IN-SITU OBSERVATION OF LÜDERS TYPE STRAIN PROPAGATION OVER POLYCRYSTALLINE AGGREGATES

by

Hasan Can Kubat

B.S., Mechanical Engineering, Boğaziçi University, 2021

Submitted to the Institute for Graduate Studies in
Science and Engineering in partial fulfillment of
the requirements for the degree of
Master of Science

Graduate Program in Mechanical Engineering

Boğaziçi University

2024

ACKNOWLEDGEMENTS

First and foremost, wholeheartedly thanks to my parents for the person who I am now. They have supported me endlessly throughout my educational and academic journey. They are always concerned with my well-being and they have never let me down with any choices I made, they were always there to support me. I cannot repay them for anything they have done throughout my life but at least, I am happy to be the son they are proud of.

I would like to express my deep gratitude to my advisor, Assoc. Prof. C. Can Aydıner, for the guidance he provided throughout my academic journey. He was the one and only person who advised me to continue the academic career after my Bachelors degree. He is an exemplary academic and advisor with immense knowledge, patience and wisdom who is always there for his students. His endless and tireless support throughout my journey of Master's degree is invaluable for me. Also, I would like to express a special gratitude to my jury members Prof. Nuri Ersoy and Prof. Demirkan Çöker for their efforts and wise counsel for my thesis.

Lastly, I wish to express my endless thanks to my MECHAMAT laboratory members Necdet Ali Özdür and Olcay Türkoğlu. They were always there for me with their experiences and knowledge. It was a pleasure to work with such great colleagues. I need to mention my friend Doğancan Kuloğlu who was my longtime friend from the prepatory year. He was always at by my side at both good and bad times. I feel gratitude for his company throughout my Master's journey.

This work was partially supported by B.U. Research Fund at Boğaziçi University under contract 22AM3.

ABSTRACT

IN-SITU OBSERVATION OF LÜDERS TYPE STRAIN PROPAGATION OVER POLYCRYSTALLINE AGGREGATES

Lüders bands are characteristic localized shear bands that are commonly observed at the initial yielding of low-carbon steels. These bands develop due to dislocation slip activity. Similar bands are observed at Magnesium specimens as well but the governing deformation mechanism for them is deformation twinning. On polycrystalline aggregates, individually twinned grains form Lüders-like macroscopic shear bands that are called collaborative twin bands (CTB). Twinning-based deformation has been studied extensively due to the attractive mechanical properties of Magnesium. The formation and expansion of these deformation bands are extremely abrupt and anisotropic. This study aims to experimentally observe the abrupt CTB activities on polycrystalline Magnesium with analyzing the effects of crystallographic texture and strain-rate on temporal resolution channel. Hot-extruded and hot-rolled specimens are compressed with low (0.001 s^{-1}) and high (0.01 s^{-1}) strain-rates. Specimens are imaged in-situ with 500-1000 Hz acquisition frequency. Four scalar parameters that derived from nominal velocity and strain-rate fields are created for tracking CTB activities. For the sharper rolling texture, individual CTB activities on the low strain-rate specimens have been successfully captured over displacement and strain fields computed with digital image correlation (DIC). The CTBs show a more uniform expansion at the higher strain-rate, although the initial CTB nucleation is an explosive event. As for extruded specimens, no discrete CTB advances are registered, highlighting the importance of crystallographic texture in CTB activity. Low strain-rate rolled specimens are further analyzed for the duration of CTB advances. Using two experiments with different sampling rates (532 and 998 Hz respectively), the average nominal duration of individual CTB activity is determined to be approximately 2 ms.

ÖZET

LÜDERS BENZERİ GERİNİM ATAKLARININ YÜKLEME ALTINDA POLİKRİSTAL KÜMELER ÜZERİNDE İNCELENMESİ

Lüders bantları genellikle düşük-karbon çeliklerinin ilk akma anında gözlemlenen lokalize kesme gerilimi bantlarıdır. Bu bantlar dislokasyon kayma aktivitelerinden dolayı oluşur. Benzer bant oluşumları Magnezyum numunelerinde de gözlemlenir ancak bu bantların oluşum nedeni deformasyon ikizlenmeleridir. Polikristal kümelerde ikizlenen kristaller, işbirlikçi ikizlenme bantları (İİB) adı verilen Lüders benzeri maksrokopik kesme gerilim bantları oluşturur. İkizlenme temelli deformasyon, Magnezyum'un üstün mekanik özelliklerinden ötürü kapsamlı bir şekilde araştırılmıştır. Bu bantların oluşumu ve genişlemesi aniden gerçekleşir ve eşyönsüzdür. Bu çalışma, polikristal Magnezyum üzerinde ani gelişen İİB olaylarına kristalografik tekstürün ve gerilme oranının etkisini deneysel olarak zaman çözünürlüğü üzerinde incelemeyi hedeflemektedir. Sıcak haddelenmiş ve ekstrüze edilmiş Magnezyum numunelere düşük (0.001 s^{-1}) ve yüksek (0.01 s^{-1}) gerinim hızları ile baskı yüklemesi yapıldı. Numuneler yüklenirken 500-1000 Hz frekanslar ile devamlı görüntüler alındı. Nominal hız ve gerinim hızı haritaları üzerinden İİB aktivitelerini takip etmek için dört adet skalar parametre çıkarıldı. Keskin kristalografik tekstürlü haddelenmiş ve düşük hızla yüklenen numunelerde DIC deplasman ve gerinim sonuçları başarılı bir şekilde bireysel İİB aktivitelerini yakaladı. Yüksek hızla yüklenen numunelerde ilk İİB oluşumu ani bir atak göstermesine rağmen oluşan İİBler sabit bir yayılım gösterdi. Ekstrüze edilmiş numunelerde İİB aktivitesi izlenemedi ki bu sonuç kristalografik tekstürün CTB aktivitelerine önemli etkisinin bir göstergesidir. Düşük hızla yüklenen haddelenmiş numuneler bireysel İİB aktivitelerinin sürelerini belirleyebilmek için daha detaylı incelendi. Nominal İİB aktivite süreleri, görüntü alma frekansları farklı (sırasıyla 532 ve 998 Hz olmak üzere) iki deneyde yaklaşık aynı ve 2 ms olarak hesaplandı.

TABLE OF CONTENTS

LIST OF FIGURES

LIST OF TABLES

LIST OF SYMBOLS

c, a	Hexagonal-close-packed coordinate axes
$h(x, y)$	Savitzky-Golay digital differentiator
i, j	Subset center coordinates
M	Interpolation radius
N	Number of sequential images recording individual CTB events
Q	Rotation tensor
t_{CTB}	Individual CTB event duration
T	Individual CTB event duration
u	Displacement field along x
U_x	Displacement field along x
$U(x, y)$	Displacement field with respect to x,y coordinates
$\dot{U}(x, y)$	Nominal velocity field with respect to x,y coordinates
v	Displacement field along y
x, y	Camera Cartesian coordinates
γ	Angle between stress vector and slip direction / Shear strain
Δt	Time interval between sequential images
Δu	Displacement gradient tensor
ε	Infinitesimal strain
$\dot{\varepsilon}$	Infinitesimal strain-rate
σ	Far-field stress
τ_{RSS}	Resolved shear stress
ϕ	Angle between stress vector and slip plane normal
ω	Infinitesimal rotation

LIST OF ACRONYMS/ABBREVIATIONS

BCC	Body-centered-cubic
CTB	collaborative twin band
CRSS	Critical resolved shear stress
DIC	Digital image correlation
ED	Extrusion direction
EDM	Electrical discharge machining
FCC	Face-centered-cubic
HCP	Hexagonal-close-packed
ND	Normal direction
STD	Standard deviation
RBM	Rigid-body motion
RD	Rolling direction
ROI	Region of interest
RSS	Resolved shear stress
TD	Transverse direction

1. INTRODUCTION

1.1. Motivation

Metallic alloys are widely used engineering materials for structural components. They are preferred for their high-strength and high-stiffness properties for such applications. Excluding specific applications such as creep resistant turbine blades [1], almost all metals used in various industries have a polycrystalline microstructure. The elastic deformation behavior of polycrystalline metals are mostly well behaved without any large-scale strain patterning. However, the plastic behavior of polycrystalline metals may vary distinctively and can show nonuniform and heterogeneous deformation. Low-carbon steels and some Aluminum-Magnesium alloys show heterogeneous Lüders banding deformation during initial yielding [2–4]. Band-like localized strain attacks cause plastic softening instability during Lüders banding [5], resulting in a serrated stress-strain curve [6, 7]. In addition, some polycrystalline metals shows Lüders-like localized band deformation but the underlying factor is deformation twinning rather than dislocation slip [8–10]. Magnesium and its alloys are among these materials that show localized Lüders-like plastic deformation due to profuse and coordinated twinning deformation within their polycrystalline aggregate [9].

Magnesium alloys stand out with their high specific strength (strength to density ratio) as the lowest density structural metals (1.7 g/cm^3) [11]. Therefore, the automotive and aerospace industries are especially interested in extending the employment of Magnesium for energy savings and decreasing harmful emissions [12]. Despite their attractive properties, hexagonal close-packed (HCP) Magnesium alloys exhibit pronounced intricacy in their deformation mechanisms, complicating their utilization. They are known for extreme plastic anisotropy and load path dependence in their mechanical response [13–16].

Hexagonal close-packed alloys, in general, have limited malleability due to insufficient number of independent slip systems [17]. For Magnesium, the slip systems further have significantly different activation ease [18]. Thus, Magnesium crystals cannot accommodate to all strain inputs easily with their available slip systems. As a result, deformation twinning that also provides strain along c-axis emerges as a favorable mechanism for Magnesium crystals [19]. Twinning, however, is unipolar. That crudely means that if a certain twin mechanism works under tension, it does not work under compression [9], [19,20]. The most common twin system observed in Magnesium is the tensile twin [21] that can dominate the strain accommodation along certain load paths (but not opposite to them).

Specific manufacturing methods influence the crystallographic texture (preferred orientation distribution) of polycrystalline Magnesium alloys [22]. Hot-rolled magnesium grains are imparted a sharp texture, where the c-axes of the HCP unit cells are preferentially aligned and directed vertically to the rolled plate. On the other hand, hot-extruded Magnesium grains have a less sharp texture, where the c-axis of the grains are distributed randomly along the radial directions of the extruded rod. Texture of Magnesium alloys heavily influences the spatial and mechanistic aspects of plastic deformation [23].

A further issue with twinning-dominant deformation in a Magnesium polycrystal is strain patterning. Simply put, twin activation (an abrupt event) inside a grain within the polycrystalline medium favors twinning in its neighbors. For this effect will be repeated in the neighbors, coordinated twinning proliferation abruptly propagates across the crystal as an autocatalytic process [10]. Consequently, these form Lüders-like macroscopic strain localization bands (shear bands), that are called collaborative twin bands (CTBs) [9] previously. Even under position-controlled loading, the abrupt strain output of the CTB advances can be higher than the imposed strain, resulting in load drops and, hence, serrated stress-strain curves [10]. Such behavior is observed at the classical Lüders yielding plateau for low-carbon steels as well. Both deformation regimes involve momentary strain softening.

There are several factors that affect the dynamic behavior and strain content of CTB formations. Crystallographic texture is highly associated with the band characteristics. Sharper texture leads to more localized (compact) CTBs to develop. In contrast, compactness of twin bands decreases with less sharp texture, leading to more diffused strain distribution of CTBs [23]. Residual plasticity is another factor that interfaces with the distribution of twin bands and hardening behavior of the material. These residual plasticity regions may be caused by either another intersecting CTB or residual slip caused by previous loading history of the material. Twin bands show a less compact distribution of strain when intersecting with such previously deformed (hardened) regions [16]. Strain-rate is another factor that promotes the twin activity against competing micro-mechanisms [24, 25].

Twinning deformation of Magnesium alloys has been studied in many aspects. Texture dependent behavior, cyclic loading response, residual intensity parameter of Magnesium twinning has been researched in MECHAMAT Laboratory [9], [23], [16], [26–28]. Most of these studies focused on the spatial resolution (analysis of whole material field in detail) of the specimens, sacrificing the temporal resolution (analysis of the material field with high frequency sampling). Although it is known that CTB activities are abrupt events even under quasistatic loading [29, 30], there are hardly any studies that focus on the temporal evolution of the CTB bands that form and advance under small applied strain-rates. This study aims to fill the research gap on CTB behavior of polycrystalline Magnesium under small strain-rate loading, with its dependencies on texture (rolled and extruded samples) and applied strain-rate.

1.2. Scope and Objectives

In this study, deformation behavior with a particular focus on deformation twinning of polycrystalline Magnesium alloys are investigated with in-situ and high sampling digital image correlation (DIC). Specimens are extracted from hot-rolled plate and hot-extruded rod of Magnesium AZ31 to investigate the texture dependent behavior of the twin deformation. The specimens are loaded along their rolling (RD) and

extruded (ED) directions for hot-rolled and hot-extruded specimens respectively to activate tensile twin systems. All specimens are extracted from rolled plate or extruded rod with their approximately identical pairs to conduct compression experiments with both low and high strain-rates of 10^{-3} s^{-1} and 10^{-2} s^{-1} respectively.

The main purpose of the study is to investigate the deformation events on the specimens with temporal resolution. Continuous full-field images are collected for this purpose. Therefore, material field scan in microscopic scale (spatial resolution) is sacrificed for high frequency image acquisition on macroscopic scale. Varying acquisition frequencies from 532 Hz to 998 Hz are implemented depending inversely on the size of the region of interest (ROI). The development and evolution of the CTBs are investigated with DIC. Various statistical methodologies are employed to detect the CTB expansion attacks. The compactness of these band attacks and their expansion speed are investigated afterwards.

Selection of specimen geometries differ from each other. It is known from previous studies that extruded specimens show no significant heterogeneous (localized) twinning deformation [23]. Thus, parallel notches on both sides of the extruded specimens are carved via electrical discharge machining (EDM) to direct homogeneous twin formation [28]. Hot-rolled specimens are larger than hot-extruded specimens, and had to be investigated with a lower acquisition frequency (532 Hz). To increase the acquisition frequency, a new set of specimens are extracted from the rolled plate with notches on both sides that forms approximately 45° with each other. The camera is rotated with this angle to investigate the region between the notches with higher frequency (998 Hz).

The most challenging obstacle for experiments with high-frequency image acquisition is DIC error. Since the time interval between consecutive images ranges between 1 ms and 1.88 ms, the deformation signal is considerably low and is affected significantly by the DIC error. Therefore, several improvenets are implemented to reduce the error. Lowering the subset size is essential for reducing the averaging error of localized strain

data. For this purpose, DIC pattern is improved via utilizing fine particle spraying tools. A speckle pattern with finely distributed small particles improves the subset uniqueness and reduces the pattern-induced bias error. Another error source is the vibration of the setup, resulting in undesirable rigid-body motion (RBM) between the images. Vibration isolators are used to eliminate such effects as much as possible.

In summary, the aim of the study is to provide results that account for the temporal resolution of twinning deformation on polycrystalline Magnesium specimens with texture and strain-rate comparison. Previous studies on the temporal aspect of polycrystalline Magnesium deformation have utilized Kolsky bars with high acquisition frequencies (orders of 10^6 Hz) [31], [24]. However, such high acquisition frequencies require significantly high strain-rates (orders of 10^3 s^{-1}), making the experiment an impact test. Abrupt activities of CTBs are not specific only to significantly high strain-rates. Even within the quasistatic range of loading, CTB events occur suddenly. One of the indicators of abrupt activity is the characteristic crackling noise that Magnesium alloys emit when twinning under quasistatic loading [29,30]. This study targets the temporal behavior at quasistatic strain-rates. The results are expected to increase the understanding of Magnesium twinning deformation behavior and aid in the development of novel crystal plasticity models [32–34].

2. BACKGROUND

2.1. Slip Systems of Magnesium Alloys

Dislocations within atomic lattice can glide along specific planes and directions. Gross-scale of these actions are called dislocation slip deformation and it is the main plastic deformation mechanism for most metals. Slip planes and directions are unique to the unit cell structure where, in general, the most close-packed atomic planes and directions are the slip planes and directions of the unit cell of a material [17]. When a crystal is subjected to deformation, available slip systems that can accommodate the deformation (if deformation field has component along the Burger's vector of the slip system) activate and accommodate to the deformation. Whether a slip system activates or not depends on a threshold value of the projected shear stress along the slip direction of the slip plane [21], [35]. The projected stress on the slip plane along slip direction is called resolved shear stress (RSS) and the threshold value of RSS that can activate that specific slip system is called critical resolved shear stress (CRSS). RSS and CRSS of a slip system is governed by Schmid's Law that can be expressed as

$$\tau_{RSS} = \sigma \cos\gamma \cos\phi, \tag{2.1}$$

where σ is far-field stress, γ is angle between stress vector and slip direction, ϕ is angle between stress vector and slip plane normal.

Number of available slip planes is proportional with the symmetry of the crystal. There are 12 unique slip systems for materials with face-centered-cubic (FCC) lattice and 24 unique slip systems for materials with body-centered-cubic (BCC) structure [17]. However for HCP lattice, this number goes down to the 4 unique slip systems due to low symmetry of HCP lattice [21]. In case of Magnesium crystals which has HCP crystal structure, these slip systems are insufficient to accommodate strain from all directions easily. In Figure 2.1, HCP crystal structure and available slip systems of

Magnesium are shown. HCP atomic structure and hexagonal coordinate system (a_1, a_2, a_3, c axes) of Magnesium unit cell is illustrated in Figure 2.1a. Figure 2.1b shows the basal slip system of $\{0001\}$ plane in direction of $\langle 11\bar{2}0\rangle$ with Burger's vector of $\langle a\rangle$. Prismatic slip system on $\{10\bar{1}0\}$ plane in direction of $\langle 11\bar{2}0\rangle$ with Burger's vector of $\langle a\rangle$ is shown in Figure 2.1c. First and second order pyramidal slip systems are presented in Figures 2.1d and 2.1e respectively. First-order pyramidal slip occurs on plane $\{10\bar{1}1\}$ along $\langle 11\bar{2}0\rangle$ direction with Burger's vector of $\langle a\rangle$. Second-order pyramidal slip occurs on plane $\{11\bar{2}2\}$ along $\langle \bar{1}\bar{1}23\rangle$ direction with Burger's vector of $\langle a+c\rangle$.

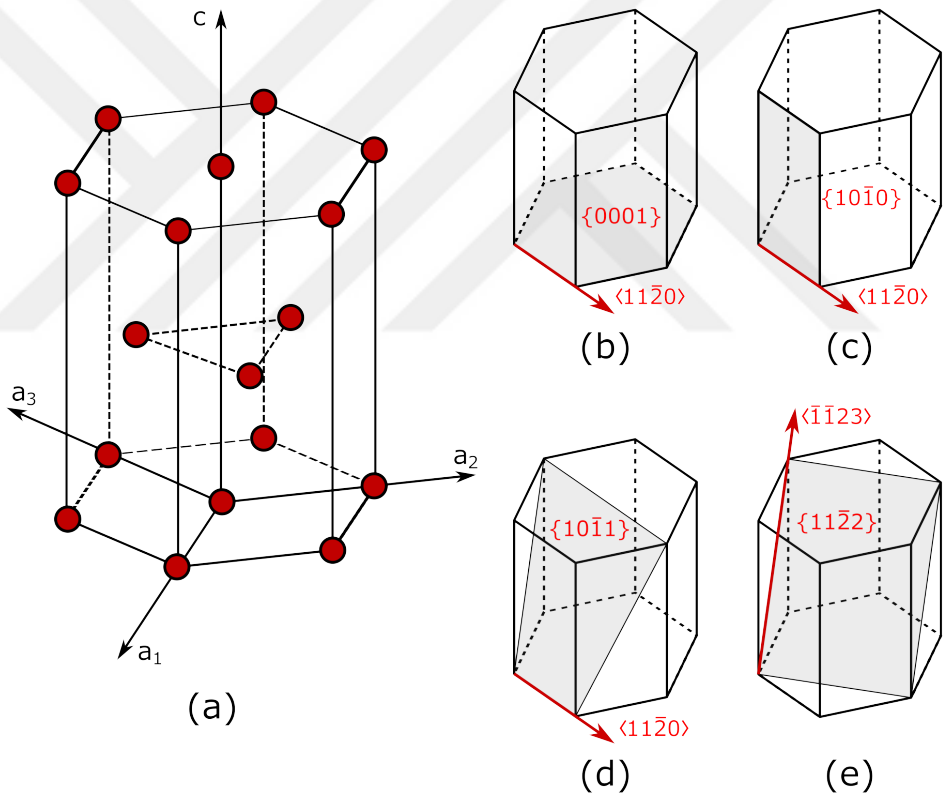

Figure 2.1. Slip Systems of HCP unit cell of Magnesium alloys. (a) HCP unit cell with its hexagonal coordinate system, (b) basal slip system, (c) prismatic slip system, (d) first-order pyramidal slip system, (e) second-order pyramidal slip system.

Presented slip systems have vastly different CRSS values from each other. The basal slip system is the easiest slip system among all available slip systems with lowest CRSS required to activate [34], [36]. Both first and second-order pyramidal slip systems

are the hardest to activate with highest CRSS value among all available systems [18], [37]. Magnesium HCP lattice can easily accommodate strain on its basal plane, because Burger's vector $\langle a \rangle$ is associated with three unique slip systems. However, only second-order pyramidal slip system can give strain output along c-axis with its Burger's vector of $\langle a + c \rangle$. Although there is available slip system that can give output displacement along c-axis, associated slip system requires significantly high RSS to activate [18], [36]. Therefore, deformation twinning becomes a favorable alternative deformation mechanism in HCPs and most commonly observed in Magnesium crystals [19].

2.2. Deformation Twinning of Magnesium Alloys

Twinning is a reorientation process of the atoms within the lattice along a specific twin planes. Atoms reorient themselves by taking their mirror image with respect to the twin plane. As result of twinning, lattice orientation significantly changes across the twin plane. This type of deformation can be observed from all type of unit crystals, but mostly from low-symmetry HCP crystals [21]. As explained in Section 2.1, deformation twinning is a favorable mechanism for Magnesium due to insufficient number of easily activated independent slip systems to accommodate strain along all directions [19].

There are several differences between dislocation slip and deformation twinning [19], [21], [38]. During deformation twinning, displacement field of individual atoms varies significantly because reorientation path of atoms differ from each other depending on their individual position with respect to the twin plane (e.g., in Figure 2.3d, displacement field of the atoms within twin region is not a uniform field). Unlike dislocation slip where displacement field of atoms are uniform along the slip plane, nonuniform displacements of atoms results in heterogeneous shearing within twin region. Another difference is time-dependence of the deformation mechanisms. Lattice reorient itself abruptly during twinning, but deformation occurs gradually for dislocation slip. Lastly, twinning is a load direction dependent (unipolar) mechanism. Twinned region within the atomic lattice can only either elongate or contract the lattice (e.g., Figure 2.3 twins can only elongate the material, and thus, can be activated under only tensile strain

along c-axis.) along the load direction. If applied strain direction coincides with the twin strain direction (tensile strain for the twins that elongates the lattice along c-axis or compressive strain for the twins that contracts the lattice along c-axis), the twin system can activate.

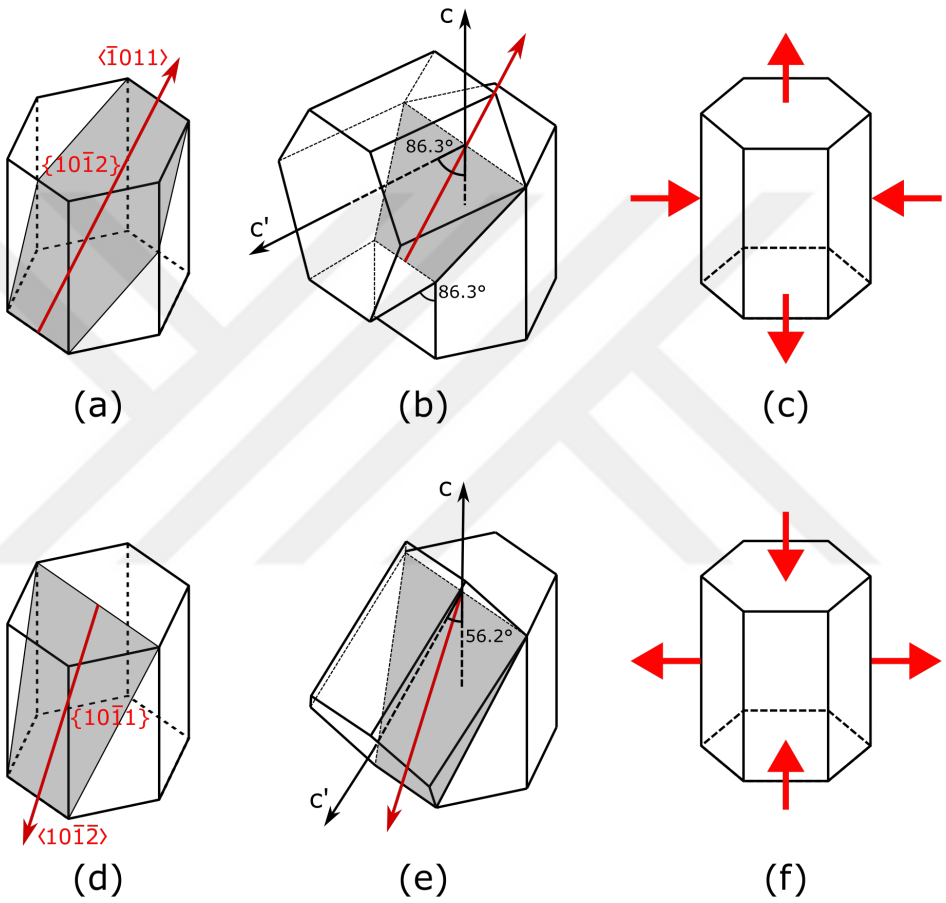

Figure 2.2. Twin systems of Magnesium HCP crystal. (a) tensile twin plane and direction, (b) (tensile) twinned unit cell, (c) favorable loading directions to activate tensile twin, (d) compressive twin plane and direction, (e) (compressive) twinned unit cell, (f) favorable loading directions to activate compressive twin.

Magnesium has two twin systems as illustrated in Figure 2.2. $\{10\bar{1}2\}\langle\bar{1}011\rangle$ extension (tensile) twin system is shown in Figure 2.2a, $\{10\bar{1}1\}\langle10\bar{1}\bar{2}\rangle$ contraction (compressive) twin system is shown in Figure 2.2d. Twinned unit crystals and their new orientations for tensile and compressive twinning are shown in Figures 2.2b and 2.2e

respectively. Since twinning is unipolar, favorable loading directions for tensile twinning are shown in Figure 2.2c, favorable loading directions for compressive twinning are shown in Figure 2.2f. The most commonly observed twinning mode for Magnesium is $\{10\bar{1}2\}\langle\bar{1}011\rangle$ tensile twin [21]. $\{10\bar{1}1\}\langle10\bar{1}\bar{2}\rangle$ compression twin mode is uncommon due to its significantly higher activation energy compared to tensile twin mode [39].

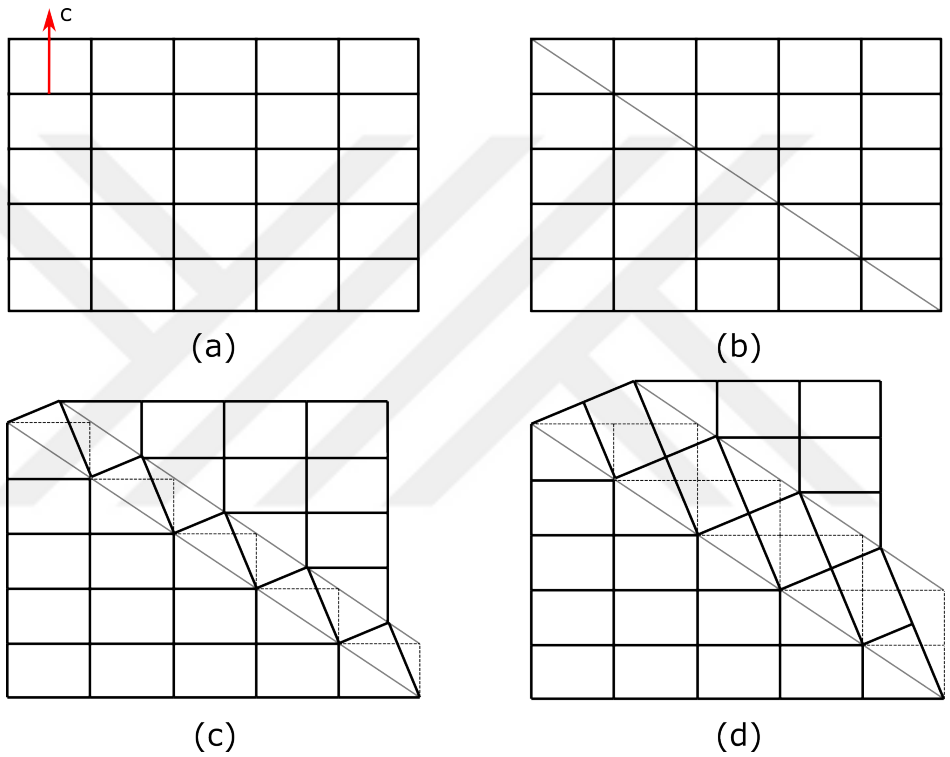

Figure 2.3. Illustration of tensile twinning in crystal structure of Magnesium. (a) initial lattice of crystal, (b) twinning plane along the lattice, (c) first line of unit crystals twinned along the tensile twin plane, (d) second line of unit crystals twinned.

Unipolarity of deformation twinning is strongly related with the unit cell geometry. For HCP unit cells, c/a ratio is the deciding parameter [21]. If c/a ratio is 1.732, the mirror image of the crystal lattice with respect to $\{10\bar{1}2\}$ twin plane is identical to the undeformed lattice. Since such reorientation accommodate to no strain, such a HCP crystal can not exercise twin deformation. For unit crystals with c/a ratio are greater than 1.732, compressive twin mode is dominant. Conversely, unit crystals with c/a ratio is lower than 1.732, tensile twin mode is dominant. In case of Magnesium,

c/a ratio is 1.624, only tensile twins can activate (Figure 2.2a-c). Lattice scale tensile twinning deformation is shown in Figure 2.3. In this Figure, lattice-scale twinning visibly results in extension along c-axis. Therefore, tensile loading along c-axis can initiate the twins. Compressive loading applied vertically along the c-axis can create tensile strain along c-axis due to the Poisson effect. Therefore, compressive loading along c-axis is a favorable loading to activate tensile twins as well.

2.3. Deformation Behavior of Polycrystalline Magnesium

Unlike conventional FCC and BCC materials such as Aluminum or steel, Magnesium crystals show rather unique deformation behavior. As explained in Sections 2.1 and 2.2, Magnesium crystals can accommodate to the strains with both its available slip and twin systems. The priority of slip or twin activation depends on the orientation between imposed strain and c-axis of the crystal unit cell. When a grain experiences twin activity, this deformation occurs abruptly and immediate change of stress and strain field occur within neighboring grain network. Resulting jump in stress and strain fields cause autocatalytic activity of twinning within the crystal network [10]. Such activity takes place within a small localized band-like region within the material field, associated with the texture sharpness [9], [23], [28]. As a result, the material develops Lüders-like strain bands which are called collaborative twin bands (CTB).

Magnesium crystals are imparted very sharp textures depending on the manufacturing method [22]. Hot-rolled Magnesium crystals face their c-axis along the plane normal of the rolled plate (Figure 3.1). Likewise, hot-extruded Magnesium crystals distribute their c-axis radially along the cross-section, vertical to the extrusion direction (Figure 3.2). When hot-rolled Magnesium is compressed vertically along the plate normal (along c-axis), only second order pyramidal slip and tensile twin system can accommodate the strain input [21]. Since CRSS of the second order pyramidal slip is much higher than the CRSS of tensile twin system [18], [39], plasticity starts with twinning. In Figure 2.4, a typical compressive stress-strain relationship of hot-rolled Magnesium is presented [13]. Compression direction is favorable for activating the ten-

sile twins. After elastic region, the tensile twin activity takes place as severely localized CTB formations. Due to being an atomic reorientation process rather than dislocation glide, twinning results in significantly less hardening than dislocation slip [40]. As a side note, deformation displays reversible behavior during cyclic loading, where twined grains within the CTB restores themselves and is called detwinning [13], [41]. During detwinning, most of the deformation is restored unless the CTB twin network interacts with other CTB network or residual slip bands [16].

Intergranular twin activity is limited and exhausted eventually with increased percentage of deformation that material experiences [13]. In Figure 2.4, twin activity ends at 3.5% - 4% strain [13]. After twin plateau region, dislocation slip becomes the dominant deformation mode. At slip dominated region, significantly increased hardening behavior occurs due to dislocation glide, generation and pile-up. Unlike twinning where most of the deformation can be restored back (detwinning), slip deformation is not reversible and leaves residual strain regions when the material is restored to its undeformed 0% strain [15, 16].

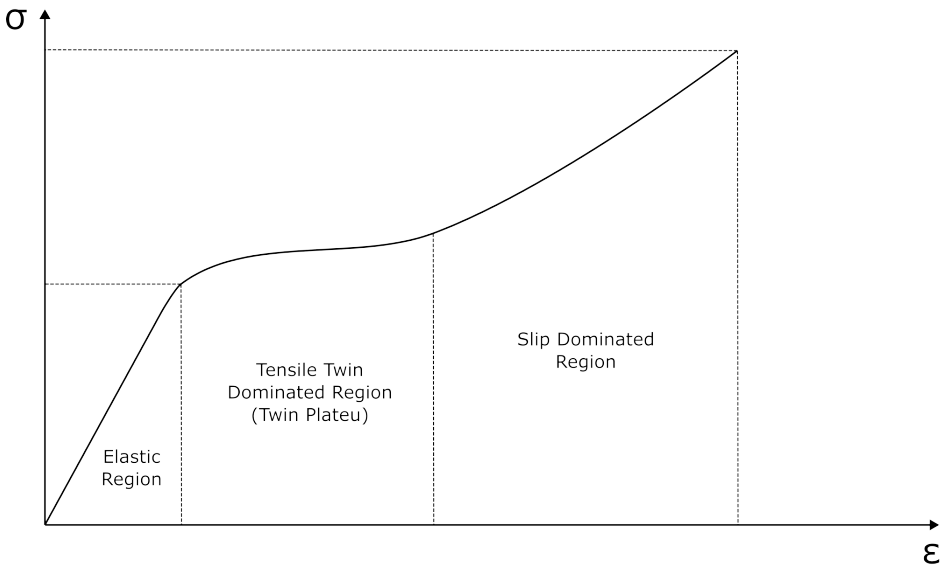

Figure 2.4. Representative stress-strain curve of hot-rolled Magnesium. Compression direction is normal to the rolled plate normal.

Hot-extruded Magnesium has smoother texture than its hot-rolled counterpart due to the radial distribution of the c-axes along extrusion direction. Compressive loading along the extrusion direction activates the tensile twins within the grains. Due to the texture difference, extruded Magnesium does not display significantly compact CTB bands [23], [28]. Strain response still indicate a band formation but the density of the twinned region is much smaller than the rolled counterpart, resulting in less average band strain. For the rolled Magnesium case, CTB bands forms 45° angle with the compression direction (along rolling direction) which indicates the plane of deformation with the highest RSS according to the Equation 2.1.

2.4. Simple Shear Deformation of CTB

For rolled samples loaded along the rolling direction, the macroscopic CTB deformation shows a simple shear type strain, elaborated in Figure 2.5. Pure shear strain and rotation as deformation gradient components is denoted as

$$\varepsilon_{xy} = \frac{1}{2}\left[\frac{\delta u}{\delta y} + \frac{\delta v}{\delta x}\right], \tag{2.2}$$

$$\omega_{xy} = \frac{1}{2}\left[\frac{\delta v}{\delta x} - \frac{\delta u}{\delta y}\right], \tag{2.3}$$

where ε_{xy} is shear strain field, ω_{xy} is rotation field, u and v are displacement fields along x and y respectively. In tensor notation, shear and rotation tensors for simple shear case are

$$\bar{\bar{\varepsilon}} = \begin{bmatrix} 0 & \frac{\gamma}{2} \\ \frac{\gamma}{2} & 0 \end{bmatrix}, \tag{2.4}$$

$$\bar{\bar{\omega}} = \begin{bmatrix} 0 & \frac{\gamma}{2} \\ \frac{-\gamma}{2} & 0 \end{bmatrix}. \tag{2.5}$$

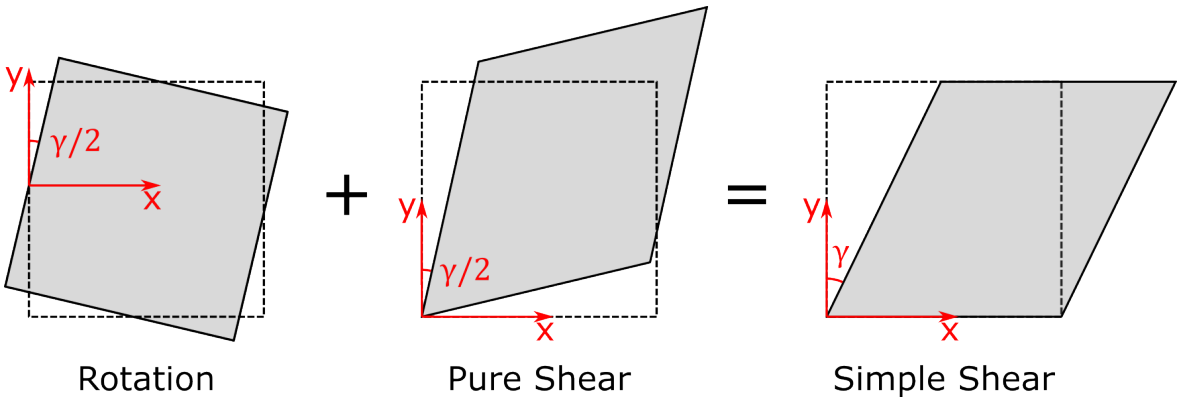

Figure 2.5. Simple shear deformation.

Simple shear is superposition of pure shear with collaboration of equal rotation. Therefore, deformation gradient tensor for simple shear case becomes as

$$\bar{\bar{\Delta}}u = \begin{bmatrix} \frac{\delta u}{\delta x} & \frac{\delta u}{\delta y} \\ \frac{\delta v}{\delta x} & \frac{\delta v}{\delta y} \end{bmatrix}, \tag{2.6}$$

$$\bar{\bar{\Delta}}u = \bar{\bar{\varepsilon}} + \bar{\bar{\omega}} = \begin{bmatrix} 0 & \gamma \\ 0 & 0 \end{bmatrix}. \tag{2.7}$$

CTBs form along the highest RSS $\pm 45°$ planes as shown in Figure 2.6. Deformation type within these bands is simple shear. However, coordinate axis is of simple shear is rotated $\pm 45°$ with respect to the as well. Therefore, strain tensors are needed to be rotated from $x'y'$ frame to xy frame as

$$\bar{\bar{Q}} = \begin{bmatrix} \cos \pm 45 & \sin \pm 45 \\ -\sin \pm 45 & \cos \pm 45 \end{bmatrix}, \tag{2.8}$$

$$\bar{\bar{\varepsilon}} = \bar{\bar{Q}}\, \bar{\bar{\varepsilon}}\, \bar{\bar{Q}}^T, \tag{2.9}$$

$$\bar{\bar{\omega}} = \bar{\bar{Q}}\, \bar{\bar{\omega}}\, \bar{\bar{Q}}^T, \tag{2.10}$$

where Q is the rotation tensor. For the case of Figure 2.6a, strain and rotation tensor becomes as

$$\bar{\bar{\varepsilon}} = \begin{bmatrix} \varepsilon_{xx} & \varepsilon_{xy} \\ \varepsilon_{xy} & \varepsilon_{yy} \end{bmatrix} = \begin{bmatrix} \frac{\gamma}{2} & 0 \\ 0 & \frac{-\gamma}{2} \end{bmatrix}, \tag{2.11}$$

$$\bar{\omega} = \begin{bmatrix} 0 & \frac{\gamma}{2} \\ -\frac{\gamma}{2} & 0 \end{bmatrix}. \tag{2.12}$$

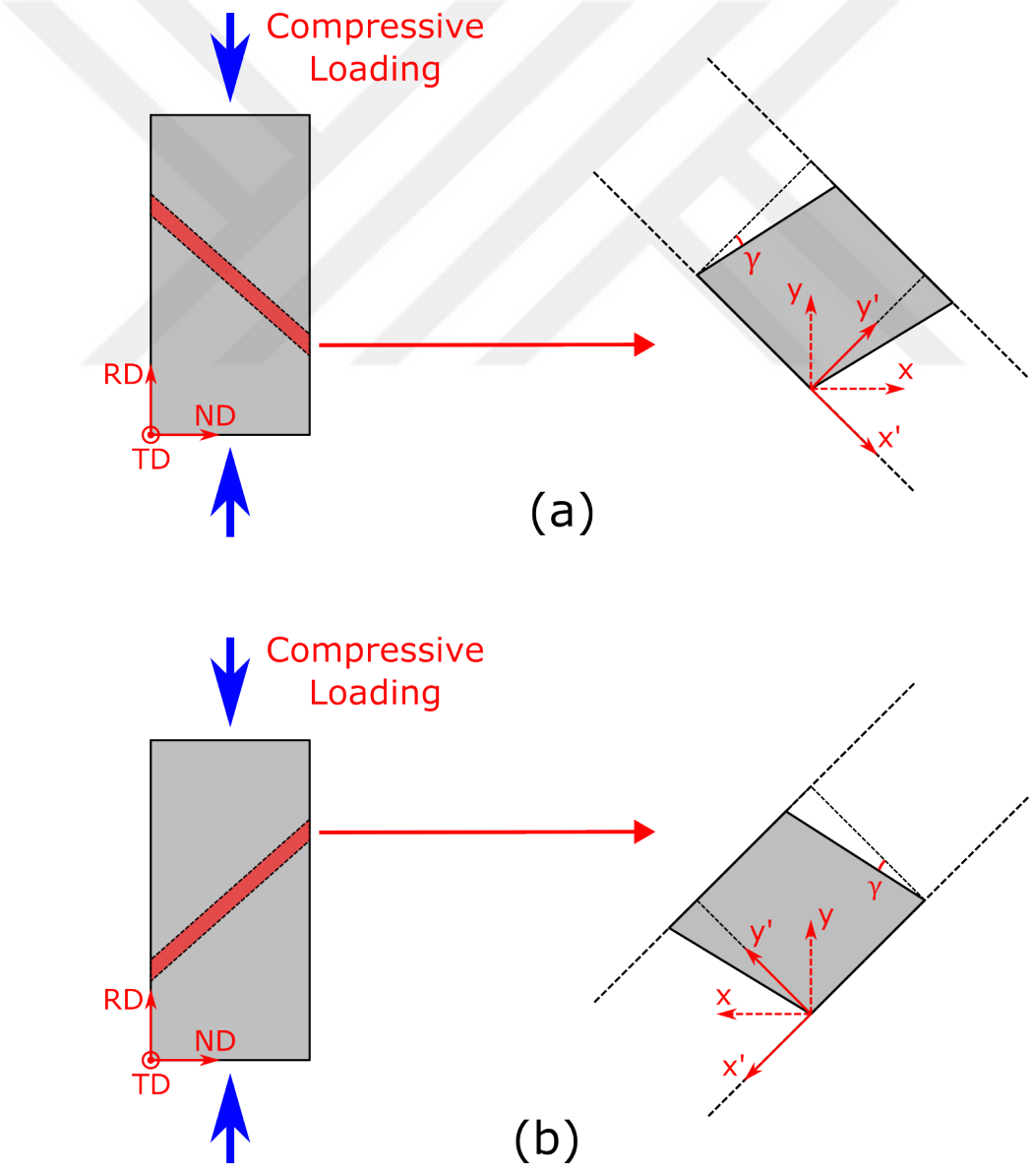

Figure 2.6. Simple shear deformation of ±45° CTB. (a) -45° CTB, (b) 45° CTB.

Equation 2.11 indicates that the ±45° CTB shear strain is transformed into bi-axial strain with Poisson's ratio of 1 on the specimen xy coordinate frame. In-plane rotation (ω) is unaffected.

2.5. Twin Band Behavior and Dynamics

The MECHAMAT Laboratory at Boğaziçi University has conducted systematic experimental studies on the twinning behavior of Magnesium alloys considering the effects of crystallographic texture and load path [9], [16], [23], [28]. Telemez et al. [9] first conducted in-situ microscopic image correlation measurements on rolled Magnesium AZ31B alloy as a sample is compressed in the rolling direction. It has shown that the deformation pattern of Magnesium specimen shows the collaborative activity of the tensile twin bands forming sharp macroscopic bands that span the sample. Strain distributions are extremely heterogeneous due to the abrupt twinning activity (Figure 2.6. Twinning behavior of the extruded and rolled Magnesium AZ31B specimens are compared by Kapan et al. [23] in cyclic loading. While the tensile twins show dominant activity under compression in each, the geometry of strain accommodation is vastly different. Highly localized and more intense/compact twinning regions emerge in the rolled specimen whereas extruded specimen shows a much more homogeneous and widespread strain accommodation. For rolled Magnesium AZ31B specimens, twinning behavior during cyclic loading (compression-tension-compression) along rolling direction is studied in micro-scale detail by Shafaghi et al. [16] For the first compression, formed CTBs are compact with average band strain of 2.2%. During tensile loading, compressive strains are mostly recovered via detwinning. Further tensile loaded specimen developed non-45° slip-shear bands, and these bands stayed residual during the second compression stage. The compactness of the new CTB formations is reduced due to remnants of the tensile plasticity. This has been quantified as a reduction from 2.2 percent average band strain of the first wave bands to around 1.4 percent. This study clearly shows that the coordinated twin activity is heavily influenced by the strain hardening fields of a deformed material.

Across Magnesium grains, the twin propagation is estimated to be a very fast process. Recording the propagation of the twin bands in a Magnesium crystal is a challenging task and demands considerably high-sampling frequency (e.g., for imaging, high-speed cameras are required). High-speed imaging studies in the literature for twinning, however, are rare and typically for extreme cases where the entire sample is loaded with very high strain-rates (e.g., with Kolsky bars). The recent study of Kannan et al. [31] on twin dynamics is conducted on a single crystal. Compressive loading is applied normal to the c-axis of the crystal. Using a camera that has an acquisition frequency on the order of 10^6 Hz, they loaded the specimen with high strain-rates ($\dot{\varepsilon}$ = 2000-3000 s^{-1}). The twins propagate with extreme speeds; the first nucleated twin tip travels approximately 5 mm of path in 6 μs. Peak $\{10\bar{1}2\}$ twin tip velocities are in the range of 1000-2000 m/s which is comparable to the speed of sound on Magnesium around 4000 m/s.

For polycrystalline specimens, the twin band formation occurs over numerous grains by autocatalytic twinning, namely, twin nucleated in a grain causes new twin formations in the neighboring grains [10]. As a result, twin bands propagate from one end of the sample to the other in a collaborative fashion. Kannan et al. [24] presented a study for twin dynamics on polycrystalline extruded Magnesium AZ31B specimens. The application of experiment is high speed acquisition (frequency in order of 10^6) with high strain-rate compressive loading along extrusion and transverse directions ($\dot{\varepsilon}$ = 5000 s^{-1} for extrusion direction, $\dot{\varepsilon}$ = 7500 s^{-1} for transverse direction). His results showed that on macroscale level, CTB propagation occurs in the orders of 1 μs under extremely high strain-rates. These results from high strain-rate applications indicate that twin propagation speed is high for both single crystal and polycrystal specimens. Additionally, Ulacia et al. [25] reported that twin activity is significantly increased for sheet Magnesium AZ31B under high strain-rate applications. Abrupt activity of CTB is not only specific for extremely high strain-rate applications. CTB propagation and expansion are abrupt events at loading conditions with quasistatic strain-rates as well. Magnesium alloys emit characteristic crackling noise when twinning which is analogous

to the tin cry effect [29,30]. Such noise generated by the CTB activities is an indicator of abruptness of these events even at quasistatic loading conditions.

While the events in high strain loading with Kolsky bars are necessarily extremely fast, the twin band propagation is expected to be slower in for a polycrystalline aggregate under quasistatic applied loading. The band attacks during quasistatic applied loading (serrations in a stress strain curve where the event imposes its own strain-rate for a short period of time) are likely slower events, corroborated by the findings of Prasad et al. [42] and Kannan et al. [24] that shows correlation between twin boundary growth speeds and applied strain-rate. In addition, in polycrystalline Magnesium specimens, autocatalytic twins do not form with perfect alignment as in single crystal specimens and this activity requires complementary slip activity to maintain strain compatibility across crystallites [43]. Hence, collaborative twinning is presumably to be a slower event than the twin growth in single crystal since it is series of sequential twinning events that are interfaced by complementary slip that also consumes time. Furthermore, the findings of the MECHAMAT laboratory on the intensity (compactness) of the CTB likely point to differences in formation speeds where more compact bands are expected to be faster [16], [23], [28]. This presumably also points to differences in twin propagation speed in the two regimes, e.g., the hardened fields due to previous plasticity might create a slowing friction effect among serial twinning events. Similarly, texture, another fundamental parameter for the compactness of twin bands, is likely to influence their propagation speeds.

3. EXPERIMENTAL METHODS

3.1. Specimen Selection and Preparation

The main goal of the experiments is the investigation of CTB evolution with a parametric study over strain-rate and texture. Therefore, two differently textured Magnesium AZ31 products (hot-rolled plate and hot-extruded rod) are selected. Hot-rolled plate is provided from Xi'an-Yuechen Metal Products and hot-extruded rod is provided from Alfa Aesar Chemistry. As explained in Section 2.3, hot-rolled Magnesium has sharp texture where the c-axes of crystals tends to face along the normal direction (ND) of the plate as shown in Figure 3.1. To activate the tensile twin systems on the plate, loading direction must have either tensile component along ND or compressive component along rolling direction (RD) or transverse direction (TD). On the other hand, hot-extruded Magnesium has a weaker texture where c-axes of crystal are distributed radially along the cross-section as shown in Figure 3.2. Tensile twins can be activated via applying compressive load along the extrusion direction (ED).

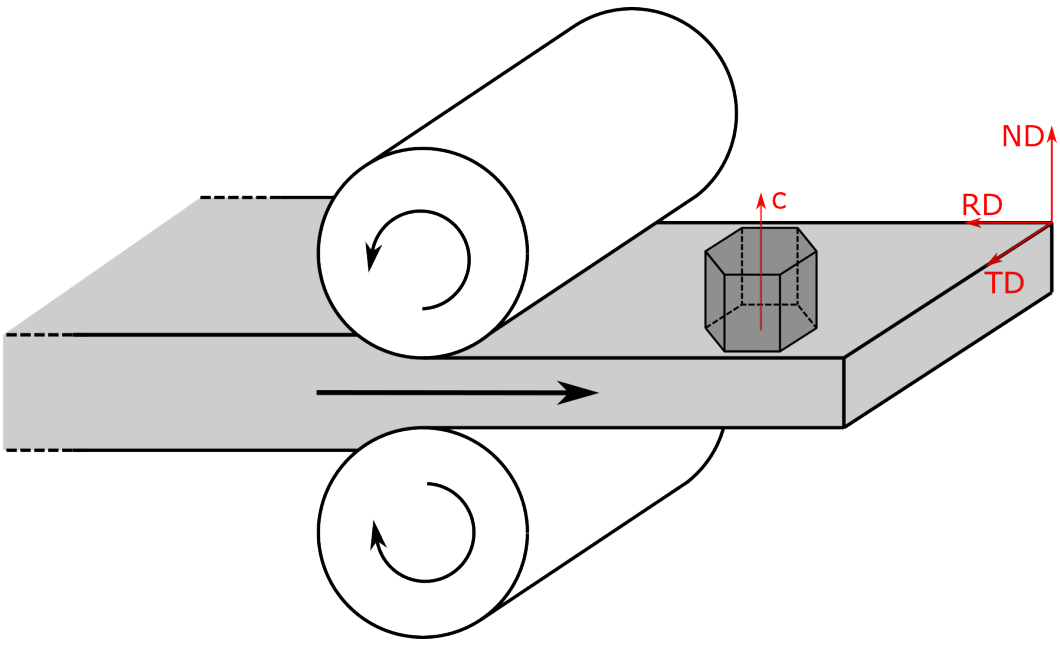

Figure 3.1. Hot-rolling process of Magnesium plate with unit crystal orientation.

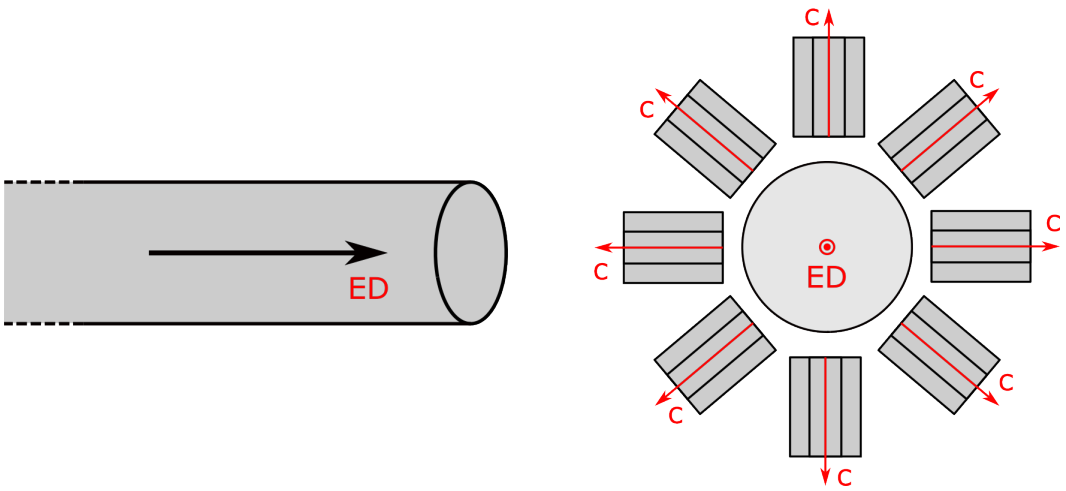

Figure 3.2. Hot-extruded magnesium plate with unit crystal orientation.

Activating the tensile twins via a tensile test is a challenging task because the specimen height is significantly constrained by the plate thickness (specimen must be put under tensile loading along c-axis, namely ND) which is 10 mm for tensile specimens. In addition, extruded rod diameter is 6.5 mm and the specimen must be extracted with its height along the diameter, also constrained. Thus, compression test is much a more viable option to use specimens with sufficient dimensions. Rolled specimens are cut along the RD, and extruded specimens are cut from the ED for that purpose via EDM. EDM is preferred because any residual plasticity alters the CTB behavior as explained in Section 2.5 and conventional methods (e.g., milling) leaves considerable residual plasticity.

A total of 6 specimens are extracted in total. 4 of them are from the rolled plate and 2 of them are from the extruded rod. The specimen shapes and dimensions are shown in Figure 3.3. Aspect ratio (ratio of specimen height to basal edge length) of 2.5 is selected to prevent buckling during the compression test for all specimens. Specimens 1 and 3 are in regular square prism shape where the DIC analysis is conducted over the full field. Specimens 2 and 4 are equivalent with 1 and 4 except for two notches are carved on both sides in 45° orientation to direct the twin bands along the corridor between the notches [28]. Only the parallelogram region between these notches are investigated with the experiments to increase the image acquisition frequency. Two

notches parallel to each other are carved on the both sides of the specimens 5 and 6. Since, extruded specimens display widespread twin band formation [23], we aim to direct those along the stress concentration regions caused by the notches [28]. As result, more localized and compact shear bands are expected. More compact bands boost the strain signal and therefore easier to track.

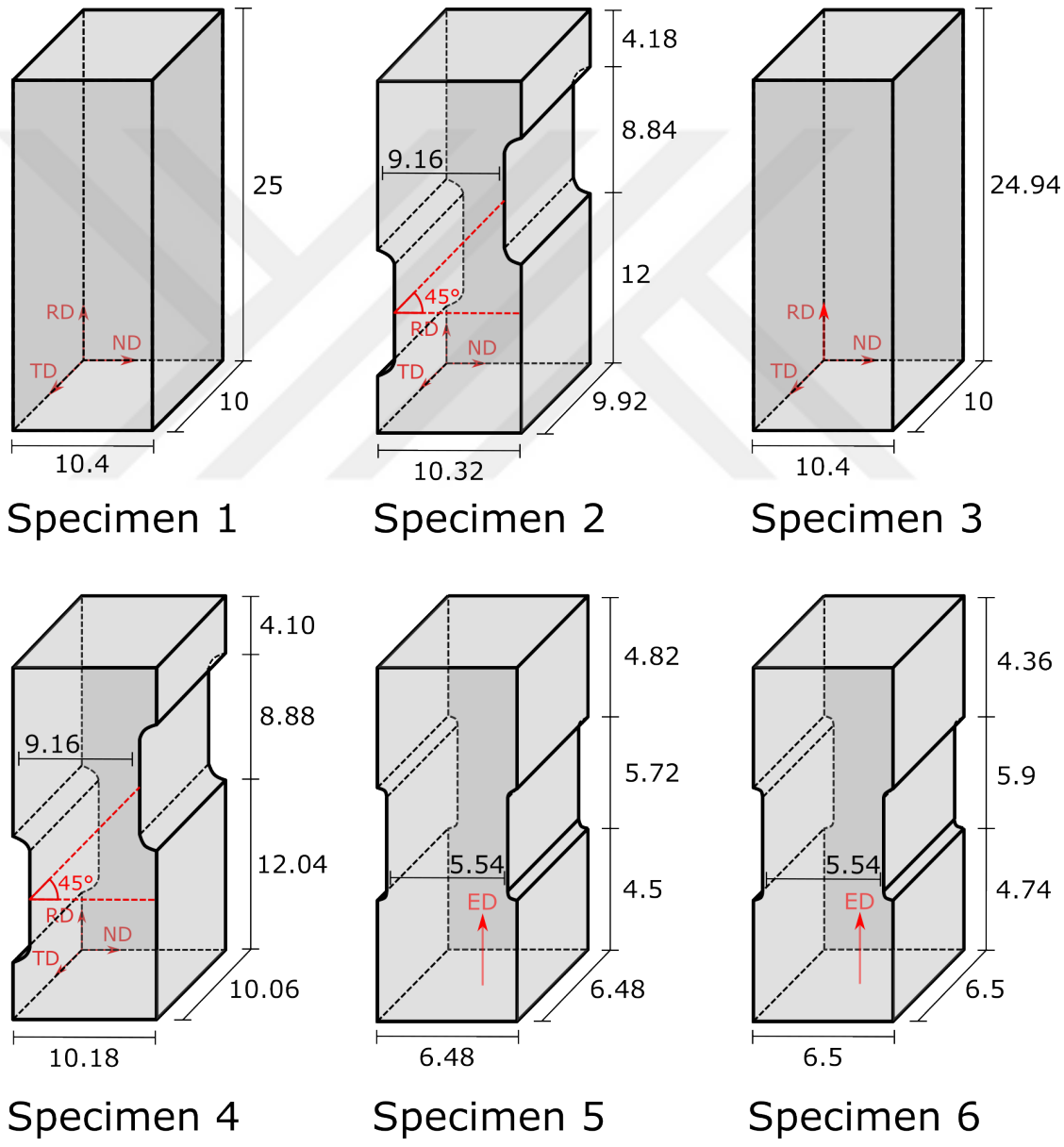

Figure 3.3. Extracted specimens and their dimensions. Specimens 1-4 are cut from the hot-rolled plate, specimens 5-6 are cut from the hot-extruded rod. All length units are millimeter.

EDM leaves a skin surface on the extracted specimens. This surface can affect the CTB behavior. In addition, rough surface reflects the light arbitrarily and unevenly. Under deformation, these light reflecting regions displace and no longer reflects light identical to their initial position. This results in a significant error source for DIC. Therefore, rough EDM skin on the experimental surfaces (TD-normal surface for rolled specimens, out of plane surface for extruded specimens in Figure 3.3) are grounded with P1200 and P2400 grinding papers. The ground surfaces are then rinsed with ethanol and acetone to remove any grease and plastic residue on them.

DIC analysis requires a random speckle pattern on the ROI. The DIC algorithm uses speckle features on the image to distinguish each subset (DIC unit element) from one another. The detail of the displacement field results of DIC is inversely proportional with subset size (larger subsets interpolate the small localized data within itself, analogous with FEM element size). However, probability of encountering an identical subset increases with decreasing spatial resolution because less features take place within these subsets. To keep the minimum subset size possible, finely distributed speckle paint (low size, densely distributed speckle) is required. Specimen surface firstly painted with thin layer of opaque white acrylic paint (the speckle patter for all specimens can be seen at Figure 3.5. Then, fine droplets of black speckle paint is sprayed on the white layer via airbrush. The quality of the speckle pattern is analyzed and quantified via an artificial RBM test (image of the speckled surface is translated artificially by subpixel interpolation, then two images are analyzed with DIC). Subset quality is quantified by calculating the standard standard deviation (STD) of the strain field of artificial RBM test with varying DIC subset sizes from 11 to 101 pixels. Normal test results are expected zero STD of strain because RBM does not induce deformation but uniform displacement field and should not develop any strain. Maximum error limit is set to 0.05% strain STD for RBM test which is obtained at 31 pixels of subset size for all experiments.

3.2. Experimental Setup

The experiments aim to in-situ recording the deformation of the specimens via continuous image acquisition. For this purpose, experimental setup shown in Figure 3.4 is established. In this setup, uniaxial loading device with load capacity of 100 kN from Zwick-Roell is used (Figure 3.4a). Specimens are placed between the compressive platens (Figure 3.4e). To prevent any deformation due to surface friction between the specimen and platens that might lead to barrelling, contact surfaces are covered with white-lithium grease. Uniaxial loading device is controlled by a computer (Figure 3.4f) which imposes the loading parameters and collects load cell data from heavy-duty compression platens.

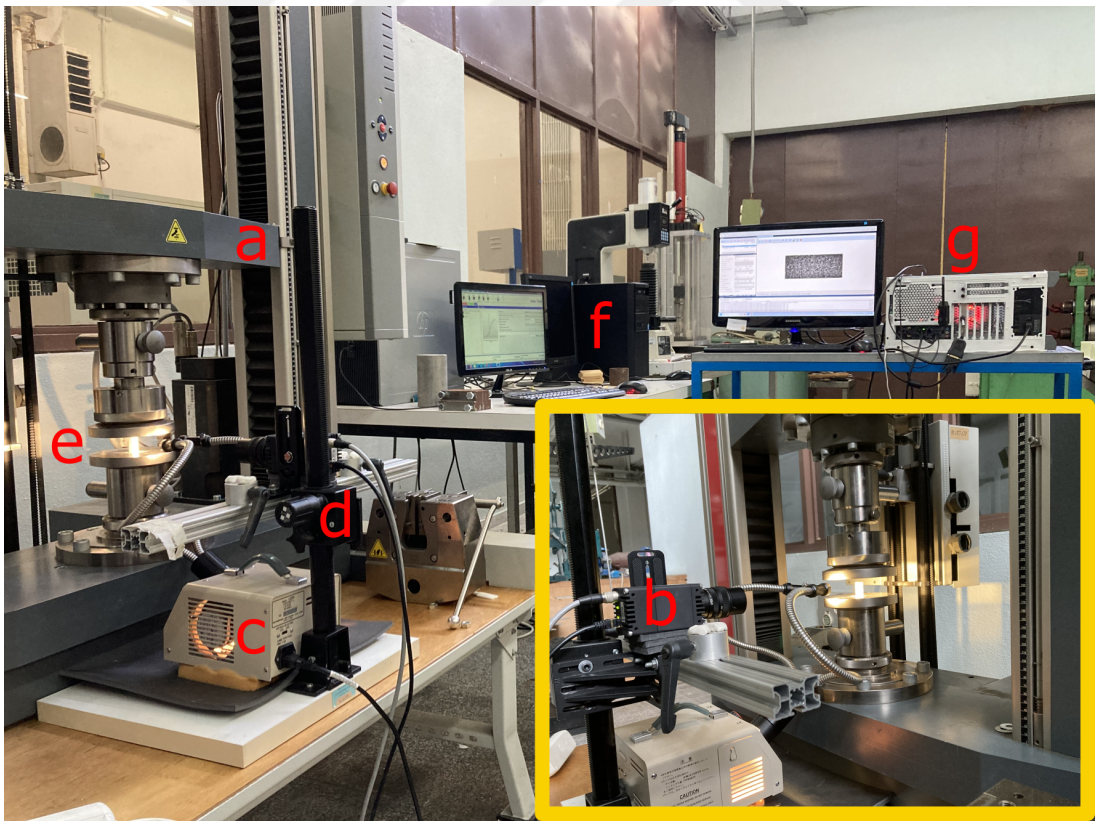

Figure 3.4. Setup used in the experiments. (a) uniaxial loading device, (b) high-speed camera, (c) halogen light source with dual fiber channels, (d) camera fixture, (e) compressive loading platens and specimen, (f) computer that controls the loading device, (g) computer that controls image acquisition.

Continuous imaging is conducted with Flir Oryx machine vision camera (Figure 3.4b). The camera can take images with 2448-2048 pixels of resolution in frequency of 162 Hz (frames per second). Image acquisition frequency of the camera sensor is an inversely proportional with frame height in pixels, ROI with lower image height than 2048 pixels results in higher acquisition frequency than 162 Hz. The maximum frames per second is obtained at 300 pixels of image height, resulting in 998 Hz frequency. The camera is mounted on a fixture that can ascend or descend the camera along z-direction (Figure 3.4d). The lightning required for imaging is provided via Olympus dual fiber channel halogen light source (Figure 3.4c). Halogen light source is selected because of the consistency of lightning compared to LED light sources that have also been tested during setup development. Duty cycle of a LED lightning requires precise synchronisation with camera acquisition due to the digital illumination output (lightning is completely zero when duty cycle is at 0 and results in completely dark images from time to time). At high frequency image acquisition, this is a challenging task because of the low exposure (shutter) time of the camera (in orders of μs). The drawback of a halogen light source is the sinusoidal function of illumination with respect to time due to AC input. Illumination differs from image to image but fluctuation is sufficiently small. The light source is isolated from the camera fixture via pads and sponges because of the vibration caused by the light source. Even though the efforts to completely isolate it, there is residual sub-pixel vibrations remaining due to either the loading device or the light source.

The camera is controlled and images are stored via a specially built computer (Figure 3.4g). The camera has no external buffer to store images. Therefore, the computer has 128 GB of RAM unit that camera uses as buffer. Taken images are sent to the computer with high bandwidth, in orders of Gbps. Thus, the computer has necessary motherboard that allows such high data bandwidth. The stored images are synchronously written to the disks. For that purpose, NVMe SSDs with high-speed writing are used.

3.3. Experimental Parameters

The experiments aim to show the effects of strain-rate and material texture on the temporal behavior of CTBs. The conducted experiments and their experimental parameters are given in Table 3.1. The loading is position controlled with imposed displacement rate. Mainly, two experiments on rolled and two experiments on extruded Magnesium specimens are conducted. Each pair of specimens are subjected to low (10^{-3} s^{-1}) and high (10^{-2} s^{-1}) strain-rates. Since rolled Magnesium specimens are larger than their extruded counterparts, full-field images of them requires larger ROI. As explained in Section 3.2, when ROI height in pixels increases, the acquisition frequency decreases. With the rolled specimen geometries (Specimens 1 and 3), acquisition frequency could be raised to maximum of 532 Hz. Thus, two other specimens with notches (Specimens 2 and 4) are used to increase the acquisition rate to absolute maximum of 998 Hz but in expense of full-field analysis. For these two notched specimens, the camera fixture is rotated by 45° degrees and only the parallelogram region between the notches are investigated (the parallelogram regions of interest are shown in Figure 3.5). Such effort to increase the acquisition frequency is not required for extruded specimens (Specimens 5 and 6) because increasing frequency from 774 Hz to 998 Hz (29% increase) is not significant to reduce the ROI further.

Table 3.1. Parameter space of the experiments. Specimens are shown in Figure 3.3.

Specimen	**Displacement Rate**	**Strain Rate**	**Acquisition Frequency**	**Analyzed Region**
Specimen 1	1.5 mm/min	10^{-3} s^{-1}	532 Hz	Full-field
Specimen 2	1.5 mm/min	10^{-3} s^{-1}	998 Hz	Notched area
Specimen 3	15 mm/min	10^{-2} s^{-1}	532 Hz	Full-field
Specimen 4	15 mm/min	10^{-2} s^{-1}	998 Hz	Notched area
Specimen 5	0.9 mm/min	10^{-3} s^{-1}	774 Hz	Full-field
Specimen 6	8.91 mm/min	10^{-2} s^{-1}	774 Hz	Full-field

The most important image acquisition parameter is the exposure (shutter) time. Exposure time is related with the illumination of the acquired images because the sensor collects less light with lower exposure time for each image. On the other hand, acquisition of the abrupt activity of CTB would result in blurry images with higher exposure time. One option is lowering the exposure time for precise images while increasing the camera gain for the decreased illumination. This option is not feasible because camera gain boosts not only illumination but noise as well. Camera noise is not desired due to the error it would introduce to DIC analysis. Therefore, the exposure time is optimised experimentally. Pixel value of a machine vision camera ranges between 0 (pure black) and 255 (pure white) grayscale interval. The parameter created for this optimization is the mean value of pixels and pixel histogram. The mean pixel value is aimed to be between 90-100 and the pixel histogram should be widely distributed. After the optimisation, exposure time of the experiments is set to value 42-56 μs depending on the density of the speckle on the material surface.

3.4. Numerical Analysis

A subset based DIC algorithm is utilized for the displacement field calculations between deformed and reference images. Main principle of the DIC is dividing the image ROI to smaller and overlapping subsets to calculate the deformation behavior of each subset. Each subset has to contain such features that the image array of the subsets are unique and distinct from each other. As explained in Section 3.1, fine particle speckling is applied for this purpose. For the experiments, each image ROI is divided into smaller square shaped subsets with edge length of 31 pixels. In Figure 3.5, speckled surface and ROI of each specimen are shown. Subsets are distributed in a way that each subset center is 10 pixels away from each other. DIC analysis with same parameters are used for all images with respect to the initially taken reference image.

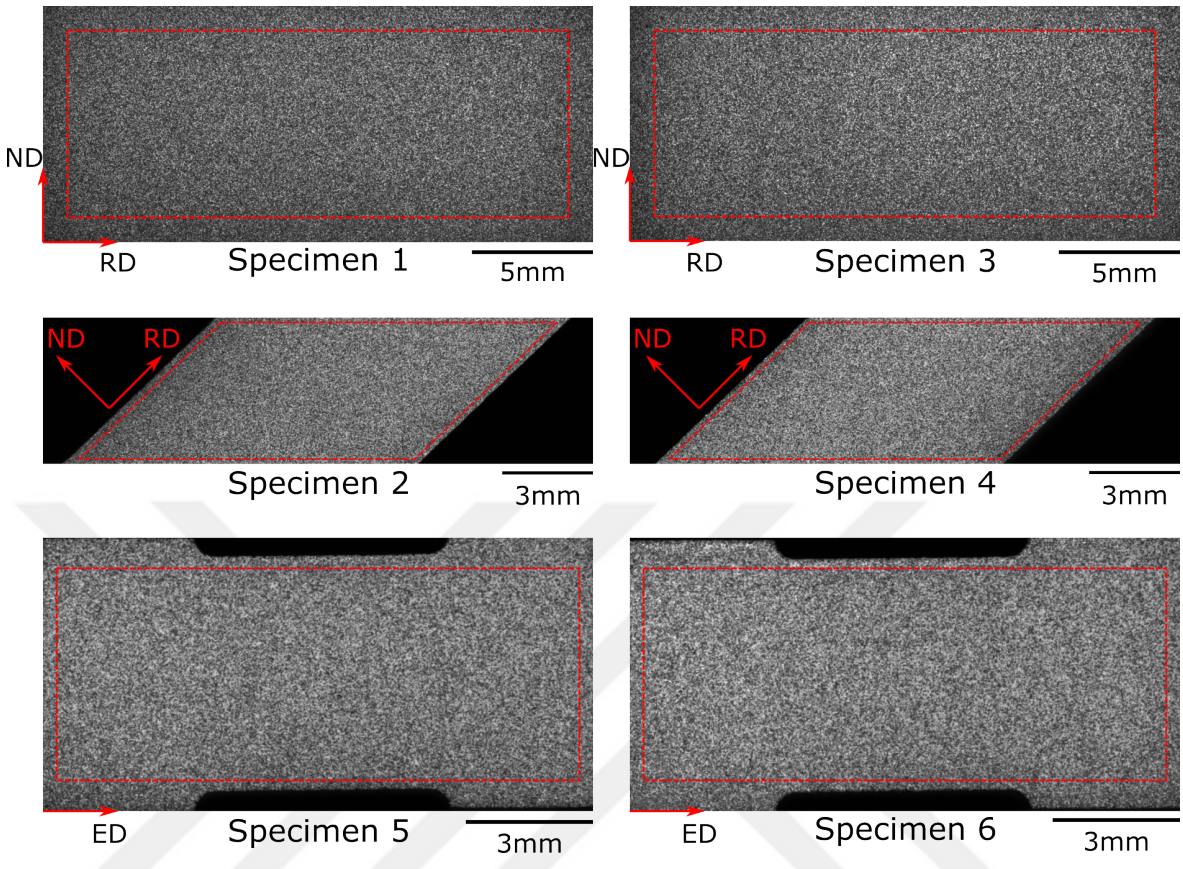

Figure 3.5. Specimen images before the experiment. DIC ROI is shown with red dashed-line boxes.

Displacement fields are calculated via a fast and robust DIC algorithm developed by Pan et al. [44]. Gauss-Newton inverse composition methodology is utilized for the algorithm. Images are analyzed with packages of 5 consecutive images with respect to the reference image. Workload is distributed equally to the processor cores to reduce the overall time required for analysis. Since, time interval between the images are small (between 1 and 2 ms), displacement field between sequential images are considerably low. Therefore, initial guess for the DIC analysis is not needed to be produced by a coarse search. Instead initial guess is taken from the displacement results of the previous set of images to reduce the computational time further. For sequential analysis (reference image of each analysis is the previous image instead of initial undeformed image), initial guess is set to 0 due to considerably small deformation.

The displacement field results of the DIC contains some errors due to halogen light illumination and sub-pixel vibration (Section 3.2), bad regions of speckle pattern and interpolation errors. Because of the errors in the DIC displacement field, displacement gradients and strains obtained for each DIC subset comes out noisy. Therefore, strains are calculated via an algorithm that utilizes convolution based Savitzky-Golay digital differentiator from the displacement fields of the subsets [45]. Strain derivation with kernel convolution is described as

$$\varepsilon_x = \sum_{x=-M}^{M} \sum_{y=-M}^{M} h(x,y)u(i+x,j+y), \tag{3.1}$$

$$\varepsilon_y = \sum_{x=-M}^{M} \sum_{y=-M}^{M} h(x,y)v(i+x,j+y), \tag{3.2}$$

$$\varepsilon_{xy} = \frac{1}{2} \sum_{x=-M}^{M} \sum_{y=-M}^{M} h(x,y)\left[u(i+x,j+y) + v(i+x,j+y)\right], \tag{3.3}$$

where i and j are center coordinates of the calculation cell, M is the calculation radius and $h(x,y)$ is the Savitzky-Golay digital differentiator. M is the value for taking account how many neighboring cells are accounted for strain calculation. Large M value averages the localized strain data resulting in excessive smoothing. Therefore, for our experiments, M value is taken 1.

The time interval between the sequential images are small (from 1 to 2 ms). Therefore, differentiation over time of strains (strain-rate) is calculated by utilizing forward and central difference methods. These methodologies are denoted respectively as

$$\dot{\varepsilon}_i = \frac{\varepsilon_{i+1} - \varepsilon_i}{\Delta t}, \tag{3.4}$$

$$\dot{\varepsilon}_i = \frac{\varepsilon_{i+1} - \varepsilon_{i-1}}{2\Delta t}, \tag{3.5}$$

where $\dot{\varepsilon}_i$ is strain-rate of point i, ε is strain field results obtained from the Equations 3.1-3 and Δt is the step size in seconds which is the time interval between the two sequential images (inverse of acquisition frequency).

4. RESULTS

4.1. Full-Field Analysis of Rolled Specimen 1 Under 0.001 strain-rate

The first experiment is conducted on Specimen 1 (Figure 3.3) with low strain-rate compression ($\dot{\varepsilon} = -0.001\ s^{-1}$). Before the loading, a pre-load of 150 N is given to make a better contact between the specimen surface and the compressive platens. The loading is position-controlled and implemented displacement rate is 1.5 mm/min. Full-sample-field analysis figures are resolved at 1400 pixels in width and 600 pixels in height. The camera could go up to 532 Hz of acquisition frequency with that resolution.

32412 images are taken with the maximum frequency (532 Hz) while the specimen is loaded during the experiment. Each image is analysed with DIC algorithm given in Section 3.4 with respect to the initially taken reference image. Load data is obtained from the load cell and mean strain data is calculated for each image with DIC and post-processing (Equations 3.1, 3.2, 3.3). Load data has lower-frequency sampling (4908 data points) than the DIC mean strain data (32412 data points). Therefore, the load data is upscaled to the size of 32412 by inserting intermediate points via equal spacing interpolation. Load values are converted to the engineering stress values by dividing the load values to the cross-sectional area of 104 mm^2. Then, stress and mean strain values are paired together to obtain the stress-strain curve that is shown in Figure 4.1.

Initial yielding starts at approximately 78 MPa, initiated with a localized CTB attack shown in Figure 4.1a. The expansion of this particular CTB (arrows in Figures 4.1a-b) is the major deformation element over the twinning plateau with a monolithic structure observed over Figures 4.1a-d. Average twin band strain is measured via taking the average of the subset strains inside a non-intersecting CTB region (a band that do not cross over another band, e.g., the band at Figure 4.1b). Characteristic twin band strain is calculated as -1.97% that is comparable to previous observations

of our laboratory [16]. Secondary CTB formations occurred at ε = -1.00% and ε = -1.50% mean strain values over Figures 4.1c-d. Visible stress-strain serrations on the plot of Figure 4.1 indicates abrupt CTB activities at points c and d. These twin band events abruptly introduce more strain than imposed, resulting in a load drop.

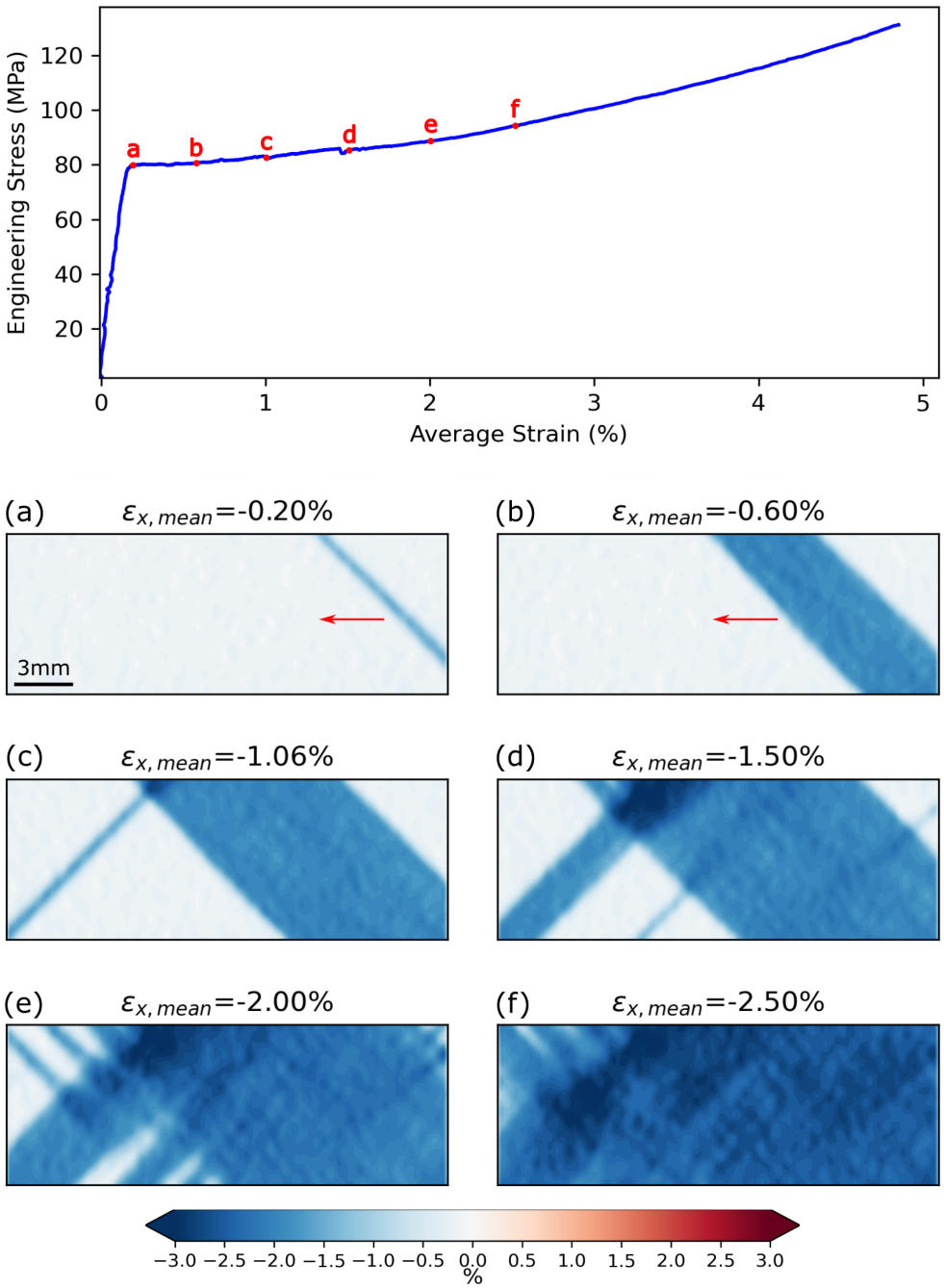

Figure 4.1. Stress-strain plot of Specimen 1. ε_x strain maps are shown on selected points of a, b, c, d, e and f on the curve to display the deformation history.

Twinning activity continues at points e and f in Figure 4.1. However, the batch of CTBs that form in this stage show a less sharp strain profile (less localized strain; more diffuse fields) which can clearly be seen in the top left corner of the strain map of point f. In addition, the material displays increased hardening over the stress-strain curve as the area fraction of CTB intersection increases. The plot (Figure 4.1) starts to deviate from the nearly perfect-plastic behavior especially after point c. After the exhaustion of the twin system (around 3% strain), much heavier hardening is observed [13] due to the switch to a much harder deformation micro-mechanism, namely, the pyramidal slip (Section 2.1).

A scalar variable (that is reduced from the spatial fields) that is solely a function of time (but not position) is desirable to identify localized CTB formation and expansion events, because of the large dataset size (32412 images over time). To derive such scalars, firstly, the displacement field results which are the first order variables obtained from DIC are investigated. During a sudden CTB advance, when one calculates the sequential displacement field (displacement field between two consecutive images separated by Δt), a dual zone imagery is obtained, apparent over Figures 4.5 and 4.6. This means the displacement field shows two clear zones, separated by the line of deformation band advance. When one takes the STD of the sequential displacement field, an elevated value is found if there is a band advance. Hence, the STD of the sequential displacement fields is regarded here as the first scalar variable (that is derived from the deformation field of each time point) in an attempt to identify CTB events over the 32412 time points.

For our case (high-frequency data acquisition), the sequential displacement field can be converted into a velocity field by taking the forward time-difference of the displacement field (Equation 3.4). This is of course a nominal velocity field that represents a mean over the sampling period of $\Delta t = 1.88\ ms$ in each time step. Here, the velocity field units are converted from pixel per seconds to mm per second via multiplying the field by the spatial resolution (16.2 μm per pixel).

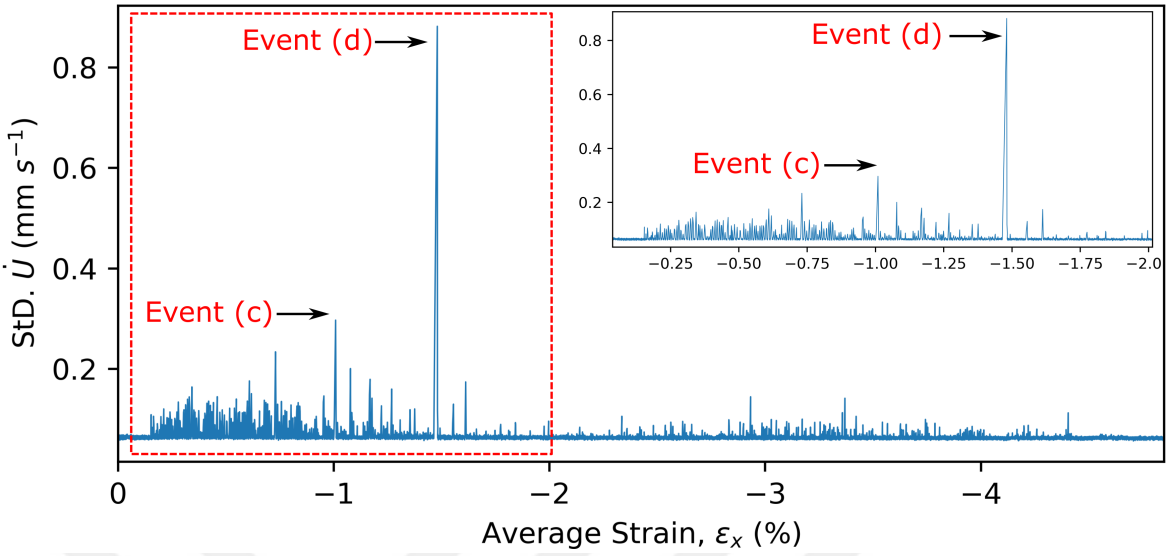

Figure 4.2. Mean strain and STD of nominal velocity field plot of Specimen 1.

In Figure 4.2, STD of nominal velocity fields [STD($\dot{U}_x(x, y)$)] are plotted versus average value of strain fields. For a homogeneous deformation, this plot should not show any sudden jumps, since STD of a (near) constant field is (near) null. However, rolled Magnesium specimens deform heterogeneously with CTB activity, and nominal velocity STD plot makes jumps whenever CTB activity is present, as shown in Figure 4.2. As discussed previously, notable serration points c and d on the stress-strain plot of Figure 4.1 indicates abrupt activity which is proven by the velocity-field-STD plot. The two highest peaks, 0.3 and 0.86 mm/s, over the STD($\dot{U}_x(x, y)$) plot are indeed associated with the serrations at points c and d shown on the stress-strain curve, respectively. The inset in Figure 4.2 zooms into first stages of the twinning (red box in the main plot) fore a better view. A similar zoom-in inset will also be provided in latter figures. After an average strain of about 1.6%, the velocity-STD plot displays considerably smaller jumps compared to the main twin plateau (points a-d). This indicates that the latter CTB activity (with more intersection with previous structures over the fully strained fields in Figure 4.1e-f) shows less heterogeneous/abrupt behavior compared with the previous CTB activity that proceeded over the maiden material.

On top of STD($\dot{U}_x(x,y)$) discussed above, two more scalar variables are derived from the fields, this time using strains (Equations 3.1, 3.2, 3.3) rather than displacements. When strain fields $[\varepsilon_x(x,y)]$ are differentiated over time, strain-rate $[\dot{\varepsilon}_x(x,y)]$ fields are obtained. Mean value and STDs of strain-rate fields are plotted against the mean strains in Figure 4.3. This is again a nominal strain-rate, similar to the nominal velocity for displacements, restricted by the sampling frequency of images. Further, another main parameter in this task that affects the results is the actual numerical (time-)differentiation scheme. Here, both forward and central difference methods are utilized for time differentiation (the first considering differences in consecutive images in the image array, while the latter takes the differences over every second image). Forward difference STD plot fails to track the CTB activities (events are not distinguishable due to the baseline error) where central difference STD plot can display the heterogeneous twin activity (resembles to the velocity STD plot in 4.2).

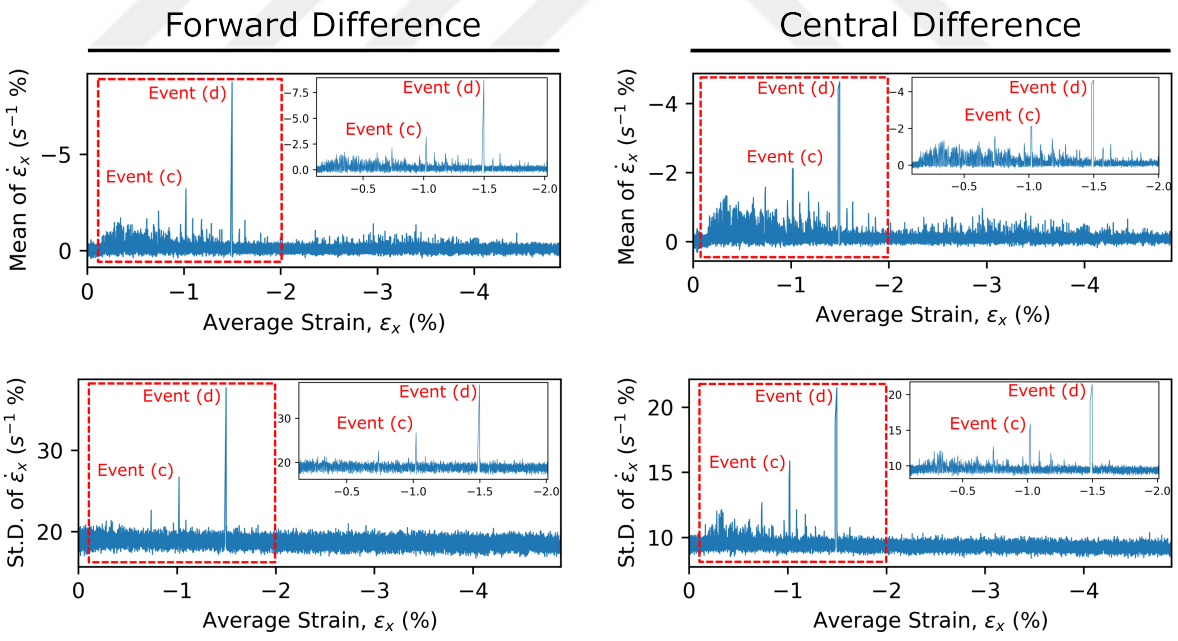

Figure 4.3. Mean and STDs of strain-rate field versus average of strain field plots for Specimen 1. strain-rate is calculated by utilizing forward and central difference.

One observes over Figure 4.3 that the mean and STD of nominal strain-rate fields (computed with central differences) show a different behavior for the CTB activity after

1.6% average strain: Here, the STD($\dot{\varepsilon}_x(x,y)$) plot shows very limited jump signal, while the Mean($\dot{\varepsilon}_x(x,y)$) plot continuously gives signal due to the ongoing deformation. (As expected, the mean is insensitive to the spatial distribution of strain accommodation, i.e., whether it is homogeneous heterogeneous.). This difference indicates that later CTB activity and slip systems are not localized enough to create a sufficient strain-rate-field STD that is higher than baseline error which arises from the DIC error. Similar behavior is also observed at the Figure 4.2 where below 1.6% mean strain STDs are considerably larger than after 1.6% mean strain STDs. Significant difference between the values of central difference mean and STD plots indicates that there are distinct strain-rate regions within the field which that lowers the mean and increases the STD. However, the characteristics of the plots can still indicate the CTB events. STD and mean values always make a jump with presence of a localized region on the strain-rate field due to a CTB activity.

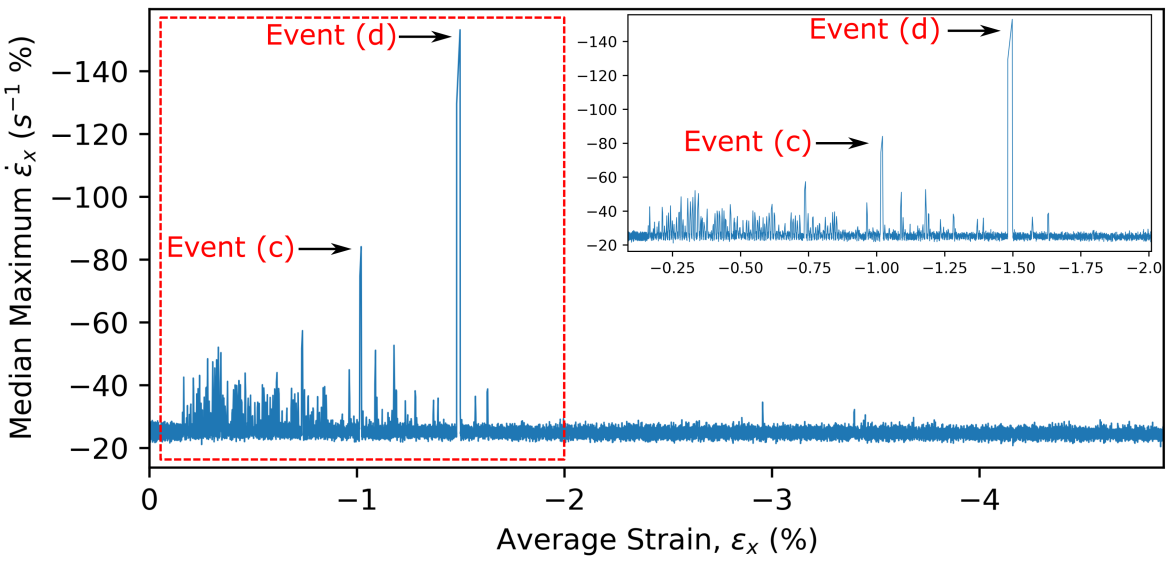

Figure 4.4. Median value of maximum 1% of the strain-rate (median maximum) field versus mean strain for Specimen 1.

On top of STD($\dot{U}_x(x,y)$), Mean($\dot{\varepsilon}_x(x,y)$), STD($\dot{\varepsilon}_x(x,y)$), previously defined, a fourth scalar variable aims to track the strain-rate of the CTB bands more directly. If a localized CTB event present, the strain-rate values inside the incremental band

advance are expected to be significantly higher than the rest of the field. To find the CTB strain-rates, the highest 1% of the strain-rate data are filtered and these are indeed found to be inside the band advances by visual inspection. For robustness, the median of these (maximal) values is considered as the scalar measure (median is effective in removing any non-physical outliers). We name this data as "median maximum". Median maximum values are plotted against the average strains in Figure 4.4. The characteristic shape of the plot resembles the central difference strain-rate STD plot at the Figure 4.3.

Two unique event points are selected on Figure 4.4 (Event c and Event d) for further investigation. Deformation history of the CTB event at $\varepsilon_{x,mean} = -1.01\%$ (Event c, which is associated with the serration at point c in Figure 4.1) is shown in Figure 4.5. Figure 4.5a represents the overall strain field change with the event where the associated CTB is indicated with black arrow. This is a CTB initiation event because the band is not present at the initial strain field. Overall change of mean strain is 0.01%. Figures 4.5b-f shows the sequential field changes of nominal velocity (left) and forward difference strain-rate (right). Figures 4.5c-e are the points where CTB initiation happens. In velocity plot of Figure 4.5c, the field separates into a dual zone from the bottom left corner of the field and slowly dissipates along the upper part of the field. At the strain-rate plot, the band initiation can be distinguished and shown with black arrow. The main portion of the deformation advance takes place in the time increment of Figure 4.5d, where the velocity fields are visibly separated by the CTB region (high displacement gradients are present) and the strain-rate forms a clear band with median maximum of $\dot{\varepsilon}_{x,band} = -129\%\ s^{-1}$. Then, the event starts to dissipate in Figure 4.5e, where the velocity field and band strain-rate diminishes. Hence, this particular event is captured within three consecutive images Figure 4.5c-e.

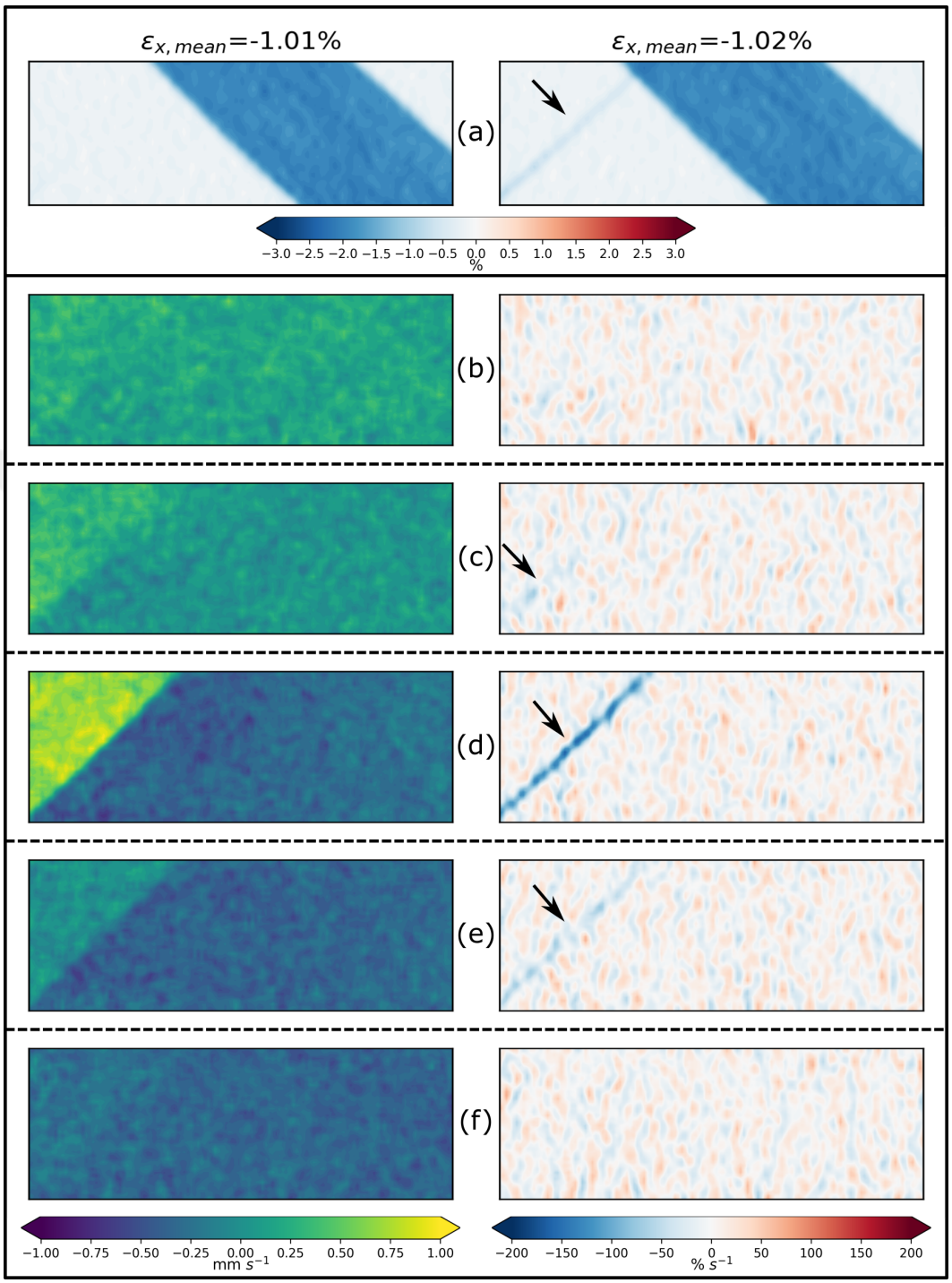

Figure 4.5. Sequential history of the CTB event at $\varepsilon_{x,mean} = -1.01\%$ on Specimen 1. (a) Initial-final strain fields of the event. (b-f) Sequential history, nominal velocity field at left-hand side and forward difference strain-rate field at right-hand side.

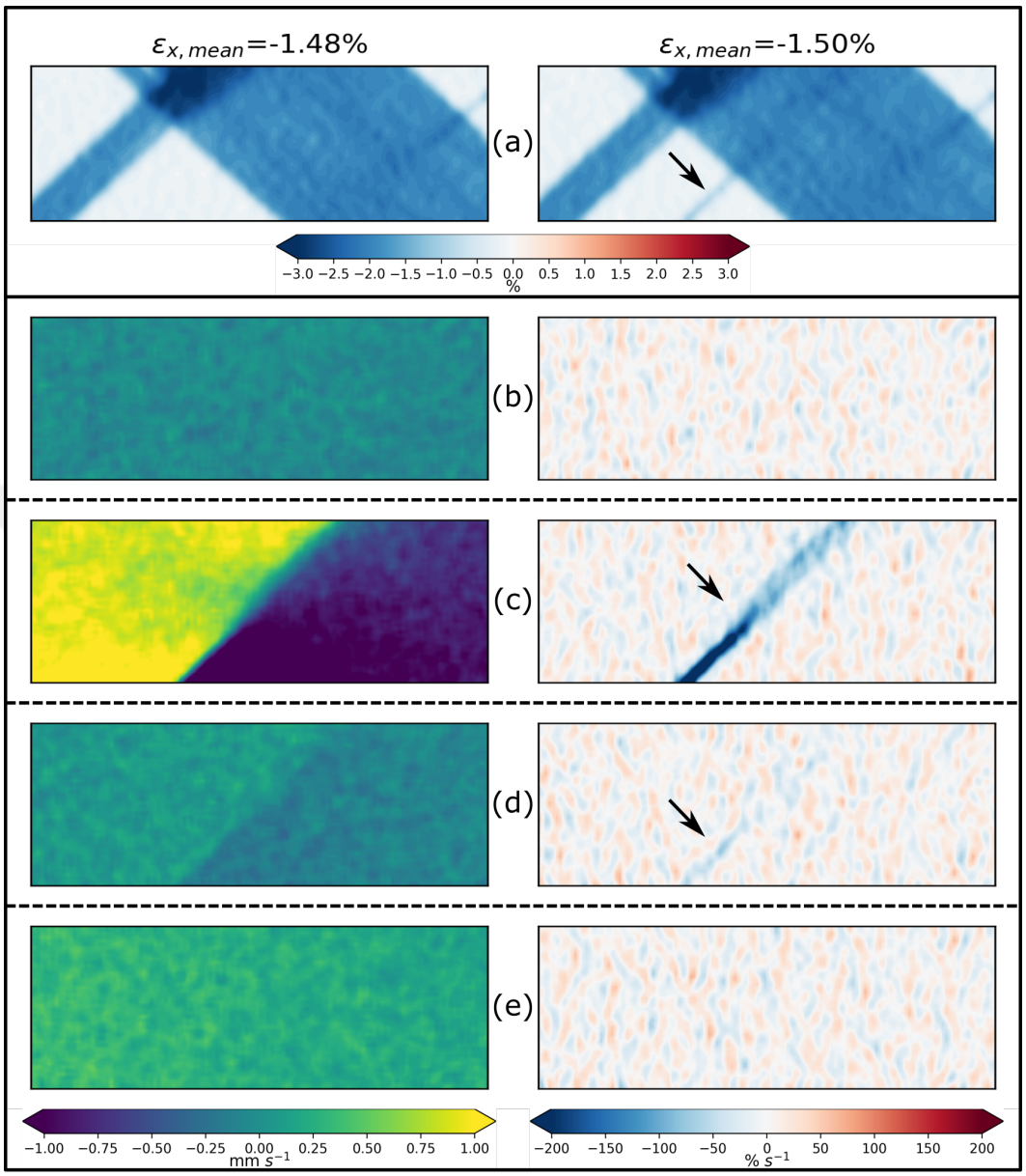

Figure 4.6. Sequential history of the CTB event at $\varepsilon_{x,mean} = -1.48\%$ on Specimen 1. (a) Initial-final strain fields of the event. (b-e) Sequential history, nominal velocity field at left-hand side and forward difference strain-rate field at right-hand side.

The history of CTB activity which is associated with the highest peak of the Figure 4.4 (Event d, which is associated with the serration at point d in Figure 4.1) is presented on Figure 4.6. Figure 4.6a, shows the initiation of the secondary CTB band indicated with black arrow on the strain maps. Overall change of mean strain is 0.02%. Figures 4.6c-d, shows the CTB activity. Velocity field is separated by the CTB

region with higher deformation gradient than the CTB presented in Figure 4.5 and strain-rate of the band is more concentrated. Band strain-rate of this particular CTB is measured with same methodology and came out as $\dot{\varepsilon}_{x,band} = -256\%\ s^{-1}$. The reason of using smaller colorbar for the plots is the event at Figure 4.6d. Abrupt attack of the CTB fades away with less distinct velocity and strain-rate fields. This CTB shows the behavior of an intersecting CTB. From Figure 4.6a, the associated band shown with the black arrow crosses over the primary monolithic twin band. The distribution of the both velocity and strain-rate fields significantly changes at the intersection region. The velocity field is separated less sharply due to lower displacement gradients at intersecting region. In addition, the strain-rate of the band diffuses widely within this region. In Figure Figure 4.6d, strain-rate of the fading band shows the same behavior, becomes less visible at the intersection region. This CTB event is observed within two consecutive images.

To track the behavior and speeds of observable CTB activities, median maximum plot given in Figure 4.4 is used. The plots obtained from central difference strain-rate data (Mean($\dot{\varepsilon}(x, y)$), STD($\dot{\varepsilon}(x, y)$ and median maximum plots) are quantitatively smoothed due to the reduction of the time resolution ($2\Delta t$ denominator of the Equation 3.5). However, central difference results track the CTB events better than the forward difference. The threshold value is determined as the mean of the median maximum values minus two times of the STD of the median maximum values of the plot given in Figure 4.4. Data points standing above this threshold are taken and investigated for abrupt-band-advance event duration. Table 4.1 shows the results of this effort. Number of CTB advance events are paired with the number of consecutive images that captured those individual events. Approximately 50% of the CTB initiation/expansion events are recorded within two consecutive images. Weighted average of the Table 4.1 yields to 1.947 average images.

Table 4.1. Number images recorded for each CTB event for Specimen 1.

	1 Image	**2 Images**	**3 Images**
Number of Events	26	48	21

4.2. Regional Analysis of Rolled Specimen 2 Under 0.001 strain-rate

With equivalent conditions of Specimen 1 (the first experiment), the second experiment is conducted on Specimen 2 (Figure 3.3) with low strain-rate compression ($\dot{\varepsilon} = -0.001\ s^{-1}$). Before the loading, pre-load of 150 N is given. The loading is position-controlled and implemented displacement rate is 1.5 mm/min. Regional analysis figures are resolved at 1120 pixels in width and 300 pixels in height. The camera could go up to 998 Hz of acquisition frequency with that resolution. 40368 images are taken with the maximum frequency (998 Hz) while the specimen is loaded during the experiment. Load data is converted to the engineering stress data by dividing the load data to the cross-sectional area of 79 mm^2. The ROI of this experiment is a regional area instead of full-field analysis (Figure 3.5). Therefore, instead of DIC mean strain data, nominal strain values are used to construct the stress-strain plot given in Figure 4.7. Nominal strain values are calculated by dividing the displacement data obtained from the crosshead position of the uniaxial loading device to the specimen height of 25.02 mm.

In Figure 4.7, the yielding starts at approximately 77 MPa and maximum stress goes up to the 114 MPa. Strain maps at Figure 4.7a-f shows ε_{xy} fields because the camera is rotated by 45°. Hence, recalling Section 2.4, CTBs with same strain tensor are exactly parallel now which only yields ε_{xy} and ω_{xy} with negligible ε_x and ε_y with respect to camera coordinates. To prevent any misunderstanding in this Figure, it should be noted that the nominal strain on the stress-strain curve has no relation with the ε_{xy} of the strain maps a-f. The nominal strain represents the whole material strain obtained from the LVDT where ε_{xy} represents the strains within the camera ROI obtained from DIC post-processing.

A major CTB origins at the top of Figure 4.7a. This band expands as a monolithic shape across the Figures 4.7a-d, indicated with the arrows. Characteristic band strain of this CTB is $\varepsilon_{xy} = 1.78\%$. This band is not perfectly parallel to the DIC ROI possibly due to minor manufacturing errors. When the principal strains are calculated,

the maximum in-plane band shear strain found as Max(ε_{xy}) = 1.95%. Maximum band shear strain came out logical because the principal strains are in agreement with Specimen 1 ($\varepsilon_x = -1.97\%$, Specimen 1 strain is already in principal configuration where $\varepsilon_{xy} \approx 0\%$) which is extracted from the same Magnesium plate.

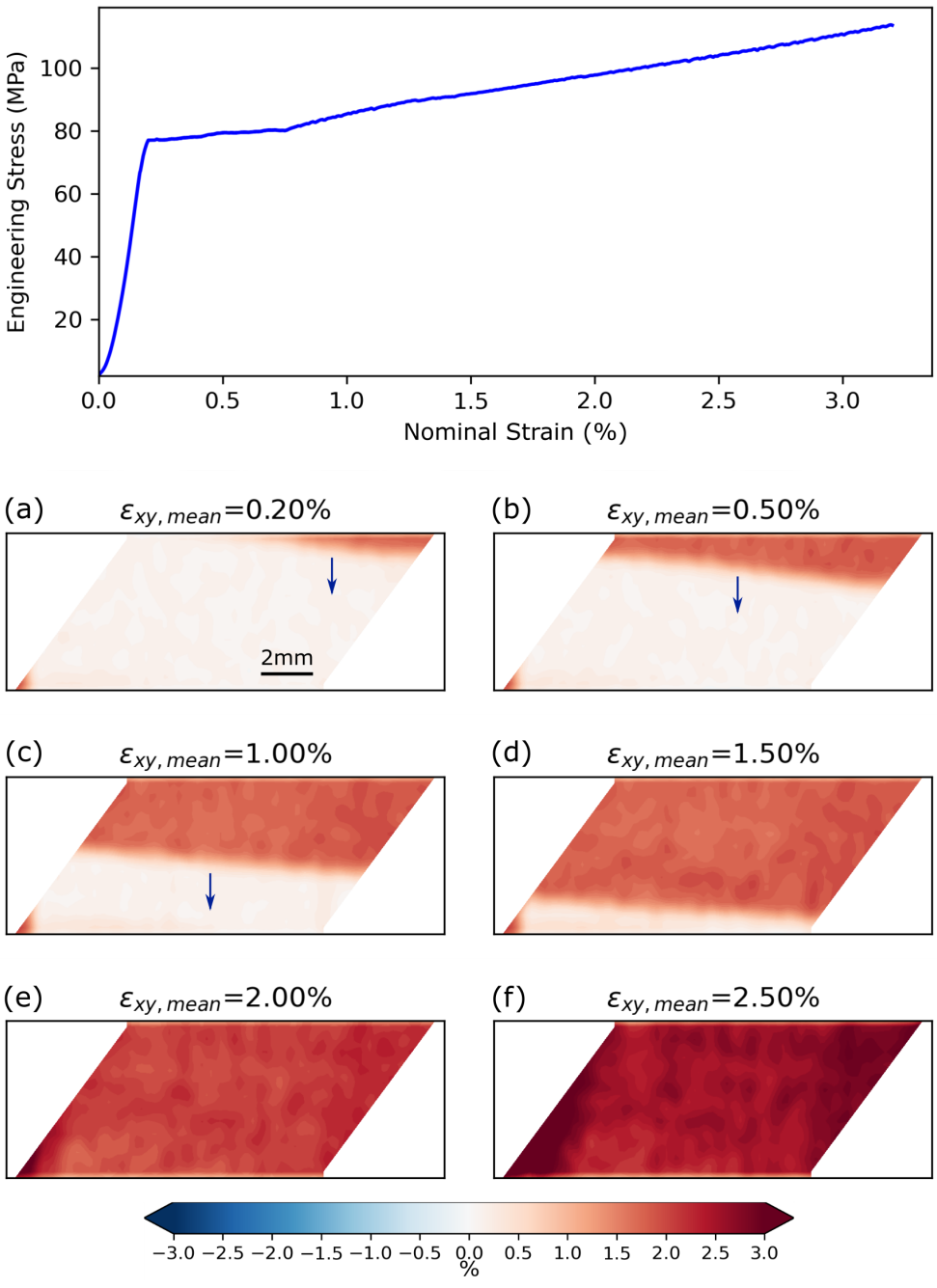

Figure 4.7. Stress-strain plot of Specimen 2. ε_{xy} strain maps of selected moments (a-f) are shown.

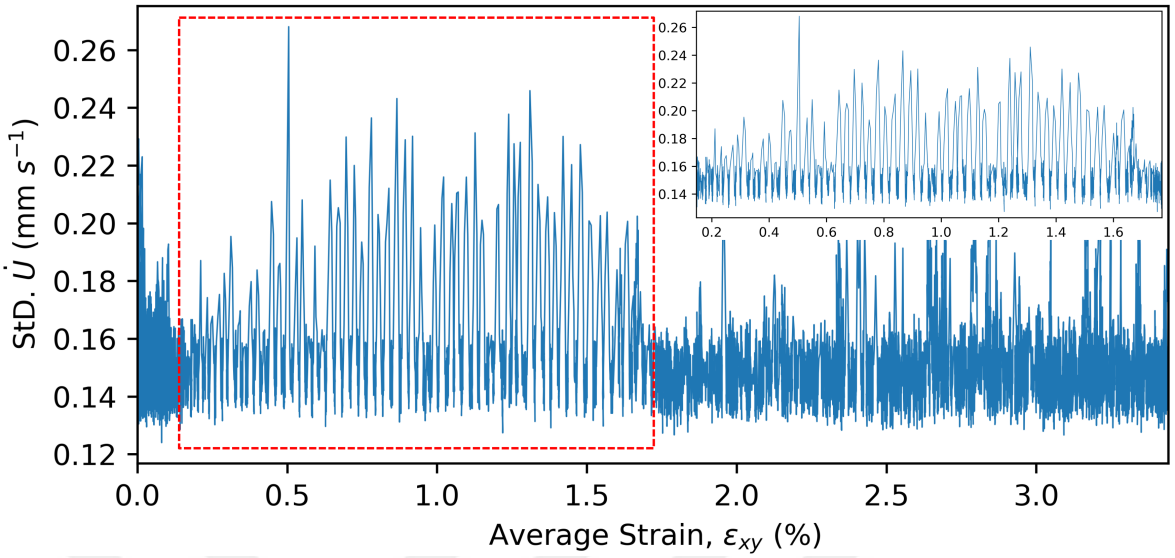

Figure 4.8. Mean strain and STD of nominal velocity field plot of Specimen 2. Velocity field is converted from camera coordinates to specimen coordinates.

The first scalar variable, the STD of nominal velocity field, is plotted against the average strain in Figure 4.8. The velocity field is calculated by considering the specimen coordinates instead of the DIC coordinates (image coordinates). Therefore, velocity field denotes the time derivative of displacement field along the compression direction (RD of the specimen, see Figure 3.5). Time derivative of displacement field is taken via forward difference method with step size of $\Delta t = 1$ ms. The velocity field units are converted from pixel per second to mm per second via multiplying the field by the spatial resolution (16.2 μm per pixel). Step-wise CTB activity can be seen from the plot, each indicating an expansion event of the monolithic CTB.

The second and third scalar variables, namely mean and STD of strain-rate field, are calculated by utilizing both forward and central difference methods with $\Delta t = 1$ ms step size. Mean and STD of strain fields are plotted against the average strain in Figure 4.9. STD plot of forward difference behaves similarly with Specimen 1 results (Section 4.1), fails to indicate the CTB activities. On the other hand, STD plot of central difference can track the heterogeneous twin activity better and shows resembling shape with velocity STD plot in 4.8). Figure 4.9 central difference mean and STD plots show

similar behavior with Specimen 1 after primary CTB plateau. After 1.74% average strain, central difference STD plot considerably low number of jumps but mean plot continuously gives signal due to ongoing deformation. In Figure 4.7d-f, monolithic band fills the region at around 1.7% strain-rate and the strain of the field increases partially homogeneously (Figure 4.7d-e).

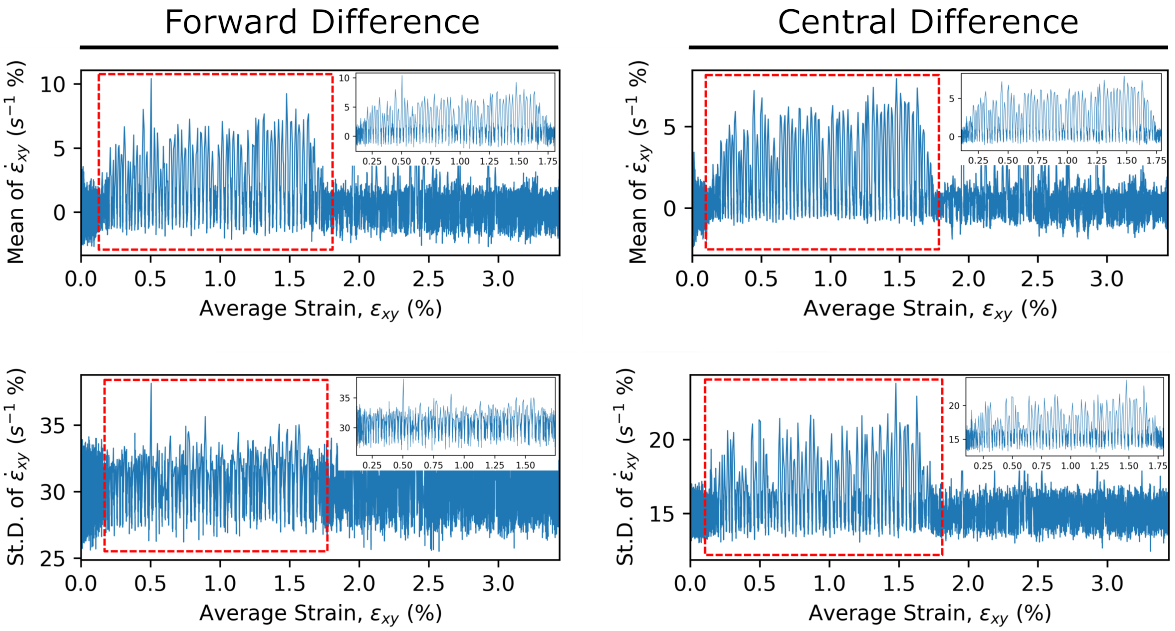

Figure 4.9. Mean and STDs of strain-rate field versus average of strain field plots for Specimen 2. strain-rate is calculated by utilizing forward and central difference.

The fourth scalar variable, median maximum, values are plotted against the average strains in Figure 4.10. The peaks and shape of the median maximum plot highly resembles the central difference strain-rate STD plot in the Figure 4.9. Area fraction increase of the monolithic CTB happens with step-wise local strain-rate bands which can be seen on the magnified image of the red-dashed box. Unlike Specimen 1 (Figure 4.4), there are not explosive events present where the band strains is not significantly deviated from the average.

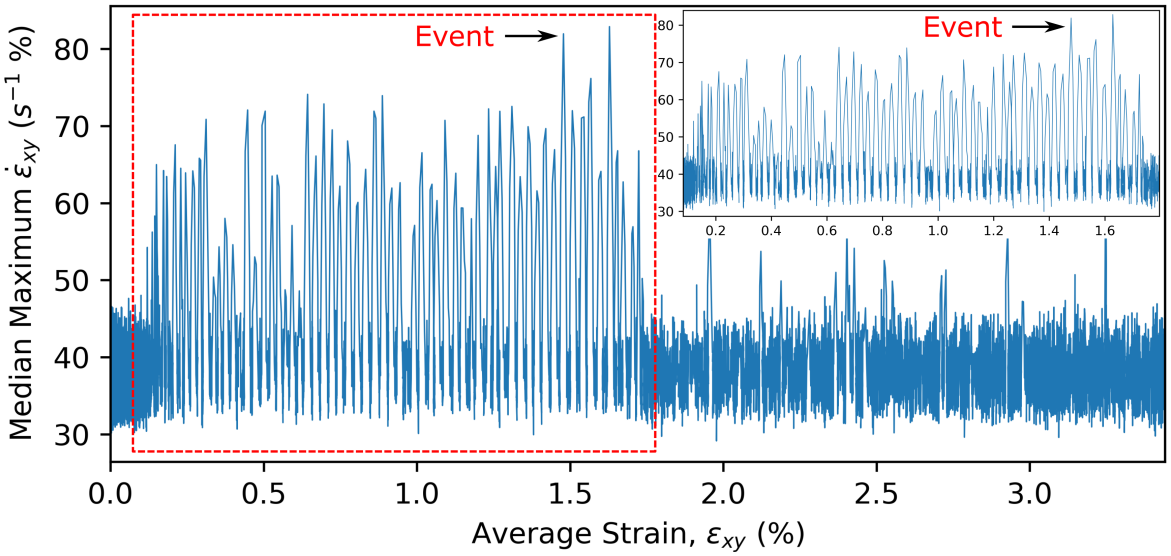

Figure 4.10. Median value of maximum 1% of the strain-rate (median maximum) field versus mean strain for Specimen 2.

One event point is selected on the Figure 4.10 for further investigation. Deformation history of the CTB event at $\varepsilon_{xy,mean} = 1.47\%$ is shown in Figure 4.11. Figure 4.11a represents the overall strain field change with the event where the edge of the associated CTB is indicated with black arrow. This is a CTB expansion event because the band expands towards the bottom of ROI. Overall change of mean strain is 0.02%. Figures 4.11b-f shows the sequential field changes of nominal velocity (left) and forward difference strain-rate (right). Figures 4.11c-e are the points where CTB expansion happens. At velocity plot of Figure 4.11c, the field is visibly start to separate by the horizontal CTB expansion line. At the strain-rate plot, the band initiation can be distinguished and shown with black arrow. The main event takes place at Figure 4.11d-e, where the velocity fields are visibly separated by the CTB expansion line and the strain-rate forms a clear band with median maximum of $\dot{\varepsilon}_{xy,band} = 100\%\ s^{-1}$ for point d and $\dot{\varepsilon}_{xy,band} = 105\%$ for point e. Then, the event is dissipated in Figure 4.11f, where the velocity field and band strain-rate returns to normal. This particular event is captured within three consecutive images.

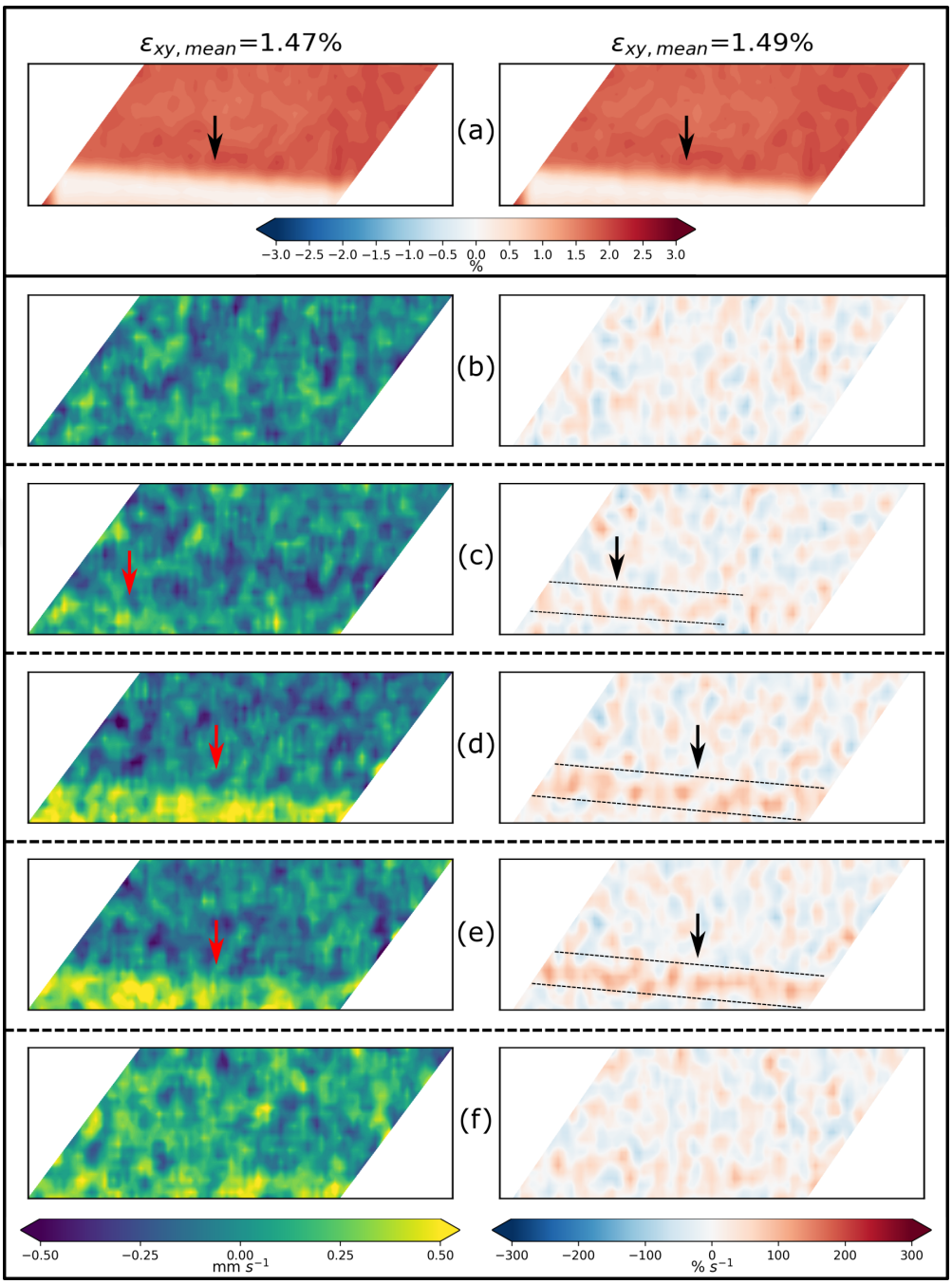

Figure 4.11. Sequential history of the CTB event at $\varepsilon_{xy,mean} = 1.47\%$ on Specimen 2. (a) Initial-final strain fields of the event. (b-f) Sequential history, nominal velocity field at left-hand side and forward difference strain-rate field at right-hand side.

To determine how many images captured each CTB expansion events, the data points above a threshold median max in Figure 4.10 are investigated. The threshold value is determined as the mean of the median maximum values plus two times of the

STD of the median maximum values of the Figure 4.10. Data points standing above this threshold are taken and investigated for event duration. In Table 4.2, number of images captured for CTB events and their duration are presented. Number of CTB events are paired with the number of consecutive images that captured those individual events. Approximately 82% of the CTB expansion events are recorded within one, three and four consecutive images. Weighted average of the Table 4.1 yields to 2.820 average consecutive images that CTB activities take place within.

Table 4.2. Number images recorded for each CTB event on Specimen 2.

	1 Image	**2 Images**	**3 Images**	**4 Images**	**5 Images**
Number of Events	26	7	22	25	9

4.3. Full-Field Analysis of Rolled Specimen 3 Under 0.01 strain-rate

The third experiment is conducted on Specimen 3 (Figure 3.3) with high strain-rate compression ($\dot{\varepsilon} = -0.01\ s^{-1}$). Before actual loading, pre-load of 150 N is given. The loading is position-controlled and implemented displacement rate is 15 mm/min. Full-field analysis figures are resolved at 1400 pixels in width and 600 pixels in height. The camera could go up to 532 Hz of acquisition frequency with the implemented resolution. 3192 images are taken with the maximum frequency (532 Hz) while the specimen is loaded during the experiment. All images are analysed with respect to the initially taken reference image via DIC. Load data is obtained from the load cell and mean strain data is calculated for each image with DIC and post-processing. Load data has less sampling (647) than the DIC mean strain data (3192). Therefore, the load data is upscaled to the size of 3192 by inserting intermediate points via equal spacing interpolation. Then, the load data is converted to the engineering stress data by dividing the load data to the cross-sectional area of 104 mm^2. Finally, stress and mean strain values are paired together to obtain the stress-strain curve that is shown in Figure 4.12.

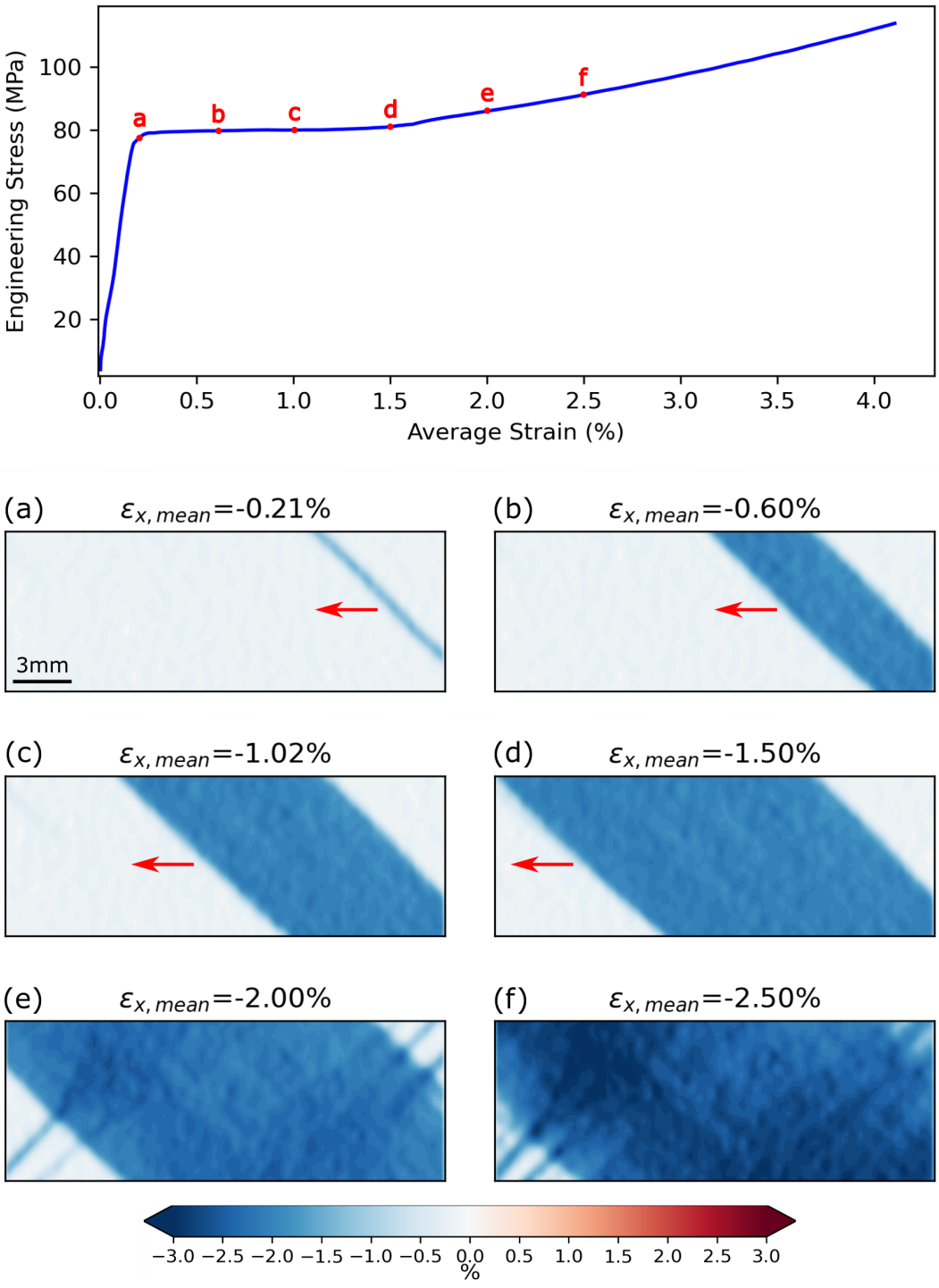

Figure 4.12. Stress-strain plot of Specimen 3. ε_x strain maps are shown on selected points of a, b, c, d, e and f on the curve to display the deformation history.

Initial yielding starts at approximately 78 MPa, initiated with a localized CTB attack shown in Figure 4.12a. The expansion of this particular CTB (arrows in Fig-

ures 4.12a-b) is the major deformation element over the twinning plateau with a monolithic structure observed over Figures 4.12a-e. Average twin band strain is measured via taking the average of the subset strains inside CTB region in Figure 4.12d and characteristic twin band strain is calculated -2.01% which is approximately similar with Specimens 1 and 2. Secondary CTB formations starts to initiate after ε_x = -1.58% mean strain at Figures 4.12e-f. Beforehand introduction of the secondary CTB bands, sole expansion of monolithic CTB in Figures 4.12a-d shows perfect plastic behavior where the stress-strain curve is perfectly horizontal with no trace of hardening at region between ε_x = -0.2% and ε_x = -1.58%.

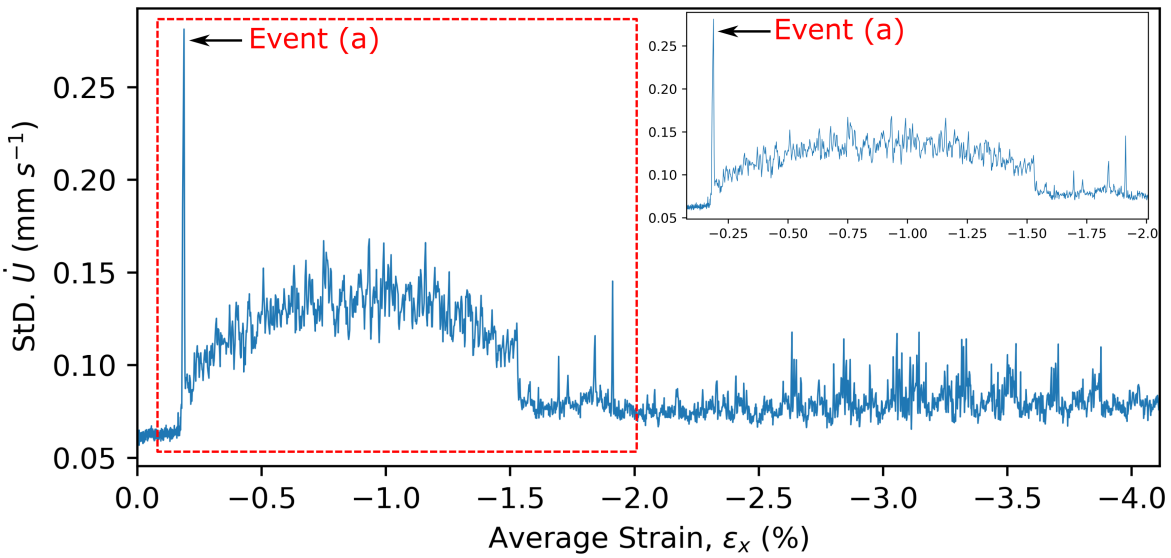

Figure 4.13. Mean strain and STD of nominal velocity field plot of Specimen 3.

The first scalar variable, STD of nominal velocity field, is obtained by differentiating the displacement field against time via forward difference method with step size of Δt = 1/532 s. This variable is plotted against the strain field average in Figure 4.13. The plot indicates that there is an initial high amplitude CTB formation at ε_x = -0.18% average strain. This band is shown in Figure 4.12a. After the initial formation of the CTB, continuously elevated field of velocity STD is observed. STD values returns to baseline after the complete formation of the monolithic CTB. This baseline point coincides with the hardening starting point where secondary CTB formations

occur and crosses over the monolithic CTB (around ε_x = -1.58%). The peaks after these point are related with multiple secondary CTB formation and expansion events shown in Figure 4.12e.

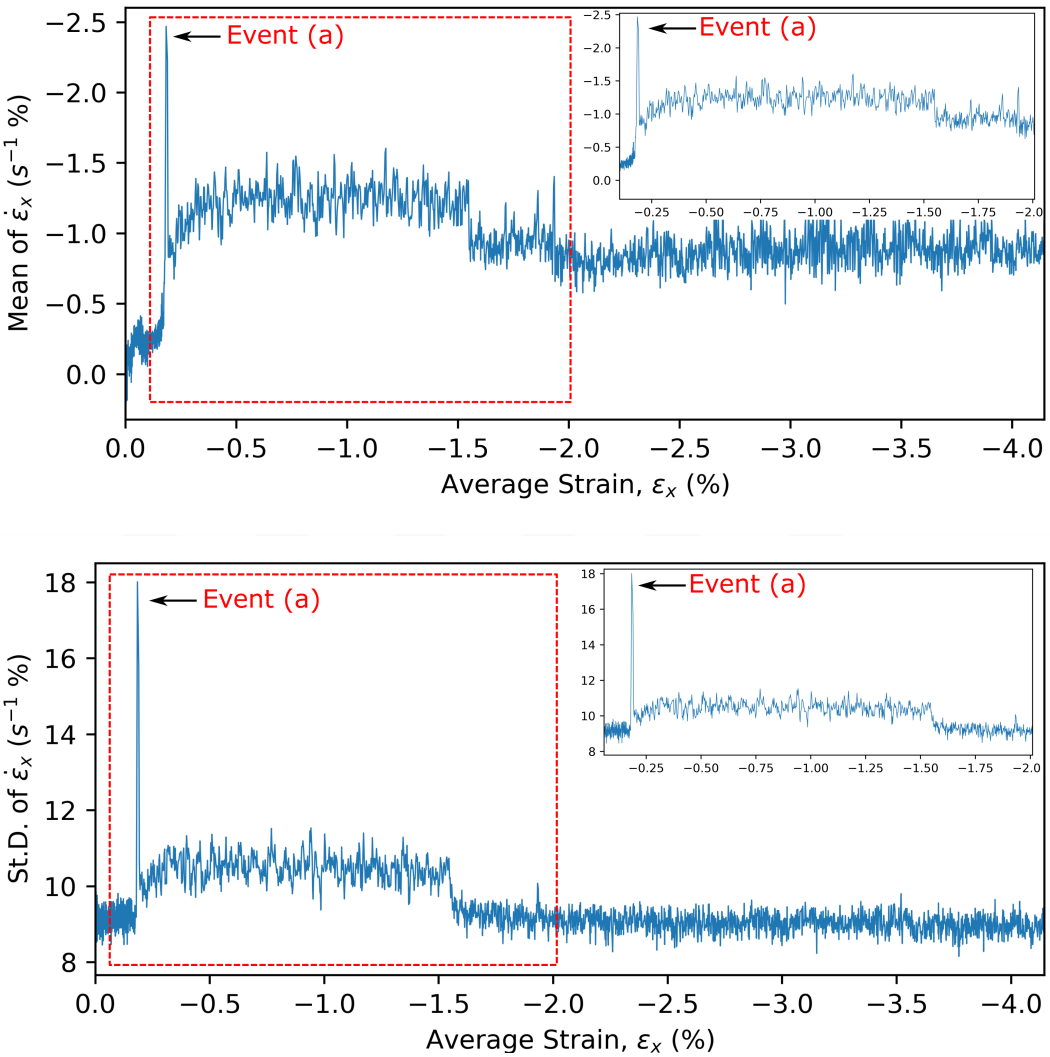

Figure 4.14. Mean and STDs of strain-rate field versus average of strain field plots for Specimen 3. strain-rate is calculated by utilizing central difference.

The second and third scalar variables, namely mean and STD of the strain-rate fields, are derived via central time difference of strain fields with step size of $2\Delta t = 2/532$ s. These variables are plotted against mean strains in Figure 4.14. Mean and STD plot shapes resembling each other at the monolithic CTB expansion region (between ε_x = -0.2% and ε_x = -1.58%). The initial formation of this band is indeed an

abrupt event with high strain-rate content, proving each other with velocity data (same high amplitude peaks are observed at velocity plot). Both mean and STD of strain-rates show continuously uniform deformation profile. CTB activity peak points are not separated from each other with intermediate data points at baseline region (steady-state region). This behavior of plots indicates that there is not a precise spacing between the CTB events that individually separates them from each other like Specimen 1 and 2 and twinning events. Another different behavior from the previous experiments is baseline elevation of the strain-rate mean plot after the main twin plateau due to the one order higher applied strain-rate.

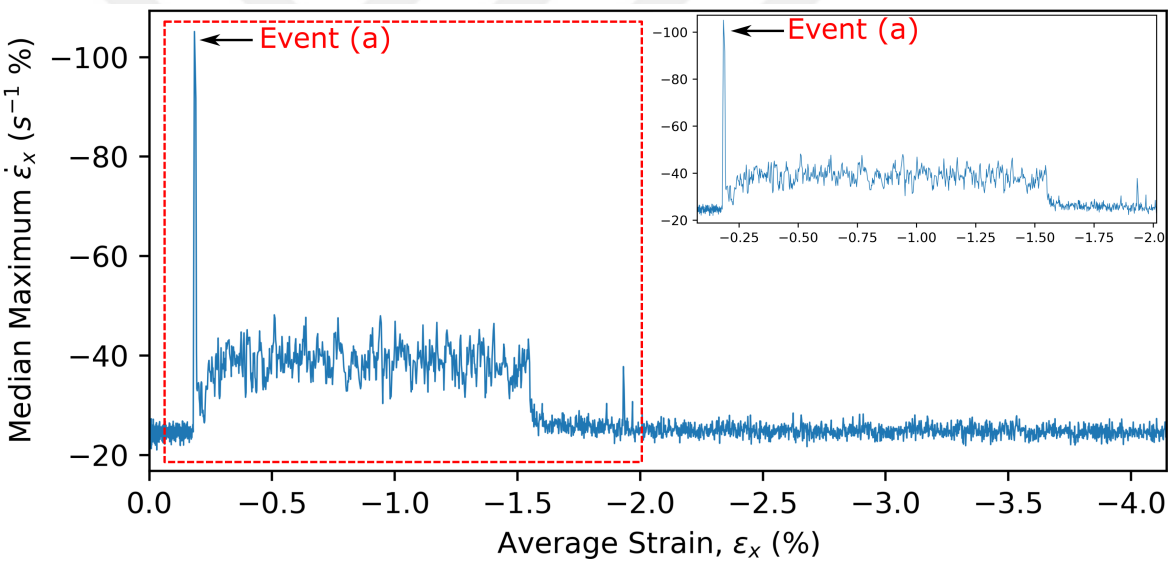

Figure 4.15. Median value of maximum 1% of the strain-rate (median maximum) field versus mean strain for Specimen 3.

The fourth scalar, median maximum, values are plotted against the average strains in Figure 4.15. The characteristic shape of the plot resembles the central difference strain-rate STD plot at the Figure 4.14. Excluding the initiation of the monolithic CTB event (denoted as "Event a" in the Figure 4.15) the strain-rates of the CTB expansion bands does not deviate significantly like the one observed in Specimen 1 (Figure 4.4, same experiment with lower strain-rate). Band activities associated with

secondary CTBs are only distinguishable at points of $\varepsilon_x = -1.86\%$, $\varepsilon_x = -1.93\%$ and $\varepsilon_x = -1.97\%$. Later CTB and slip activities results in no localized strain-rate regions.

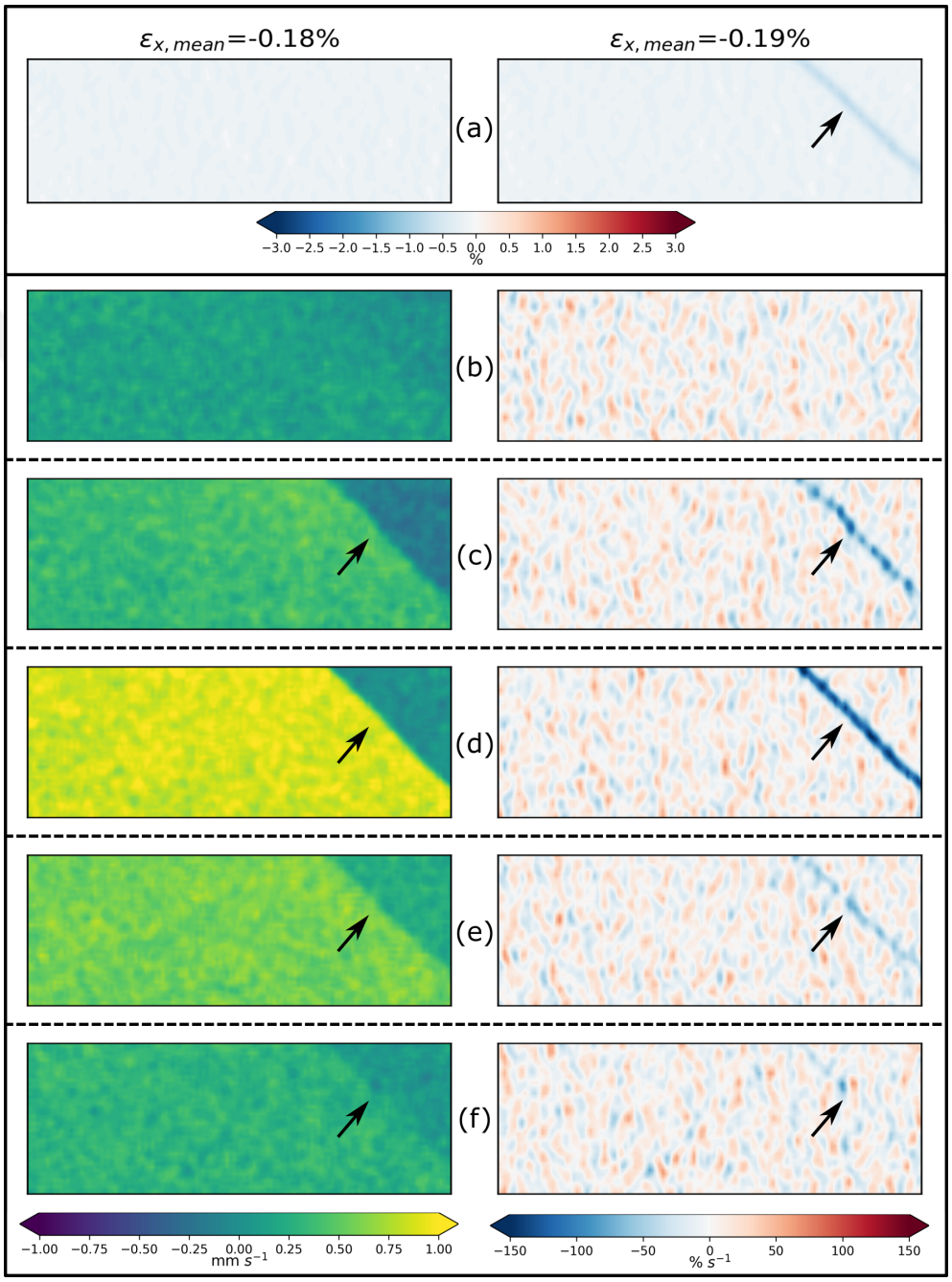

Figure 4.16. Sequential history of the CTB event at $\varepsilon_{x,mean} = -0.18\%$ on Specimen 3. (a) Initial-final strain fields of the event. (b-f) Sequential history, nominal velocity field at left-hand side and forward difference strain-rate field at right-hand side.

The highest strain-rate event (initial CTB formation event (Figure 4.12a)) on the Figure 4.15 is investigated further. Deformation history of the CTB event at $\varepsilon_{x,mean} = -0.18\%$ is shown in Figure 4.16. Figure 4.16a represents the overall strain field change with the event where the associated CTB is indicated with arrow. This is the initiation event of the monolithic CTB. Overall change in mean strain is 0.01%. Figures 4.16b-f shows the sequential field changes of nominal velocity (left) and forward difference strain-rate (right). Figures 4.16c-d are the point where CTB initiation happens. The main event takes place at Figure 4.16d, where the velocity fields are sharply separated by the CTB region and the strain-rate forms band with median maximum of $\dot{\varepsilon}_{x,band} = -136\%\ s^{-1}$. Then, the event starts to dissipate in Figure 4.16e, where the velocity field and band strain-rate diminishes.

Unlike low strain-rate loading experiments (Specimens 1 and 2), the end point of the CTB event presented in Figure 4.16 is not present. CTB activity still continues in Figure 4.16f with visibly separated velocity field. In Figure 4.17, similar deformation history of an arbitrary point on the monolithic CTB expansion ($\varepsilon_{x,mean} = -0.61\%$) is shown. From Figure 4.17b-f, it can be clearly seen that the individual CTB activities do not dissipate with a certain velocity/strain-rate map (maps with no bands present). After the end of an individual CTB activity, another one immediately starts and our acquisition frequency can not capture the small time interval between them where the material field is steady (no CTB activity is present). This is the reason that our scalar value plots (Figures 4.13, 4.14 and 4.15) are continuously elevated with respect to the baseline. Therefore, unlike low strain-rate loading experiments, we can not assess and correlate the CTB events with number of images that captured them individually. On the other hand, we can determine the average strain-rate of these continuous expansion bands for the monolithic CTB which is measured as $\dot{\varepsilon}_x = -53.87\%\ s^{-1}$.

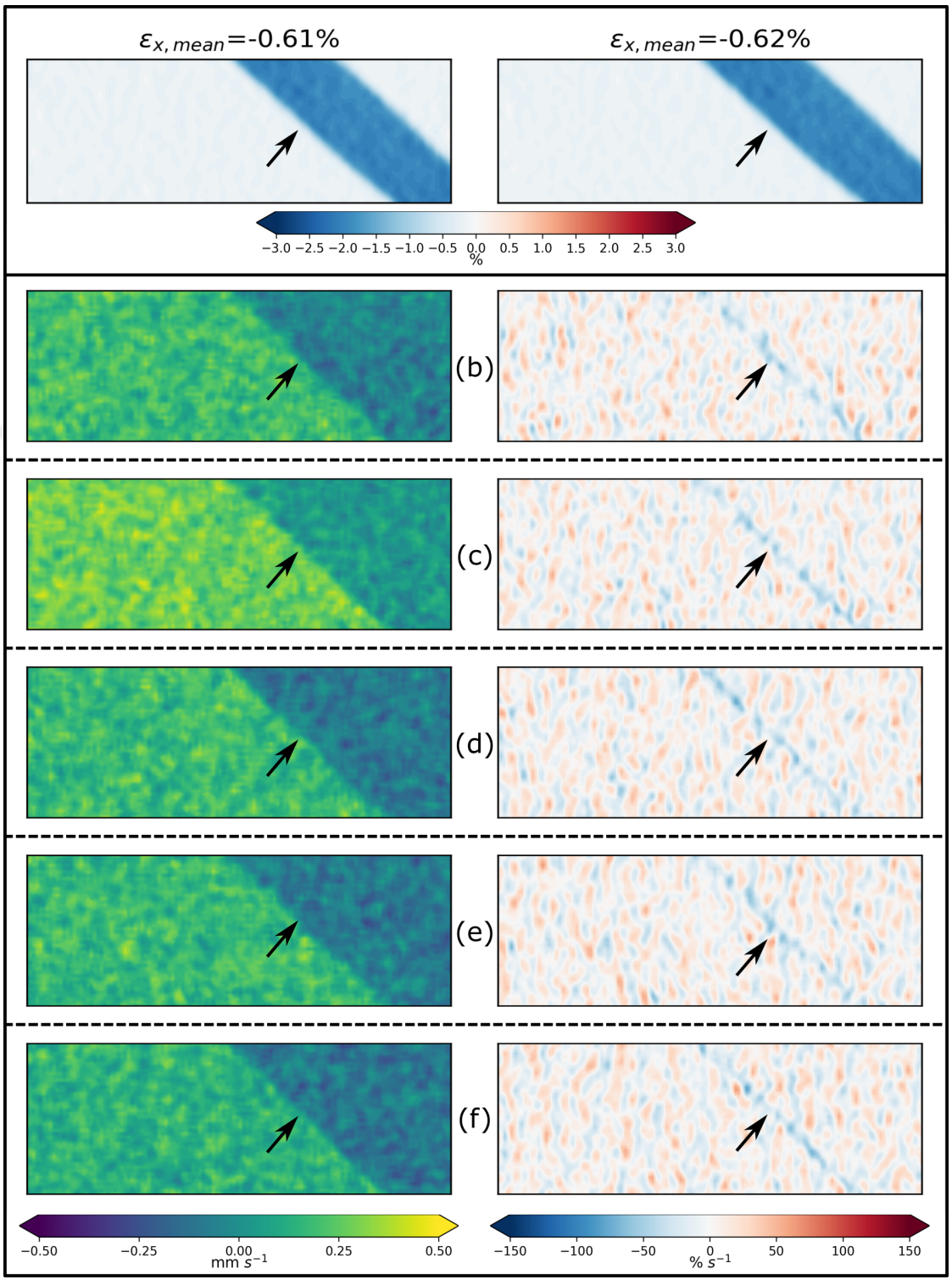

Figure 4.17. Sequential history of the CTB event at $\varepsilon_{x,mean} = -0.61\%$ on Specimen 3. (a) Initial-final strain fields of the event. (b-f) Sequential history, nominal velocity field at left-hand side and forward difference strain-rate field at right-hand side.

4.4. Regional Analysis of Rolled Specimen 4 Under 0.01 strain-rate

The fourth experiment is conducted on Specimen 4 (Figure 3.3) with high strain-rate compression ($\dot{\varepsilon} = -0.01\ s^{-1}$). Before the loading, pre-load of 150 N is given. The loading is position-controlled and implemented displacement rate is 15 mm/min. Regional analysis figures are resolved at 1120 pixels in width and 300 pixels in height. The camera could go up to 998 Hz of acquisition frequency with that resolution. 4075 images are taken with the maximum frequency (998 Hz) while the specimen is loaded during the experiment. Load data is converted to the engineering stress data by dividing the load data to the narrowest cross-sectional area of 81 mm^2. The ROI of this experiment is a regional area instead of full-field analysis. Therefore, instead of DIC mean strain data, nominal strain values are used to construct the stress-strain plot given in Figure 4.18. Nominal strain values are calculated by dividing the displacement data obtained from the crosshead position to the specimen height of 25.02 mm.

In Figure 4.18, the yielding starts at approximately 78 MPa and maximum stress goes up to the 110 MPa. Strain maps at Figure 4.18a-f shows ε_{xy} fields because the camera is rotated by 45°. The nominal strain on the stress-strain curve should not be mistaken with the ε_{xy} of the strain maps a-f. The nominal strain represents the whole material strain obtained from the LVDT where ε_{xy} represents the strains within the camera ROI obtained from DIC post-processing.

Initial CTB activity differs from the Section 4.2 where first two vertical twin bands initiate from the right side of the ROI. These are elements of complementary -45° activity in the unrotated coordinate system (Figure 2.6). After the initiation, these vertical bands stays dormant until the major horizontal CTB fills the field (Figure 4.18f. A major horizontal CTB origins at the top of Figure 4.18a. This band expands as a monolithic shape across the Figures 4.18a-e, indicated with the arrows. Then, this band meets with another horizontal band at the bottom of ROI which was formed between Figures 4.18a-b. Characteristic band strain of the monolithic CTB is $\varepsilon_{xy} = 1.77\%$. This band is not perfectly parallel to the DIC ROI due to minor manufacturing errors.

When the principal strains are calculated, the maximum in-plane band shear strain found as Max(ε_{xy}) = 1.94%. Maximum band shear strain came out logical because it is approximately same strain with the band strains of the Specimens 1-3 (Sections 4.1, 4.2 and 4.3).

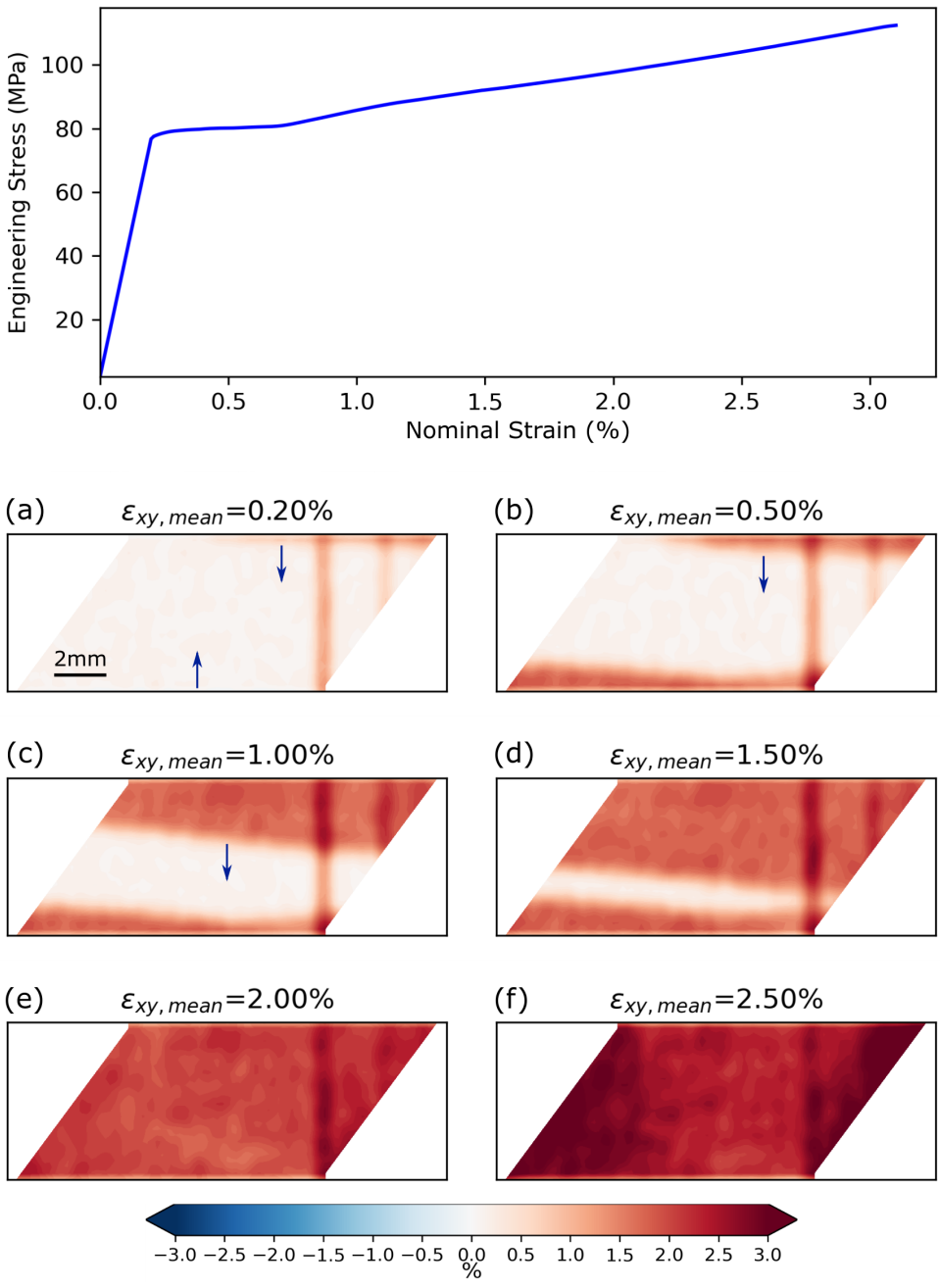

Figure 4.18. Stress-strain plot of Specimen 4. ε_{xy} strain maps of selected moments (a-f) are shown

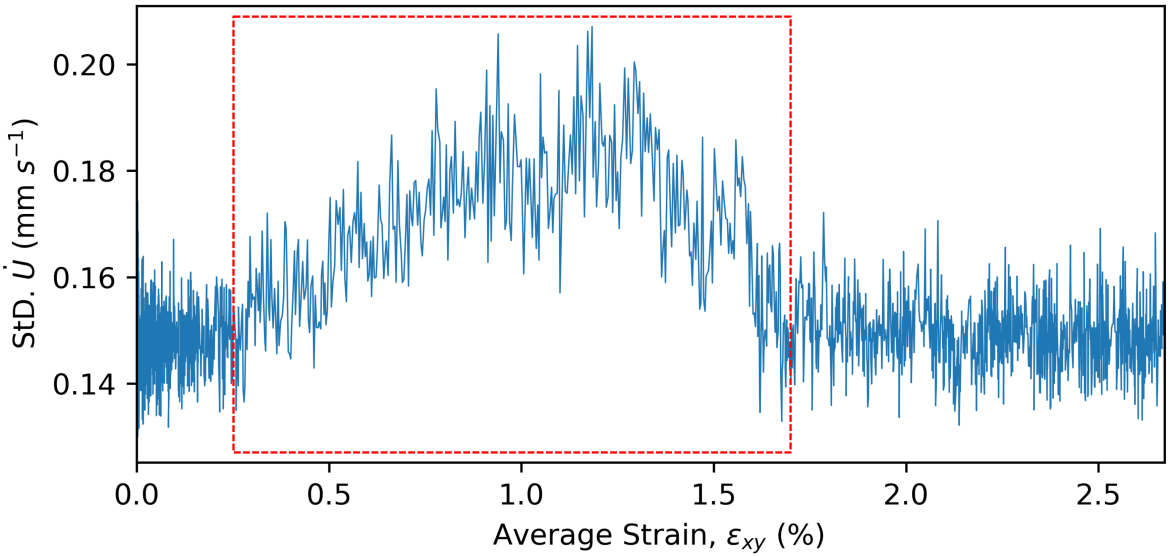

Figure 4.19. Mean strain and STD of nominal velocity field plot of Specimen 4. Velocity field is converted from camera coordinates to specimen coordinates.

The first scalar variable, the STD of nominal velocity field, is plotted in Figure 4.19 against the mean strain. The velocity field is calculated by considering the specimen coordinates instead of the DIC coordinates (image coordinates). Therefore, velocity field denotes the time derivative of displacement field along the RD of the specimen (Figure 3.5). Time derivative of displacement field is taken via forward difference method with step size of $\Delta t = 1$ ms. The velocity field units are converted from pixel per second to mm per second via multiplying the field by the spatial resolution (16.2 μm per pixel). The velocity plot shows similar behavior with Specimen 3 (Section 4.3) where the plot do not touch to the baseline.

The second and third scalar variables, namely mean and STD of strain-rate field, are calculated by utilizing central difference method with $\Delta t = 1$ ms step size. Mean and STD of strain fields are plotted against the average strain in Figure 4.20. STD and mean plots of strain-rate display analogous behavior with Specimen 3 results (Section 4.3). The plot is elevated from the baseline and twin activity continuously happens. After 1.62% average strain, STD plot stays at baseline, making no high amplitude jumps. However, mean strain plot continues to show deformation activity, indicating

that the deformation continues with homogeneous profile than the boxed region. In Figure 4.18d-f, monolithic band fills the region at around 1.7% strain-rate and the strain of the field increases partially homogeneously (Figure 4.18d-e).

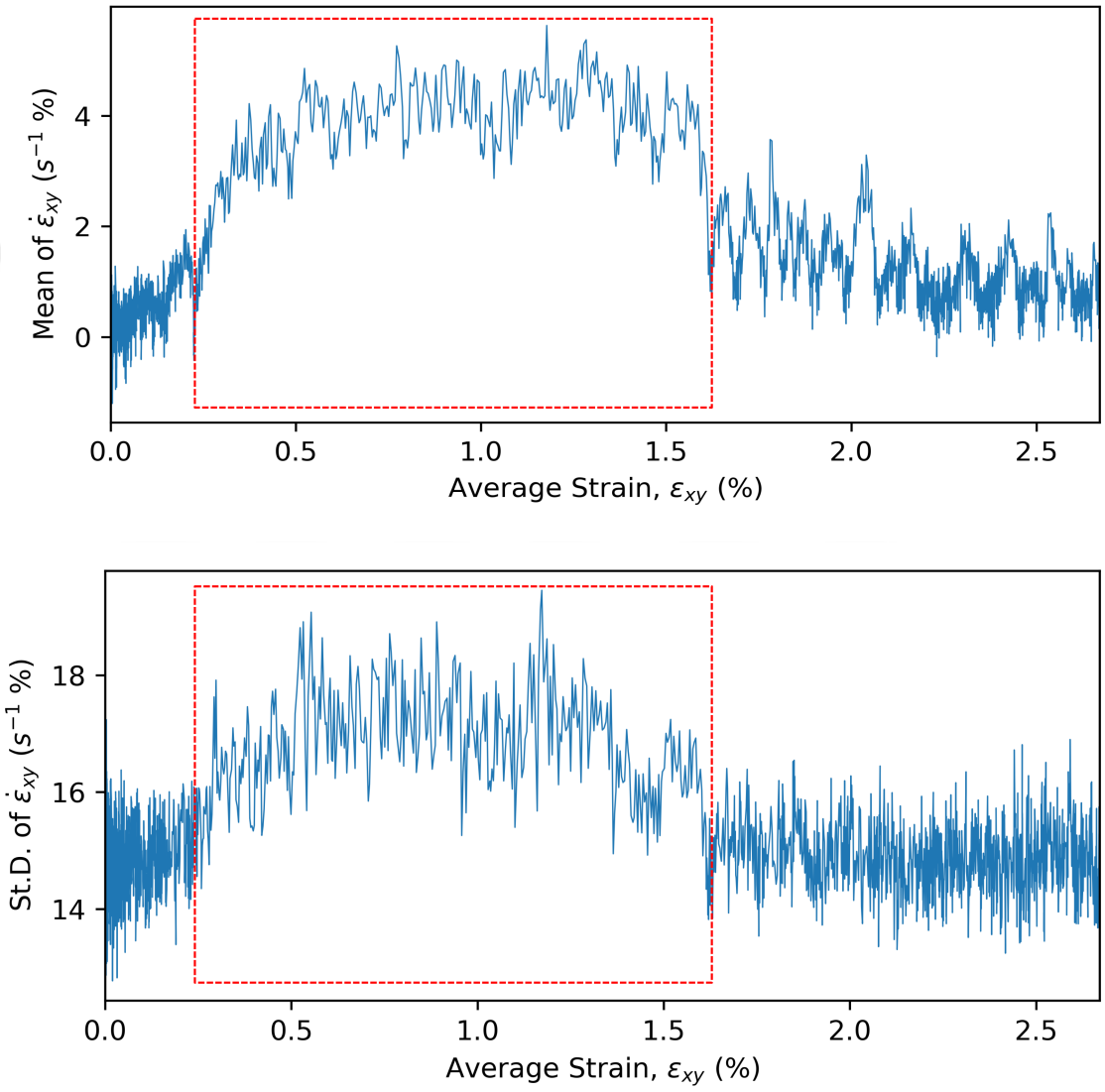

Figure 4.20. Mean and STDs of strain-rate field versus average of strain field plots for Specimen 4. strain-rate is calculated by utilizing central difference.

The fourth scalar variable, median maximum, values are plotted against the average strains in Figure 4.21. The peaks of the median maximum plot has higher amplitude and deviates more than the ones presented in median maximum plot of Specimen 3 (Figure 4.15). Median maximum plot denotes the approximate shear rate

strain if a band present (the plot elevates from the baseline). Figure 4.21 plot indicate that the CTBs are always expanding in the red dashed-box region because there is always a present strain-rate band reading (plot never descends to the baseline). Unlike Specimen 3 (Figure 4.15, there are not any explosive (high amplitude) events present where the band strain is not significantly deviated from the average.

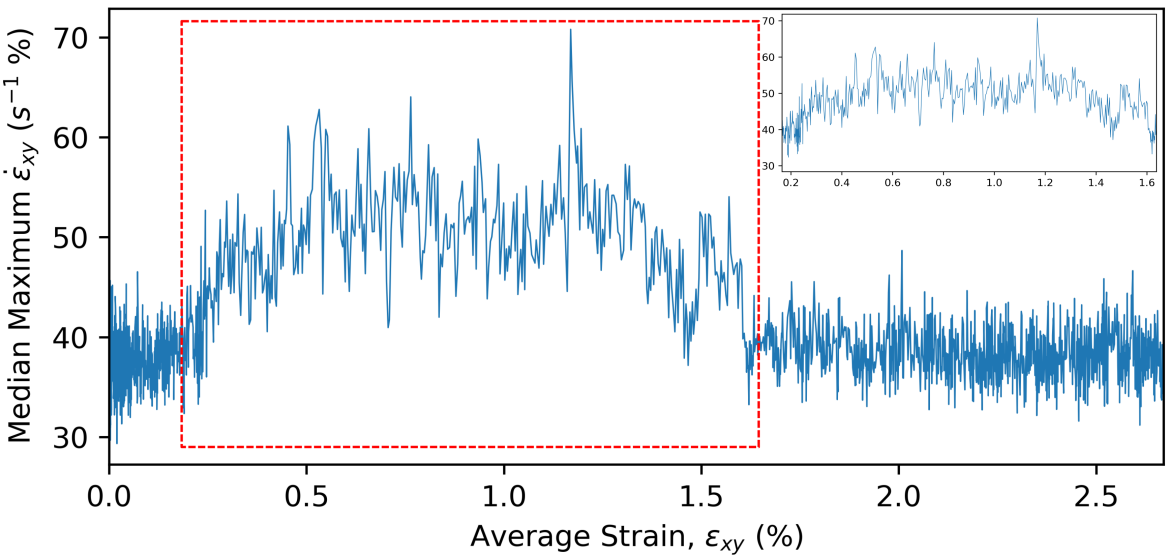

Figure 4.21. Median value of maximum 1% of the strain-rate (median maximum) field versus mean strain for Specimen 4.

One arbitrary point on the Figure 4.21 is selected for further investigation. Deformation history of the CTB event at $\varepsilon_{xy,mean} = 0.93\%$ is shown in Figure 4.22. Figure 4.22a represents the overall strain field change with the event where the edge of the associated CTB is indicated with arrow. The CTB expands towards the bottom of ROI. Overall change of mean strain is 0.03%. Figures 4.22b-f shows the sequential field changes of nominal velocity (left) and forward difference strain-rate (right). At velocity plots of Figure 4.22b-f, the velocity field is continuously separated and separating CTB activities are shown in the strain-rate maps as well. CTB events occur continuously where there is not a point that has velocity field with no separation or strain-rate with no bands present. Due to continuous CTB activity, we can not assess and correlate the CTB events with number of images that captured them individually. With that being

said, we can find the average strain-rate of these continuous expansion bands for the monolithic CTB which is measured as $\dot{\varepsilon}_{xy} = 81.78\%\ s^{-1}$.

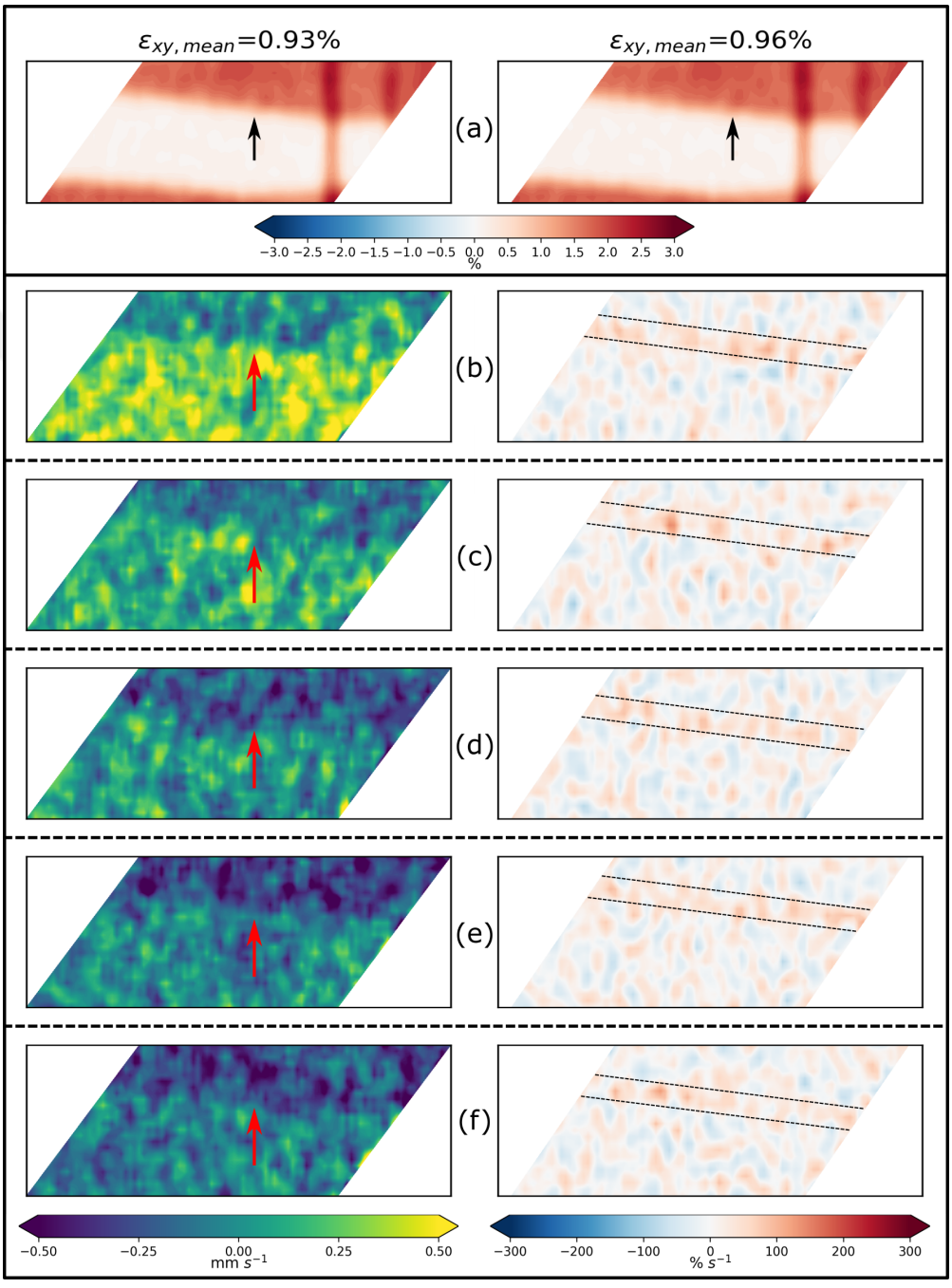

Figure 4.22. Sequential history of the CTB event at $\varepsilon_{xy,mean} = 0.93\%$ on Specimen 4. (a) Initial-final strain fields of the event. (b-f) Sequential history, nominal velocity field at left-hand side and forward difference strain-rate field at right-hand side.

4.5. Full-Field Analysis of Extruded Specimen 5 Under 0.001 strain-rate

The fifth experiment is conducted on Specimen 5 (Figure 3.3) with low strain-rate compression ($\dot{\varepsilon} = -0.001\ s^{-1}$). Before actual loading, pre-load of 150 N is given. The loading is position-controlled and implemented displacement rate is 0.9 mm/min. Full-field analysis figures are resolved at 800 pixels in width and 400 pixels in height. The camera could go up to 774 Hz of acquisition frequency with the implemented resolution. 47159 images are taken with the maximum frequency (774 Hz) while the specimen is loaded during the experiment. All images are analysed with respect to the initially taken reference image via DIC. Load data is obtained from the load cell and mean strain data is calculated for each image with DIC and post-processing. Load data has less sampling (3461) than the DIC mean strain data (47159). Therefore, the load data is upscaled to the size of 47159. Then, the engineering stress data is obtained by dividing the load data to the narrowest cross-sectional area of 36 mm^2. The stress-strain curve constructed from these data is shown in Figure 4.23.

Yielding starts at approximately 106 MPa, initiated with a CTB attack between the diagonal corners of opposite notches shown in Figure 4.23a. There is a stress relaxation observable around points a-b due to initial twinning activity. Twin strains are not as compact as rolled specimens (Specimens 1-4) as expected. Average twin band strain is measured via taking the average of the subset strains inside twinned region in Figure 4.23c and characteristic twin band strain is calculated as -1.31% which is considerably lower than rolled specimens.

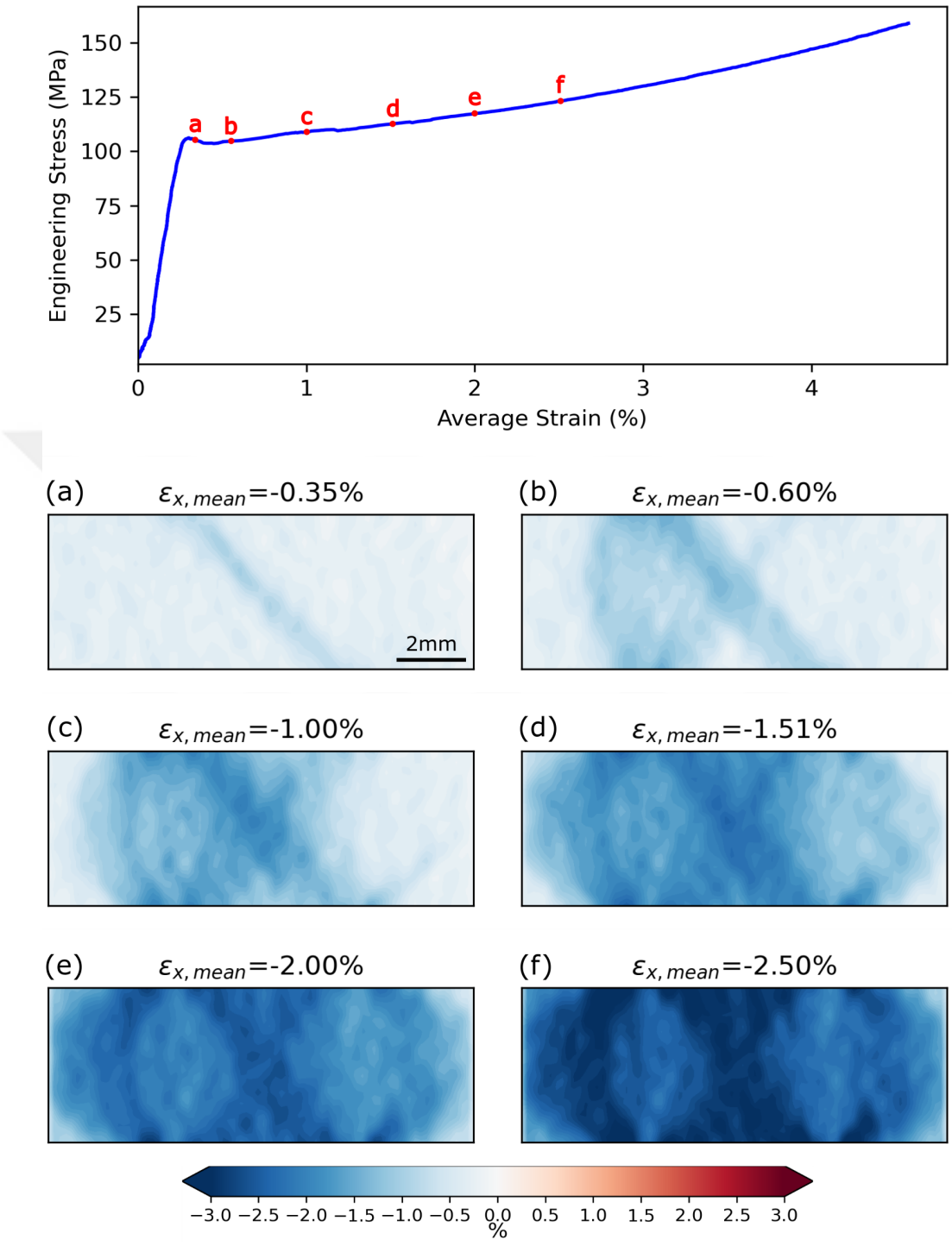

Figure 4.23. Stress-strain plot of Specimen 5. ε_x strain maps (comparable with [28]) are shown on selected points of a, b, c, d, e and f on the curve to display the deformation history.

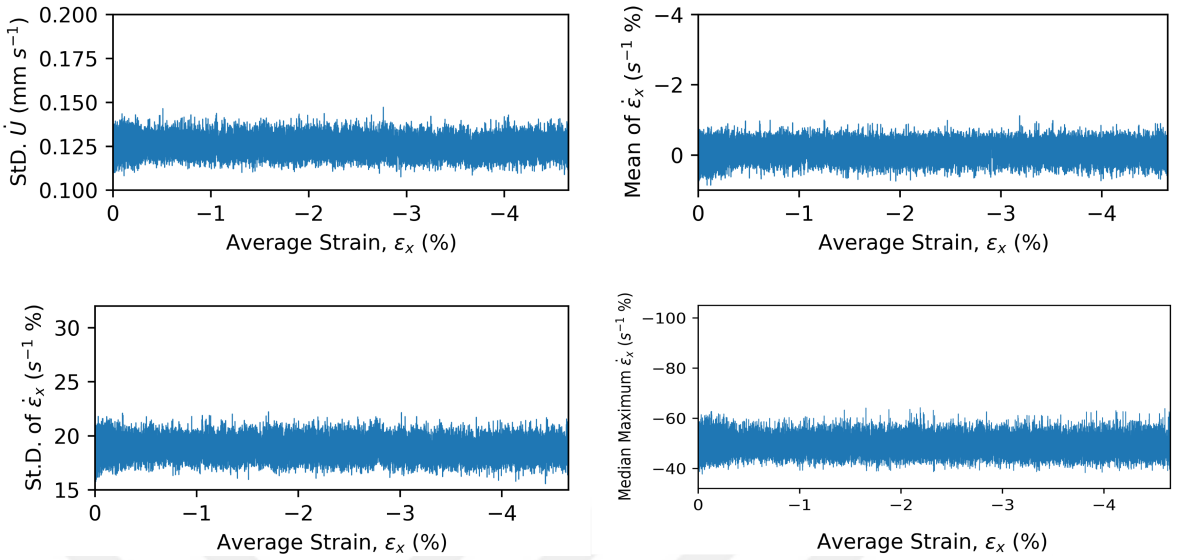

Figure 4.24. Scalar variable plots of Specimen 5, (a) nominal velocity plot, (b) mean of central difference strain-rate plot, (c) STD of central difference strain-rate plot, (d) median maximum plot

Scalar variables of STD($\dot{U}_x(x,y)$), Mean($\dot{\varepsilon}_x(x,y)$), STD($\dot{\varepsilon}_x(x,y)$) and median maximum are plotted against the average strain in Figure 4.24. These plots display no abrupt and localized activity as we see no jumps from the baseline. This indicates that the CTBs are forming and expanding in a diffused manner. Figure 4.24b also shows that the deformation history is not deviated the baseline significantly, indicating that CTB activity accommodate the imposed strains regularly and uniformly.

4.6. Full-Field Analysis of Extruded Specimen 6 Under 0.01 strain-rate

The sixth and last experiment is conducted on Specimen 6 (Figure 3.3) with high strain-rate compression ($\dot{\varepsilon} = -0.01\ s^{-1}$). Before the actual loading, pre-load of 150 N is given. The loading is position-controlled and implemented displacement rate is 8.91 mm/min. Full-field analysis figures are resolved at 800 pixels in width and 400 pixels in height. The camera could go up to 774 Hz of acquisition frequency with the implemented resolution. 5417 images are taken with the maximum frequency (774 Hz) while the specimen is loaded. All images are analysed with respect to the initially

taken reference image via DIC. Load data is obtained from the load cell and mean strain data is calculated for each image with DIC and post-processing. The load data has less sampling (657) than the DIC mean strain data (5417). Therefore, the load data is upscaled to the size of 5417. Then, engineering stress data is obtained by dividing the load data to the narrowest cross-sectional area of 36 mm^2.

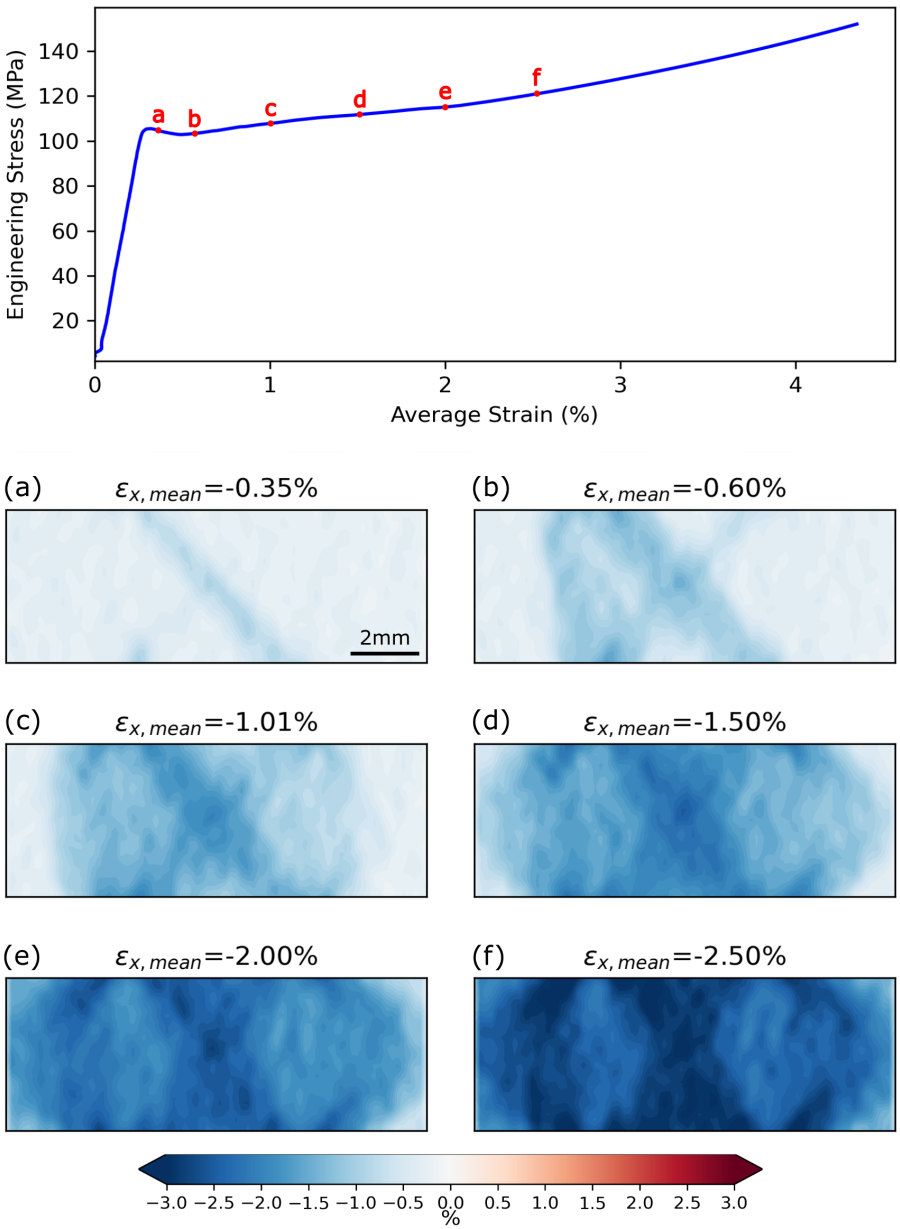

Figure 4.25. Stress-strain plot of Specimen 6. ε_x strain maps (comparable with [28]) are shown on selected points of a, b, c, d, e and f on the curve to display the deformation history.

The stress-strain curve that constructed from engineering stress and average strain data is shown in Figure 4.25. Yielding starts at approximately 107 MPa, initiated with a CTB attack between the diagonal corners of opposite notches shown in Figure 4.25a. There is a stress relaxation observable around points a-b due to initial twinning activity. Twin strains are not as compact as rolled specimens (Specimens 1-4) as expected. Average twin band strain is measured via taking the average of the subset strains inside CTB region in Figure 4.25c and characteristic twin band strain is calculated as -1.36% which is approximately same with Specimen 5 and considerably lower than rolled specimens.

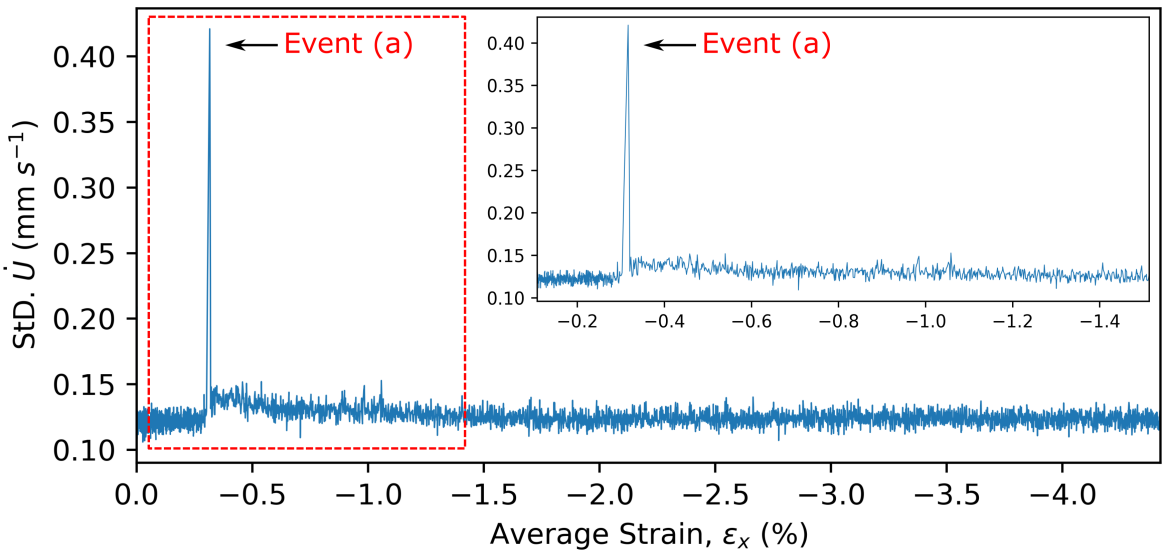

Figure 4.26. Mean strain and STD of nominal velocity field plot of Specimen 6.

The STD of the nominal velocities is the first scalar investigated. STDs of nominal velocity fields [STD($\dot{U}_x(x, y)$)] are plotted versus average value of strain fields in Figure 4.26. The behavior of nominal-velocity plot is different for especially at initial yielding region (around point a at Figure 4.25). Significantly high velocity deviation is observed due to first CTB activities. The rest of the deformation history show baseline elevation compared with the elastic region.

Another two scalar variables derived from the central difference strain-rate fields. Mean($\dot{\varepsilon}_x(x,y)$) and STD($\dot{\varepsilon}_x(x,y)$) values are plotted against the average strains in Figure 4.25. The same signal jump seen in the nominal-velocity field is also present in strain-rate plots as well. Mean($\dot{\varepsilon}_x(x,y)$) plot displays elevated baseline compared with the Mean($\dot{\varepsilon}_x(x,y)$) of Specimen 5 (Figure 4.24 due to the increase in order of the strain-rate of applied loading. Similar behavior is not observed in STD($\dot{\varepsilon}_x(x,y)$) plot where there are not significant deviations within the strain field excluding the jump at the start of the yielding. Elevated baseline of Mean($\dot{\varepsilon}_x(x,y)$) plot but no-jump of STD($\dot{\varepsilon}_x(x,y)$) at plastic region indicates that the deformation is close to be uniform and makes no deviation within the field.

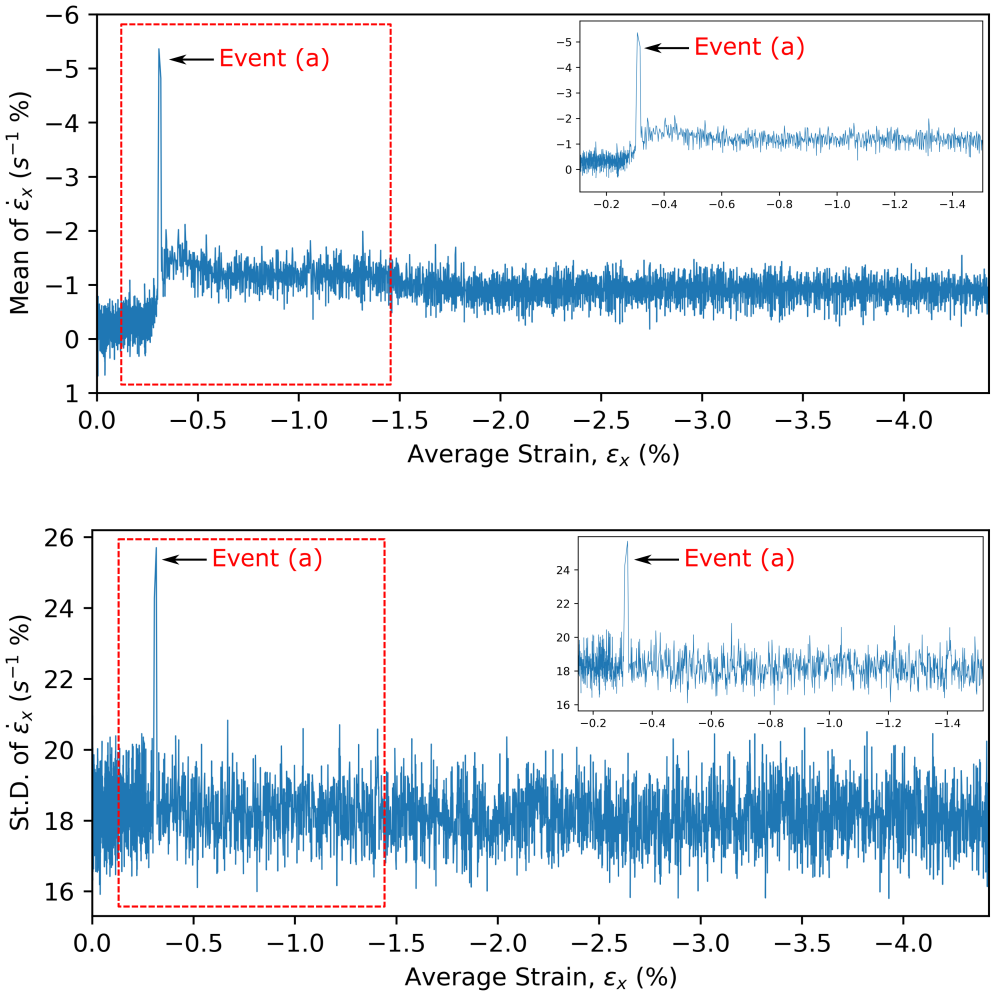

Figure 4.27. Mean and STDs of strain-rate field versus average of strain field plots for Specimen 6. strain-rate is calculated by utilizing central difference.

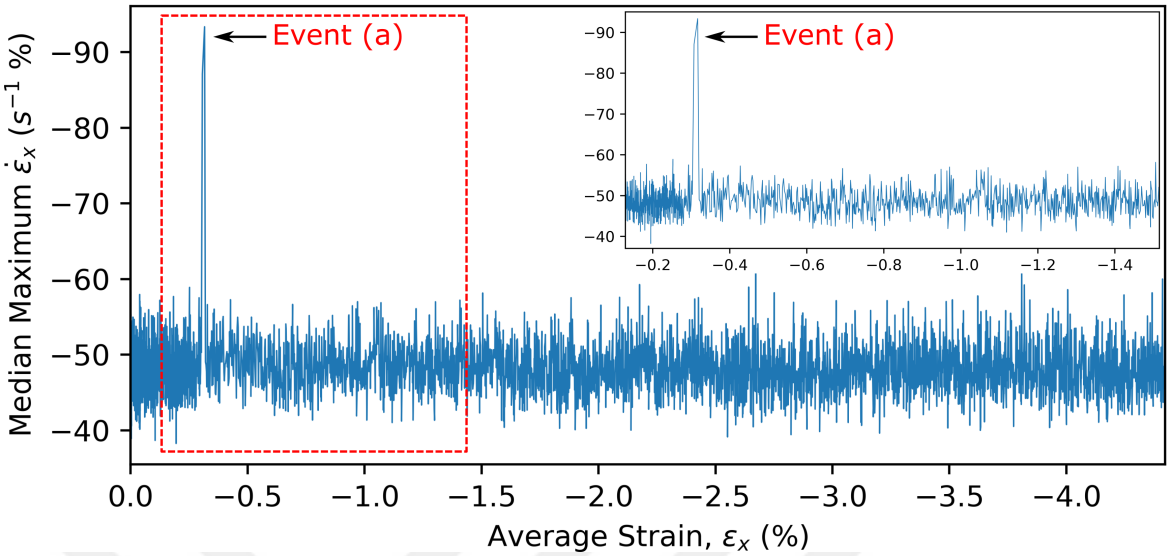

Figure 4.28. Median value of maximum 1% of the strain-rate (median maximum) field versus mean strain for Specimen 6.

The fourth scalar variable, median maximum, is plotted against the average strain is Figure 4.28. The characteristic shape of the plot resembles the STD($\dot{\varepsilon}_x(x, y)$) plot in the Figure 4.27. Only one twin activity is identifiable which is the initial burst strain attack observed at the point a on the stress-strain curve (Figure 4.25). There are some minimal jumps at slip region (after 2.5% average strain) but the peak of those are considerably minimal and fails to stay above our threshold value (Mean(Median Maximum) $\pm$ 2$\times$STD(Median Maximum)) which is applied for previous experiments.

The highest peak in Figure 4.28 (Event a), is selected for further investigation. Deformation history of the CTB event at $\varepsilon_{x,mean} = -1.01\%$ (Event a, which is related with the band at Figure 4.25)a is shown in Figure 4.29. Figure 4.29a represents the overall strain field change with the event where the associated CTB is indicated with an arrow. This is a CTB initiation event because the band is not present at the initial strain field. Overall change of mean strain is 0.02%. Figures 4.5b-f shows the sequential field changes of nominal velocity (left) and forward difference strain-rate (right). Figures 4.29c-e are the points where the CTB initiation happens. In Figures 4.29c-e, the velocity field separation and strain-rate bands are pointed with

arrows. The Figure 4.29c is the start point of the event where the band formation starts to show. The main event takes place at Figure 4.29d, where the velocity fields are visibly separated by the CTB region (high displacement gradients are present) and the strain-rate forms a clear band with median maximum of $\dot{\varepsilon}_{x,band} = -118\%\ s^{-1}$. The Figure 4.29e is the end point where both velocity and strain-rate signals diminish. This particular event is captured within three consecutive images.

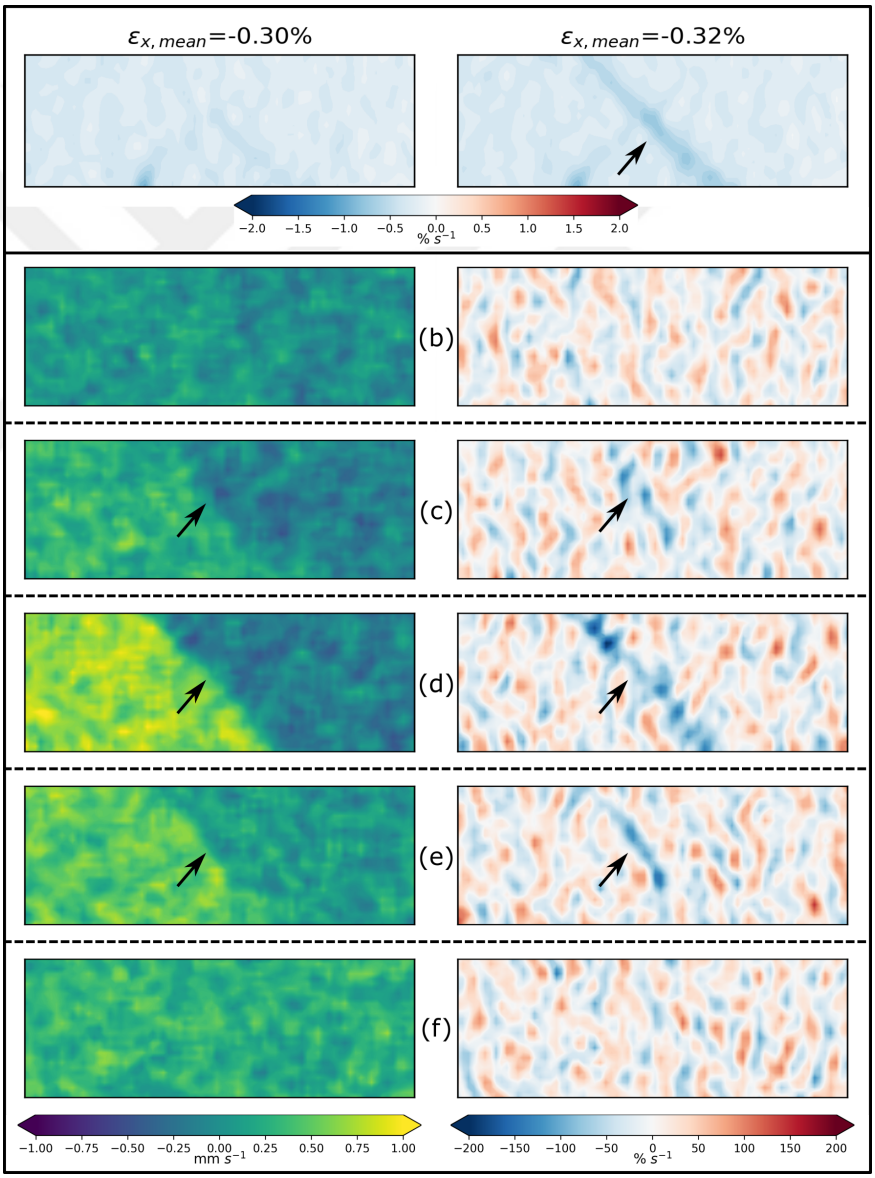

Figure 4.29. Sequential history of the CTB event at $\varepsilon_{x,mean} = -0.30\%$ on Specimen 6. (a) Initial-final strain fields of the event. (b-f) Sequential history, nominal velocity field at left-hand side and forward difference strain-rate field at right-hand side.

5. DISCUSSION

5.1. Review on Numerical Methodologies

Quality of DIC results depends on factors such as the uniqueness of the DIC pattern (fine and non repetitive distribution of speckle), lightning uniformity (equal illumination for the images) and stability of the images (vibration-free region of interest). The initial efforts described in the Sections 3.1, 3.2 and 3.4 tried to eliminate the error sources completely. However, there are trade-offs for some of these optimizations. For example, using a larger subset size reduce the error by increasing the uniqueness of each subset but reduces the magnitude of output data due to wider interpolation.

The DIC error is considerably small for large deformation signals where we do not see any noise on the strain maps given in stress-strain plots in Figures 4.1, 4.7, 4.12, 4.18, 4.23 and 4.25. On the other hand, DIC error is relatively influential for sequential data (nominal velocity and strain-rate) where the deformation signal is considerably low due to high acquisition frequency and very small deformations between small time intervals. This margin is observable at nominal velocity and strain-rate plots given in sequential history of selected events in Figures 4.5, 4.6, 4.11, 4.16, 4.17, 4.22 and 4.29.

The baseline error amplitudes (thickness of baseline) of Mean($\dot{\varepsilon}(x, y)$) plots for high strain-rate experiments (0.01 s^{-1}) are a smaller fraction of their low strain-rate counterpart experiments (0.001 s^{-1}). For example, Specimen 1 and 3 are same specimens but different strain-rates are applied to them and Figure 4.3 central difference Mean($\dot{\varepsilon}(x, y)$) plot show wider baseline fluctuation (approximately 0.35% s^{-1}) than Figure 4.14 Mean($\dot{\varepsilon}(x, y)$) plot (approximately 0.20% s^{-1}) at elastic region. Same phenomenon is present between Specimens 2-4 and 5-6 as well. Reason of this is DIC errors become less influential on the results as the deformation signal between the sequential images increases and this signal is proportional with the strain-rate of the experiment.

5.2. Effect of strain-rate on Deformation

Low (0.001% s^{-1}) and high (0.01% s^{-1}) strain-rate loading resulted in a different deformation plasticity behavior on rolled specimens. When we inspect the stress strain curves of Specimen 1 (Figure 4.1) and Specimen 3 (Figure 4.12), the expansion of the monolithic band of Specimen 3 displays perfect plastic deformation as there is no increase in stress is observed until 1.58% average strain. At that point, secondary CTB formations starts and crosses-over the monolithic CTB and specimen starts to show hardening. However, monolithic CTB of Specimen 1 expands with some degree of hardening between points a and c of Figure 4.1 as approximately 6 MPa increase in stress is observed until the secondary CTB formation at point c. The reason for this different hardening response may be the distinct behaviors of twin and hard-slip (non-basal) systems against the implemented strain-rates.

In mechanics, temperature and strain-rate dependence are typically associated. Tensile twin is known as an athermal mechanism (its activity is not affected by temperature or strain-rate) whereas hard-slip mechanisms show much higher temperature or strain-rate dependence [46–48]. While temperature encourages operation of a "thermal" mechanism (a mechanism whose intrinsic time of operation is affected by temperature), higher strain-rates discourages the same mechanism by given it less time. If the implemented strains are abrupt, complementary hard-slip activities stays behind of the extension twin activity. This results in increased twin but reduced slip activity. Since dislocation slip activity is diminished and twinning itself causes negligible hardening, work hardening of the material decreases.

Similar hardening behavior difference is observed between Specimens 2 and 4 (mild notched rolled specimens) in Figures 4.7 and 4.18 stress-strain curves as well. Specimen 2 stress level is increased by 4 MPa until 0.75% nominal strain while Specimen 4 stress level is increased by 2 MPa until 0.74% nominal strain. A minor difference between Specimens 3 and 4 is they are went through high strain-rate experiments but Specimen 4 shows small hardening (2 MPa stress increase) until 0.74% average strain

while Specimen 3 is nearly perfect plastic (1 MPa stress increase until 1.58% average strain). We can not assess the deformation profiles of the whole material field that alter the stress-strain curves for Specimens 2 and 4 because camera ROI focuses on the notched area.

All full-field analysis experiments (Specimens 1, 3, 5 and 6) indicate that CTB nucleation (original formation of the band) results in much higher strain-rate response compared with the CTB expansion. The CTB activities presented in Figures 4.5, 4.6, 4.16 and 4.29 are CTB nucleation events that associated with the highest peaks of their respective median maximum plots. In addition, these experiments show that the first CTB activities are explosive (resulting in significantly high strain-rate band) for high strain-rate loading (Specimen 3 and 6). Respective median maximum plots in Figures 4.15 and 4.28 show that the initial CTB activities yield significantly higher strain-rate than the latter CTB activities for Specimen 3 and 6. On the other hand, Specimen 1 display highest strain-rate bands with secondary CTB nucleations and extruded Specimen 5 does not respond with any CTB strain-rate band within the detectable range.

CTB activities are impulse-like functions (CTB activity starts, ends and stays idle for a period) in band strain-rate Figures 4.4 and 4.10 for low strain-rate loading experiments (Specimens 1 and 2). Selected event analysis figures (4.5, 4.6, 4.11 show these periods as the start and finish of these events can be seen at the first and the last nominal-velocity and strain-rate fields (no separation of velocity field and band formation within the strain-rate field). However, CTB activities become rather continuous with each other for high strain-rate experiments which can be seen at median maximum plots of these experiments (Figures 4.15, 4.21). Possibly, these events are still periodic events. If CTB events are periodic, the separation periods between individual CTBs could not be captured with maximum of 998 Hz acquisition frequency (these events occur within much less than 1 ms which is time interval between the images with 998 Hz acquisition) for implemented strain-rate of 0.01% s^{-1}. On the other hand, CTBs may expand continuously (non-periodic) without slip hindrance due to

the strain-rate dependence of hard-slip mechanisms. For both cases, it can be argued that the maximum instantaneous speed of the CTB activities are inversely related with the implemented strain-rate and results in either much smaller or non-existent periods between each other.

5.3. Effect of Material Texture on Deformation

The extruded specimens (Specimens 5 and 6) show rather distributed strain distribution of CTBs (Figures 4.23 and 4.25) compared to the sharp formations observed in rolled specimens (Figures 4.1, 4.7, 4.12 and 4.18). This is the result of texture differences between the rolled and extruded Magnesium (Section 2.3. Average strains within the twinned region (around -1.40%) of extruded specimens is lower than their rolled counterparts (around -2.0%).

Strain maps of extruded specimens show that the initial twin activity forms a band across the diagonal corners of the notches. This is intended to localize the strain distribution as we know that extruded Magnesium deforms homogeneous via twinning. Despite the localization efforts Specimen 5 (0.001% s^{-1} compression) show no local twin activity from our 4-parameter plots in Figure 4.24. Specimen 6 (0.001% s^{-1} compression) show similar behavior at overall plasticity region but initial yielding. There is a significant peak recorded in all 4-parameter plots (Figures 4.26, 4.27 and 4.28) which is related with initial CTB band formation. This event is rather unique for this specimen because there is no other bands could be recorded. The band strain-rate recorded with this particular event ($\dot{\varepsilon}_{x,band} = -118\%\ s^{-1}$) is comparable with the one observed at Specimen 3 in Figure 4.16 ($\dot{\varepsilon}_{x,band} = -136\%\ s^{-1}$) that both band strain-rates are nearly same for different textures but same implemented strain-rates.

5.4. Assessment on CTB Event Duration

When one can see the start and end of and activity within sequential images (as the cases in Figures 4.5, 4.6 and 4.11), approximate duration for these events can be

calculated. Therefore, the events need to be periodic like in the low strain-rate loading experiments on rolled Specimens 1 and 2 to assess a time for the duration of these events. Such periodic band strain-rate is observed within both Specimens 1 and 2 in Figures 4.4 and 4.10.

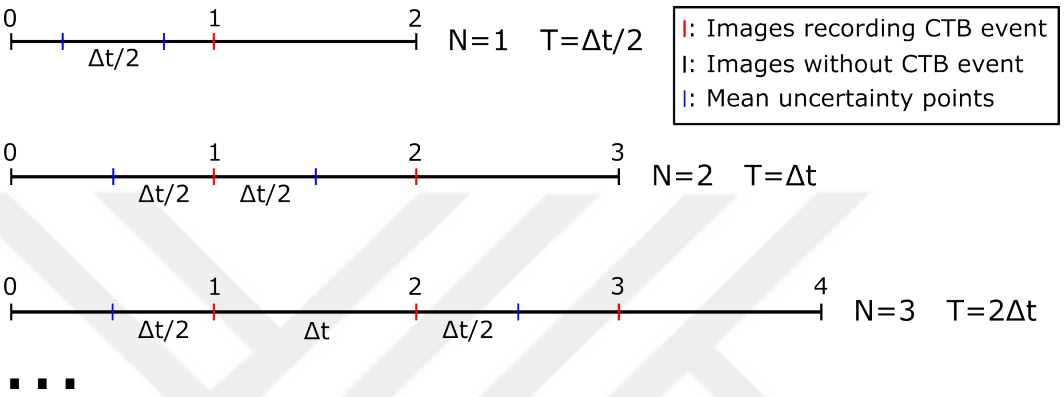

Figure 5.1. Illustration of approximate event duration for CTB activities. N is the number of consecutive images that recorded a particular CTB activity, Δt is the period between the images and T is the total nominal event duration for that particular CTB activity.

The time-difference of strain results gives the strain changes between the time interval between sequential images (Δt). If a CTB even is observed within one strain-rate image (deformation signal is observed within a particular image, and no signal is observed at neighboring images), this event started and ended within less than one time interval ($t_{CTB} < \Delta t$) with Δt uncertainty. For another case, if a CTB event is observed within two consecutive strain-rate images, this event started and ended within less than two time intervals ($t_{CTB} < 2\Delta t$) with $2\Delta t$ uncertainty. This changes with three or more consecutive images capturing an individual CTB activity where at least one image interval enters certainty region. For a CTB activity with three consecutive images, we are certain that this activity covered entire time zone between the first and second event images (Δt certainty) with $2\Delta t$ uncertainty due to the first and last images. In Figure 5.1, event duration measurement is shown for one, two and three

images CTB events. To deal with uncertainties, we took the average of the uncertainty time interval and make an approximate calculation of event duration.

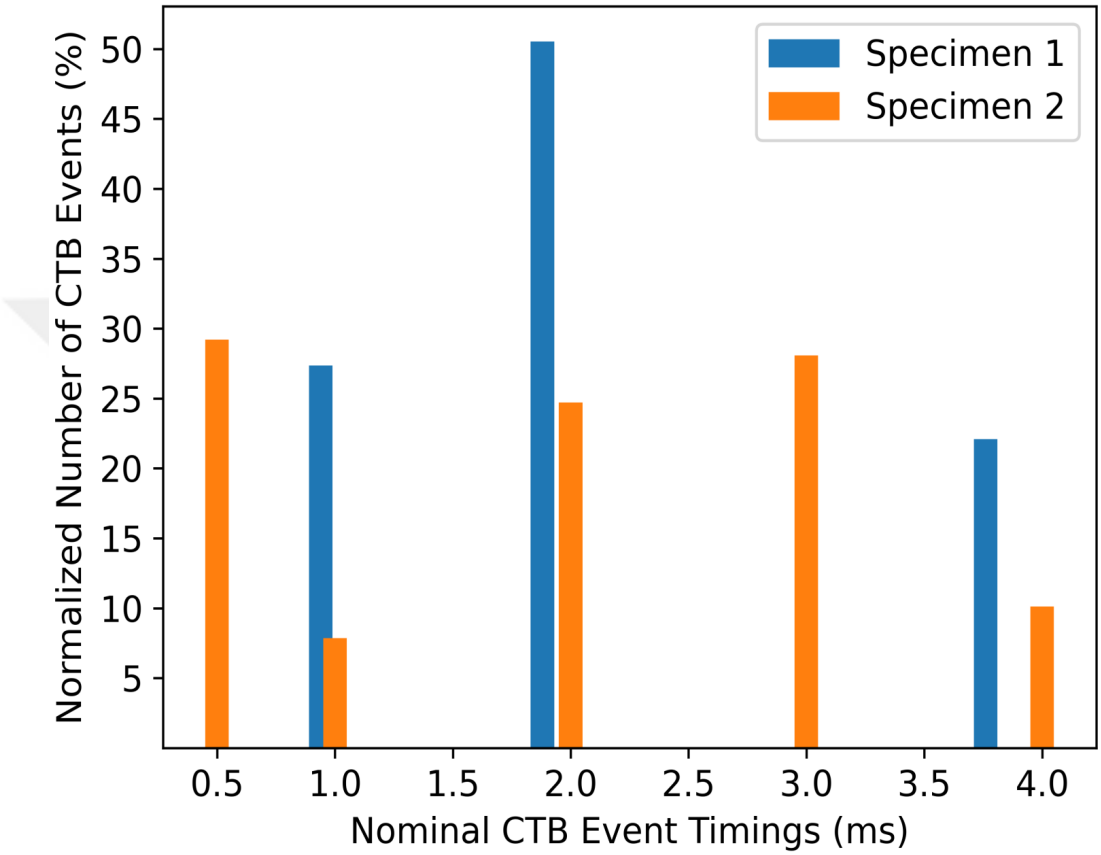

Figure 5.2. Histogram of nominal CTB event duration and normalized number of events observed.

Returning to Tables 4.1 and 4.2, we can apply the approximation shown in Figure 5.1 to create nominal event duration for Specimens 1 and 2. The distribution of nominal CTB event duration and normalized number of CTB events (overall percentage with respect to the all events observed) that corresponds to those duration are shown in Figure 5.2. From this figure, we can see that the nominal duration are within a specific range (events on both Specimens 1 and 2 are within similar duration range). From Tables 4.1 and 4.2, number of images that captured CTB events are higher for Specimen 2 due to higher acquisition frequency (998 Hz versus 532 Hz). However, these events corresponds to same nominal duration. When we calculate the average nominal event

duration for each specimen, average time for Specimen 1 is 2.04 ms and for Specimen 2 is 1.97 ms. These two values are approximately same which is logical because Specimen 1 and 2 are same materials (cut from same plate) and loading parameters of their respective experiments are same. This result also shows that 532-998 Hz (Δt= 1.00-1.88 ms) is sufficient to observe the story of CTB activities within multiple images.

6. CONCLUSION

In this study, CTB deformation mechanics and dynamics on polycrystalline Magnesium AZ31 specimens are analyzed with temporal resolution. The effects crystallographic texture on CTB deformation is inspected by using hot-rolled and hot-extruded specimens. These specimens are subjected to strain-rates of 0.001 s^{-1} and 0.01 s^{-1} to evaluate the effects of strain-rate on CTB deformation. To increase the recording frequency, specifically shaped specimens with notches are used to direct the CTB deformation plateau to a regional area. ROI of the camera focused on this smaller regional area, resulting in approximately doubled recording frequency. Four scalar variables are derived from the deformation fields to characterize and compare them individually which are the STD of nominal velocity field, mean and STD of strain-rate fields, median of the strain-rate field with value of highest 1%.

Strain-rate is an influential parameter that affects the CTB activities on the Magnesium specimens. Specimens loaded with low strain-rate (0.001 s^{-1}) show periodic attacks of CTB activity, each separated by an idle region. On the other hand, high strain-rate (0.01 s^{-1}) loading resulted in continuous CTB activity as continuous strain-rate reading was observed on the twin plateau from high strain-rate experiments. Also, high strain-rate experiments resulted in explosive initial CTB nucleations where the strain-rate readings of these nucleations are much higher than the rest of the twin plateau. In addition, the CTB nucleation is found to cause the strain-rate bands with higher magnitude than the CTB expansion bands.

Crystallographic texture is another factor that has significant effect on the deformation behavior of Magnesium. Extruded specimens are subjected to both low and high strain-rate compression. Low strain-rate loading results indicate no localize CTB takes place within any region of the deformation plateau. Because of the crystallographic texture, CTB bands on Magnesium distributes rather homogeneously and do not cause significant deviations on the deformation map. However, high strain-rate

resulted in an initial CTB activity with band strain-rate comparable to the CTB activities on the rolled specimens. In general, the most explosive events have been associated with CTB nucleation (the original formation of a CTB band).

An effort to assess the duration of CTB activities is carried out on the rolled specimens compressed with low strain-rate. CTB activities on these specimens show periodic behavior where individual CTB attacks are separated from each other by idle region (in idle region no CTB activities are observed). Number of sequential images that captures individual CTB activities are analyzed with considering the uncertainty problem. To deal with the uncertainties, average value of the uncertainty time interval (half of the interval) is taken as approximation. Nominal CTB event duration of both specimens are distributed within the similar interval on the time axis. In addition, the average value of CTB event duration for both specimens are calculated and came out approximately same value which is 2 ms. Average CTB duration results indicates that our recording frequencies are sufficient to capture the story of individual CTB events on specimens under low strain-rate compression because time interval between sequential images are lower than the average CTB event duration (1 and 1.88 ms for 998 and 532 Hz respectively).

7. FUTURE WORK

The strain-rate definitely plays a crucial role on CTB deformation. Just an order increase of applied strain-rate altered the CTB behavior significantly as we discovered different hardening characteristics and periodic CTB activity. Similar experiments can be carried out with strain-rates in orders of 10^{-4} s^{-1}. With same image acquisition setup (acquisition frequencies between 500 and 1000 Hz), lower strain-rate may lead us to capture individual CTB events with higher number of sequential images.

This study have shown that the CTB activities on rolled MgAZ31 under 0.001 s^{-1} are barely observable within the acquisition frequencies within the range of 500-1000 Hz. Increasing the acquisition frequency with better cameras is expected to improve the CTB event duration assessment because more sequential images would be captured for individual CTB activities and hence, the effect of uncertainty would decrease. Moreover, we could not determine whether the DIC activity of the high strain-rate rolled experiments are periodic or continuous with our image acquisition frequency. Using cameras with higher frequency would answer this question. This effort also demands more robust DIC and post-processing algorithms to reduce the DIC error further because the influence of DIC error increases with lower deformation signal between sequential images. The deformation signal would certainly decrease with higher acquisition frequencies (lower Δt).

REFERENCES

1. Versnyder, F. I. and M. Shank, "The Development of Columnar Grain and Single Crystal High Temperature Materials Through Directional Solidification", *Materials Science and Engineering*, Vol. 6, pp. 213–247, 1970.

2. Choi, I., S. Jin and S. Kang, "Effects of Microstructure and Alloy Contents on the Lüders Line Formation in Al-Mg Alloys", *Scripta Materialia*, Vol. 38, No. 6, pp. 887–892, 1998.

3. de Codes, R. N., O. S. Hopperstad, O. Engler, O. G. Lademo, J. D. Embury and A. Benallal, "Spatial and Temporal Characteristics of Propagating Deformation Bands in AA5182 Alloy at Room Temperature", *Metallurgical and Materials Transactions A*, Vol. 42, pp. 3358–3369, 2011.

4. Nagarajan, S., R. Narayanaswamy and V. Balasubramaniam, "An Insight into Lüders Deformation Using Advanced Imaging Techniques", *Journal of Materials Engineering and Performance*, Vol. 22, pp. 3085–3092, 2013.

5. Ananthakrishna, G., "Current Theoretical Approaches to Collective Behavior of Dislocations", *Physics Reports*, Vol. 440, pp. 113–259, 2007.

6. Schwab, R. and V. Ruff, "On the Nature of the Yield Point Phenomenon", *Acta Materialia*, Vol. 61, pp. 1798–1808, 2013.

7. Cai, Y. L., S. L. Yang, S. H. Fu and Q. C. Zhang, "The Influence of Specimen Thickness on the Lüders Effect of a 5456 Al-Based Alloy: Experimental Observations", *Metals*, Vol. 6, No. 120, pp. 1–12, 2016.

8. Efstathiou, C. and H. Sehitoglu, "Strain Hardening and Heterogeneous Deformation During Twinning in Hadfield Steel", *Acta Materialia*, Vol. 58, No. 5, pp. 1479–1488, 2010.

9. Aydıner, C. C. and M. A. Telemez, "Multiscale Deformation Heterogeneity in Twinning Magnesium Investigated with In Situ Image Correlation", *International Journal of Plasticity*, Vol. 56, pp. 203–218, 2014.

10. Muránsky, O., M. Barnett, V. Luzin and S. Vogel, "On the Correlation Between Deformation Twinning and Lüders-like Deformation in an Extruded Mg Alloy: In Situ Neutron Diffraction and EPSC.4 Modelling", *Materials Science and Engineering: A*, Vol. 527, pp. 1383–1394, 2010.

11. Jayasathyakawin, S., M. Ravichandran, N. Baskar, C. Anand Chairman and R. Balasundaram, "Mechanical Properties and Applications of Magnesium alloy – Review", *Materials Today: Proceedings*, Vol. 27, pp. 909–913, 2020.

12. Easton, M., A. Beer, M. Barnett, C. Davies, G. Dunlop, Y. Durandet, S. Blacket, T. Hilditch and P. Beggs, "Magnesium Alloy Applications in Automative Structures", *Jom*, Vol. 60, pp. 57–62, 2008.

13. Lou, X. Y., M. Li, R. K. Boger, S. R. Agnew and R. H. Wagoner, "Hardening Evolution of AZ31B Mg Sheet", *International Journal of Plasticity*, Vol. 23, pp. 44–86, 2007.

14. Barnett, M. R., M. D. Nave and A. Ghaderi, "Yield Point Elongation Due to Twinning in a Magnesium Alloy", *Acta Materialia*, Vol. 60, pp. 1433–1443, 2012.

15. Anten, K. and B. Scholtes, "Formation of Macroscopic Twin Bands and Inhomogeneous Deformation During Cyclic Tension-Compression Loading of the Mg-Wrought Alloy AZ31", *Materials Science and Engineering: A*, Vol. 746, pp. 217–228, 2019.

16. Shafaghi, N., E. Kapan and C. C. Aydıner, "Cyclic Strain Heterogeneity and Damage Formation in Rolled Magnesium via In Situ Microscopic Image Correlation", *Experimental Mechanics*, Vol. 60, pp. 735–751, 2020.

17. Hull, D. and D. J. Bacon, *Introduction to Dislocations*, 5th edn., Elsevier, Oxford, 2011.

18. Agnew, S. R., D. W. Brown and C. Tomé, "Validating a Polycrystal Model for the Elastoplastic Response of Magnesium Alloy AZ31 Using In Situ Neutron Diffraction", *Acta Materialia*, Vol. 54, pp. 4841–4852, 2006.

19. Yoo, M. H., "Slip, Twinning, and Fracture in Hexagonal Close-Packed Metals", *Metallurgical Transactions A*, Vol. 12, pp. 409–418, 1981.

20. Üçel, I. B., E. Kapan, O. Türkoğlu and C. C. Aydıner, "In Situ Investigation of Strain Heterogeneity and Microstructural Shear Bands in Rolled Magnesium AZ31", *International Journal of Plasticity*, Vol. 118, pp. 233–251, 2019.

21. Hosford, W. F., *Mechanical Behavior of Materials*, 2nd edn., Cambridge University Press, Cambridge, 2009.

22. Nie, J. F., K. S. Shin and Z. R. Zeng, "Microstructure, Deformation, and Property of Wrought Magnesium Alloys", *Metallurgical and Materials Transactions A*, Vol. 51, pp. 6045–6109, 2020.

23. Kapan, E., N. Shafaghi, S. Uçar and C. C. Aydıner, "Texture-Dependent Character of Strain Heterogeneity in Magnesium AZ31 Under Reversed Loading", *Materials Science and Engineering: A*, Vol. 684, pp. 706–711, 2017.

24. Kannan, V., X. Ma, N. M. Krywopusk, L. J. Kecskes, T. P. Weihs and K. T. Ramesh, "The Effect of Strain Rate on the Mechanisms of Plastic Flow and Failure of an ECAE AZ31B Magnesium Alloy", *Journal of Materials Science*, Vol. 54, pp. 13394–13419, 2019.

25. Ulacia, I., S. Yi, M. T. P. Prado, N. Dudamell, F. G. Diaz-Rubio, D. Letzig and I. Hurtado, "Texture Evolution of AZ31 Magnesium Alloy Sheet at High Strain

Rates", *4th International Conference on High Speed Forming*, pp. 189–197, Columbus, Ohio, USA, 2010.

26. Özdür, N. A. and C. C. Aydıner, "Advance of Collaborative Twinning Fields in Magnesium AZ31 via the Strain and Residual Intensity Channels in Microscopic Image Correlation", *Conference Proceedings of the Society for Experimental Mechanics Series*, Vol. 2, pp. 1–9, 2022.

27. Özdür, N. A., I. B. Üçel, J. Yang and C. C. Aydıner, "Residual Intensity as a Morphological Identifier of Twinning Fields in Microscopic Image Correlation", *Experimental Mechanics*, Vol. 61, pp. 499–514, 2021.

28. Erman, S. C., L. Stainier and C. C. Aydıner, "Guiding Severely Anisotropic Twinning Bands in Magnesium: An In Situ Investigation by Full-Field Microscopic Image Correlation", *Materials Today Communications*, Vol. 35, p. 106203, 2023.

29. Drozdenko, D., J. Bohlen, S. Yi, P. Minárik, F. Chmelík and P. Dobroň, "Investigating a Twinning–Detwinning Process in Wrought Mg Alloys by the Acoustic Emission Technique", *Acta Materialia*, Vol. 110, pp. 103–113, 2016.

30. Murasawa, G., R. Takahashi, T. Morimoto and S. Yoneyama, "Inhomogeneous Deformation Twinning Measurement Using Digital Image Correlation and Acoustic Emission", *Experimental Mechanics*, Vol. 55, pp. 65–76, 2015.

31. Kannan, V., K. Hazeli and K. Ramesh, "The Mechanics of Dynamic Twinning in Single Crystal Magnesium", *Journal of the Mechanics and Physics of Solids*, Vol. 120, pp. 154–178, 2018.

32. Hutchinson, J. W., "Elastic-Plastic Behaviour of Polycrystalline Metals and Composites", *Proceedings of the Royal Society of London. A. Mathematical and Physical Sciences*, Vol. 319, pp. 247–272, 1970.

33. Cheng, J., J. Shen, R. K. Mishra and S. Ghosh, "Discrete Twin Evolution in Mg Alloys Using a Novel Crystal Plasticity Finite Element Model", *Acta Materialia*, Vol. 149, pp. 142–153, 2018.

34. Chang, Y. and D. M. Kochmann, "A Variational Constitutive Model for Slip-Twinning Interactions in HCP Metals: Application to Single and Polycrystalline Magnesium", *International Journal of Plasticity*, Vol. 73, pp. 39–61, 2015.

35. Cai, W. and W. D. Nix, *Imperfections in Crystalline Solids*, Cambridge University Press, Cambridge, 2016.

36. Koike, J., "Enhanced Deformation Mechanisms by Anisotropic Plasticity in Polycrystalline Mg Alloys at Room Temperature", *Metallurgical and Materials Transactions A*, Vol. 36, pp. 1689–1696, 2005.

37. Wu, Z., M. F. Francis and W. A. Curtin, "Magnesium Interatomic Potential for Simulating Plasticity and Fracture Phenomena", *Modelling and Simulation in Materials Science and Engineering*, Vol. 23, pp. 1–19, 2015.

38. Christian, J. W. and S. Mahajan, "Deformation Twinning", *Progress in Materials Science*, Vol. 39, pp. 1–157, 1995.

39. Barnett, M., "Twinning and the Ductility of Magnesium Alloys: Part II. "Contraction" Twins", *Materials Science and Engineering: A*, Vol. 464, No. 1, pp. 8–16, 2007.

40. Hama, T., Y. Kariyazaki, N. Hosokawa, H. Fujimoto and H. Takuda, "Work-Hardening Behaviors of Magnesium Alloy Sheet During in-Plane Cyclic Loading", *Materials Science and Engineering: A*, Vol. 551, pp. 209–217, 2012.

41. Wu, L., S. Agnew, D. Brown, G. Stoica, B. Clausen, A. Jain, D. Fielden and P. Liaw, "Internal Stress Relaxation and Load Redistribution During the

Twinning–Detwinning-Dominated Cyclic Deformation of a Wrought Magnesium Alloy, ZK60A", *Acta Materialia*, Vol. 56, pp. 3699–3707, 2008.

42. Prasad, K. E. and K. Ramesh, "In Situ Observations and Quantification of Twin Boundary Mobility in Polycrystalline Magnesium", *Materials Science and Engineering: A*, Vol. 617, pp. 121–126, 2014.

43. Kumar, M. A., I. J. Beyerlein, R. A. Lebensohn and C. N. Tomé, "Modeling the Effect of Neighboring Grains on Twin Growth in HCP Polycrystals", *Modelling and Simulation in Materials Science and Engineering*, Vol. 25, p. 064007, 2017.

44. Pan, B., K. Li and W. Tong, "Fast, Robust and Accurate Digital Image Correlation Calculation Without Redundant Computations", *Experimental Mechanics*, Vol. 53, pp. 1277–1289, 2013.

45. Pan, B., "Full-Field Strain Measurement Using a Two-Dimensional Savitzky-Golay Digital Differentiator in Digital Image Correlation", *Optical Engineering*, Vol. 46, p. 033601, 2007.

46. Hollenweger, Y. and D. M. Kochmann, "An Efficient Temperature-Dependent Crystal Plasticity Framework for Pure Magnesium with Emphasis on the Competition Between Slip and Twinning", *International Journal of Plasticity*, Vol. 159, p. 103448, 2022.

47. Chapuis, A. and J. H. Driver, "Temperature Dependency of Slip and Twinning in Plane sStrain Compressed Magnesium Single Crystals", *Acta Materialia*, Vol. 59, pp. 1986–1994, 2011.

48. Meyers, M., O. Vöhringer and V. Lubarda, "The Onset of Twinning in Metals: A Constitutive Description", *Acta Materialia*, Vol. 49, No. 19, pp. 4025–4039, 2001.